

POLITECNICO DI MILANO

Scuola di Ingegneria Industriale e dell'Informazione
Corso di Laurea Magistrale in Ingegneria Biomedica



**Transmission Electron Microscopy (TEM) Analysis for the
Investigation of
Phototropic Changes of Photoreceptor Outer Segments**

Supervisor: Prof. Riccardo BARBIERI
Co-Supervisor: Prof. Enrico Gianluca CAIANI
UIC advisor: Prof. Xincheng YAO

Author:

Jacopo BENEDETTI Matr. n. 849808

Anno Accademico 2016-2017

I want to thank my parents, my brother and my sister who allowed me to follow my dreams and always push me through the unknown and undiscovered. To Angela who has always been by my side, also when there was an ocean between us. I need to thank all my friends, with whom I enjoyed this beautiful adventure. To Cecilia, who always drives me crazy but she's the one that will always remember me this splendid University period we shared together. To Rap, Feib and Phase, I couldn't have asked for better mates. To my roommates, especially Gira, who taught me a lot about the statistical analysis. A final special thanks to Rap, he simplified everything. To my grandmothers and my friends, thanks for all the support you gave me.

ACKNOWLEDGEMENTS

I want to thank Professor Yao who allowed me to follow my interests and gave me the possibility to carry out a fascinating research on what I care most: our eyes. I must thank all my lab mates, especially Yiming, that always helped me out and became more friends than colleagues. To Figen Sailer without who all this study wouldn't have been feasible, and to all the patience she had with us. To Shen who helped me with cryosection.

I want also to thank Professor Barbieri and Professor Caiani for the help they gave me conducting this research, their experience and know-how was essential for the realization of this project.

JB

TABLE OF CONTENTS

<u>CHAPTER</u>		<u>PAGE</u>
1	INTRODUCTION	1
1.1	The Eyeball	2
1.1.1	The Retina	4
1.2	Eye Physiology	10
1.2.1	Phototransduction cascade	10
1.2.2	From Photoreceptors to Ganglion Neurons	14
1.2.3	From Ganglion Neurons to the Occipital Cortex	17
2	STATE OF THE ART AND AIMS OF THE THESIS	18
2.1	Previous research on Transient Retinal Phototropism	18
2.2	Aims of the Thesis	22
3	MATERIAL, METHODS AND EXPERIMENTAL SET-UP	24
3.1	MATLAB® algorithm implementation	39
4	RESULTS	45
4.1	Statistical Analysis – <i>Interdiscs</i> distances	47
4.2	Statistical Analysis – <i>Intradisc</i> distances	51
4.3	Comparison between manually and automatically obtained results	57
5	DISCUSSION AND CONCLUSION	63
6	APPENDICES	72
7	CITED LITERATURE	93

LIST OF TABLES

<u>TABLE</u>		<u>PAGE</u>
I	RODS AND CONES SYSTEM CHARACTERISTICS: DIFFERENCES AND SIMILARITIES.....	9
II	INTERDISCS DISTANCES PER CATEGORY AND <i>t</i> -TESTS RESULTS.....	48
III	INTERDISCS MEAN VALUES MANUALLY OBTAINED.....	56
IV	INTRADISCS MEAN VALUES MANUALLY OBTAINED.....	57
V	INTERDISCS AND INTRADISCS DISTANCES, MANUAL AND AUTOMATIC RESULTS	57
VI	BLAND-ALTMAN STATISTICAL APPROACH, BIASES AND LIMITS OF AGREEMENTS DISPLAYED.....	58
VII	MEAN OUTER INTERDISCS DISTANCES OBTAINED WITH THE TWO METHODS.....	60

LIST OF FIGURES

<u>FIGURE</u>		<u>PAGE</u>
1	The Eyeball.....	2
2	Retina Layers. Reprinted with permission.....	4
3	(A) Cones and rods photoreceptors anatomy. (B) Details of the photoreceptors OS: the system of stacked discs	6
4	Dark Adaptation Psychophysical curve	7
5	Cones wavelengths sensitivity	8
6	Phototransduction cascade scheme.	10
7	stimulus, Current and Membrane potential diagrams.....	12
8	Representation of molecular steps in photoactivation (modified from Leskov et al. [20]). .	13
9	(A) A perpendicular section of the human retina seen through the light microscope.	15
10	The Visual Pathway block diagram	17
11	(a) Schematic diagram of retinal photoreceptors of the leopard frog (<i>Rana pipiens</i>). (b) Histological images of dark-adapted and (c) light-adapted frog eyes. The red arrows indicate cone photoreceptors and the green arrows indicate rod photoreceptors. INL: inner nuclear layer; OPL: outer plexiform layer; ONL: outer nuclear layer; IS: inner segment; OS: outer segment; RPE: retina pigment epithelium; BrM: Bruch’s membrane; ChC: choriocapillaris. [45].....	18
12	(A) Confocal (left) and OCT (right) observation of transient phototropic changes evoked by a 20° oblique light stimulation. (B) Confocal(left) and OCT (right) observation of transient phototropic changes evoked by a - 20° oblique light stimulation.....	20
13	On the left the enucleated frog’s eye. On the right the same eye in a Petri dish containing Ringer’s solution and the two tools (tweezers and scissors) used for the hemisection procedure.....	24

14	Hemisected frog's eye inside a glass vial containing the fixative solution	25
15	Dim red light environment to process DA eyes.....	25
16	Box with black taped glass vials filled with fixative solution containing hemisected DA eyes	26
17	Model of hemisected eyeball.	27
18	Schematic Outline TEM.	29
19	Original (left) and modified (right) DA image obtained from the Central OS of the second DA eye.	31
20	On the left the original histogram, while on the right the histogram of the modified image.....	31
21	TEM image, 2500 X magnification	32
22	TEM image, 80 kX magnification	33
23	TEM image, 100 kX magnification	33
24	TEM image, 150 kX magnification	34
25	TEM image, 200 kX magnification	34
27	TEM image, 250 kX magnification	35
27	(A) detail of one randomly selected rectangle (133.6 x 180.4 pixels). (B) Rectangle magnification (115%). (C) Interdiscs distance manual calculation, the two final spots of the ruler touch with their extreme part the very first black border of the membrane. (D) Intradisc distance manual calculation, the two final spots of the ruler touch with their internal edge the two external black borders of the disc membrane.	37
28	Photoreceptor segments, from left to right: Synaptic Body, Inner Segment (nucleus, cytosol and organelles) and Outer Segment (OS) divided into: Inner OS, Central OS, Outer OS. ..	38
29	A) Representative image with salt and pepper noise, before filtering. B) Same image after filtering.....	39
30	A) Kirsch compass mask edge detection. B) Gradient in x edge detection.....	40

31	A) Original filtrated image. B) Original filtrated image with gradients superimposed. Red arrows characterize ROIs with low values while green arrows represent ROIs with higher values.	41
32	On the left, original gray scale cropped image. In the middle, cropped binarized image obtained with Otsu’s method. On the right, cropped binarized image obtained with <i>kmeans</i> function with k=4.	42
33	A) Example of a rotated rectangle, the angle of rotation is given by the gradient vector. B) Binarized image of the rectangle shown in A). C) Result of the algorithm for distance calculation. The green line represents the averaged distance from the borders, while the red and blue line represent respectively the signal (peaks/valleys according to white and black regions) unfiltered and filtered (moving mean 1D)	43
34	Fourier Transform magnitude	43
35	Fourier transform magnitude details. On the left a magnified image where it is possible to visualize the peaks. On the right a further magnification to better pinpoint the first peak location.....	44
36	TEM images with mean values related to the first and second LA eye.....	45
37	TEM images with mean values related to the first and second DA eye	46
38	Bar plot of the DA vs. LA interdiscs mean distances. Error bars showing standard deviations are superimposed to the histograms.....	48
39	Interdiscs bar plots of different categories showing differences between the two groups, DA and LA. Asterisks highlight the statistical significance.....	49
40	Interdiscs bar plots of the two experiments between the two groups, DA and LA. Asterisks highlight the statistical significance.....	50
41	Mean intradisc distance bar plot, similarities between DA and LA	51
42	Barplots of different tests with superimposed s.d. Asterisks highlighted statistical significance	53

43	Intradisc bar plots of different categories. Asterisks highlight the statistical significance...	54
44	Bar plot of the DA vs. LA interdiscs mean distances obtained using MATLAB®. Error bars showing standard deviations are superimposed to the histograms.	59
45	Bar plot of the DA vs. LA interdiscs mean distances obtained using ImageJ®. Error bars showing standard deviations are superimposed to the histograms.	59
46	Bar plot with superimposed s.d. of DA Outer OS and LA Outer OS interdiscs distances obtained using MATLAB®	61
47	Bar plots with superimposed s.d. of DA and LA intradisc distances obtained using MATLAB®. Two different thresholding methods were used: Otsu's and the <i>kmeans</i> clustering. Both tests are not significant	62
48	Rods Outer Segment shrinkage and bending when stimulated by light	63
49	Discs misalignment, hypothesized behavior to explain rod OS bending towards the direction of light.....	64

SUMMARY

Background and purpose. The Stiles-Crawford effect (SCE) refers to the directional sensitivity of the retina which means that light rays impinging at the center of the eye evoke a greater response of the neural cells composing the retina in respect to rays that enter the pupil more peripherally [1]. The lack of this effect in rods photoreceptors can be compensated by the presence of transient retinal phototropism (TRP), which instead it is been proved to be dominant in rods. TRP occurs mainly in the photoreceptors outer segment (OS) and it is correlated with the oblique light stimulation. Receptors, when stimulated, move towards the direction of the oblique light, and this phenomenon possibly compensates for some light efficiency loss caused by oblique light stimulation. Although the mechanism underlying this behaviour is not totally understood, early studies have reported disc-shape change of rod photoreceptor, but there is no direct evidence regarding the mechanism of discs' arrangement. This is the reason why this project is focused on the observation of these structures using a Transmission Electron Microscopy (TEM). To discover more about rod outer segment (ROS) changes, electroretinogram (ERG) studies have been pursued to compare ROS movement with the hyperpolarization of retinal photoreceptors (reflected by the onset of the ERG a-wave). It has been found that ROS shrinkage happens before the onset of a-wave (and before the hyperpolarization [3]), possibly indicating that disc-based stages of photo-transduction cascade contribute to the TRP phenomenon. This behavior can also explain the lack of TRP in cones as in these cells discs are linked with the membrane of the OS, while in rods discs are stacked one over the other without any linkage with the OS membrane. Therefore, because rod's discs are relatively free to float inside the OS, a light stimulation may entail and provoke a modification of these structures. Perhaps, shifting of the rods towards the central region can be due to the partial stimulation of discs that can have only one side of the pigment molecules bleached, while the unstimulated area will not undergo modification in its structure, causing a misalignment between them that may result in the ROS bending [45]. The aim of this study is the investigation of the rod's membranous disc utilizing TEM to find a quantitative explanation of this process and to discover the biophysical mechanism of rod OS dynamics. Besides

reflecting clear physiological mechanisms related to the functional response of the retina to a light stimulus, these dynamics could also provide a valuable tool for advanced diagnosis of retinal diseases.

Materials and methods. Leopard frogs' (*rana pipiens*) retinal samples were used for the experiment. Samples were collected from four eyes, two from Light Adapted frogs (LA), and two from Dark Adapted ones (DA). LA and DA frogs were euthanized and enucleated of both eyes, after at least 24 hours of light adaptation or dark adaptation respectively. The globe was hemisected along the equator with fine scissors and the lens and anterior structures were removed from the retina. The hemisected eyeball then was inserted in a glass vial containing the fixative solution.

After fixation, the samples were cryosectioned. Each hemisected eye has been transferred from fixative to 300 μ l 2.3 M sucrose (Sucrose 99%, @SIGMA life science) in 0.1 M sodium phosphate buffer pH 7.3 at 4°C for 1 hour, then embedded and quick frozen in an OCT compound (@Tissue-Tek) that facilitates the cutting procedure. To study photoreceptors' behaviour at the subcellular level and clearly pinpoint the differences and similarities in discs' distances between the two groups of samples, images from the Transmission Electron Microscopy (TEM) were analyzed. After having obtained the TEM images, two methods were applied for their analysis: 1) a manual method which exploited the properties of @ImageJ to measure *intradisc* and *interdiscs* distance; 2) an automatic method based on a @MATLAB algorithm to conduct the same analysis in an automatic way.

Results. Averaged LA *interdiscs* distances gave a mean \pm std of 5.803 ± 1.88 nm, whereas the corresponding DA averages gave 7.750 ± 1.79 nm. Mean *intradisc* (discs' transversal thickness) values were 13.668 ± 1.84 nm and 13.362 ± 1.52 nm for LA and DA respectively. Multiple *t*-tests were performed to assess the statistical significance of the difference between the two groups, samples and categories. Automatic and manual results were then compared to further validate our results. Both methods led to the same conclusion: LA frogs showed a significant shrinkage in the OS with respect to DA samples caused by light stimulus. The disparity in measurements between LA and DA samples

was found to be close to 2 nm in the *interdiscs* distances. Furthermore, this reduction has mainly occurred at the top of photoreceptors OS, as reflected in the *interdiscs* distances (the space between two adjacent discs), whereas the *intradisc* measurements difference between the two groups was not significant.

Conclusions. The innovative effort of this project focused on the comparative analysis of dark-adapted and light-adapted frog's retinas utilizing an electron microscope to focus at the nano-level, thus permitted to achieve a deeper understanding of the phenomena underlying the retinal phototropism effect. This study discovered new features of this biophysical event, not only assessing in a precise way the different morphology of photoreceptors OS caused by light but also discovering specifically where these modifications took place and which structures were affected. Although these findings are and will be very useful they are just a step of a longer pathway that we hope will permit to simplify the detection of certain pathologies and it will allow the patient to receive proper treatment on time, protecting as much as possible the incredible mechanism that is our vision. The main innovation stands in the collection of analytical data related on disc-shape modification that permitted to carry out statistical analysis on the different level and locations of shrinkage among the two groups. The identification and quantification of the differences and similarities between those groups not only brought to a deeper understanding on where and when the TRP phenomenon takes place, but also added a small brick on a wall of discoveries that is hoped will permit to conduct an early diagnosis of retinal pathologies such as AMD or diabetic retinopathy.

SOMMARIO

Introduzione. L'effetto Stiles-Crawford (SCE) si riferisce alla sensibilità direzionale della retina, ovvero i raggi di luce diretti nel centro dell'occhio evocano una maggiore risposta delle cellule neurali che compongono la retina rispetto ai raggi che entrano più perifericamente nella pupilla. La mancanza di questo effetto nei bastoncelli può essere compensata dalla presenza del fototropismo retinico transiente (TRP), che appunto è stato dimostrato dominante in questi cellule piuttosto che nei cono. Il TRP si verifica principalmente nel segmento esterno del fotorecettore (OS) ed è correlato con la stimolazione luminosa obliqua. I recettori, quando stimolati, si muovono verso la direzione della luce e questo fenomeno forse può compensare anche la perdita di efficienza luminosa causata proprio da questa stimolazione luminosa obliqua. Anche se tutt'ora non comprendiamo completamente il meccanismo sottostante a questo fenomeno, precedenti studi hanno sottolineato un cambiamento di forma dei dischi all'interno dei fotorecettori, ma non si hanno ancora prove dirette riguardo al meccanismo della disposizione dei dischi e per questo il progetto è incentrato sull'osservazione di queste strutture grazie all'utilizzo del *Transmission Electron Microscope* (TEM). Per avere più informazioni sui segmenti esterni dei bastoncelli (ROS), sono stati effettuati studi elettroretinografici (ERG) per confrontare il movimento dei ROS con l'iperpolarizzazione dei fotorecettori retinici (indicato dell'onda a-ERG). È stato scoperto che la riduzione in lunghezza dei ROS accade prima della nascita dell'onda a e quindi prima della iperpolarizzazione [3]. Ciò può indicare che le fasi della fototrasduzione che avvengono a livello dei dischi contribuiscono al fenomeno del TRP. Questo comportamento può anche spiegare la mancanza di TRP nei cono per il semplice fatto che in queste cellule i dischi sono collegati con la membrana del OS, mentre nei bastoncelli, i dischi sono impilati uno sopra l'altro senza alcun legame con la membrana OS. Quindi, poiché i dischi dei bastoncelli sono relativamente liberi di galleggiare all'interno del OS, una stimolazione luminosa potrebbe provocare una modifica di queste strutture. Lo spostamento dei bastoncelli verso la regione centrale può essere dovuto alla stimolazione parziale dei dischi, che possono avere solo un lato dei dischi

soggetto a stimolazione, mentre l'altro non stimolato non subirà modifiche nella sua struttura, causando un disallineamento e quindi una flessione dei ROS [45]. Lo scopo di questo studio è l'indagine dei dischi dei fotorecettori utilizzando il TEM per trovare una spiegazione quantitativa a questo processo e per scoprire la dinamica di questo meccanismo biofisico. Questa scoperta non solo avrebbe un'importanza fisiologica, dal momento che riflette un funzionamento funzionale della risposta retinica ad uno stimolo luminoso, ma potrebbe anche fornire uno strumento prezioso per la diagnosi avanzata delle malattie retiniche.

Materiali e metodi. Per l'esperimento sono stati utilizzati campioni retinici di rane di leopardo (*rana pipiens*). Sono stati considerati due gruppi di campioni, rane adattate alla luce (LA) e quelle al buio (DA). Gli animali LA dopo almeno 24 ore di adattamento della luce sono stati decapitati ed enucleati di entrambi gli occhi. Il globo è stato emisezionato lungo l'equatore con forbici di precisione e successivamente il cristallino e le strutture anteriori dell'occhio sono state rimosse dalla retina. Il bulbo oculare emisezionato è stato quindi trasferito in una fiala di vetro contenente la soluzione fissativa. Dopo la fissazione, i campioni sono stati crio-sezionati. Ogni campione è stato trasferito dalla soluzione fissante a 300 μ l di saccarosio 2,3 M (saccarosio 99%, $\text{\textcircled{R}}$ SIGMA life science) in 0,1 M sodio fosfato a pH 7,3 a 4 ° C per 1 ora, quindi incorporato e congelato velocemente in un composto OCT ($\text{\textcircled{R}}$ Tissue-Tek) che ne facilita la procedura di taglio. Al fine di studiare il comportamento dei fotorecettori a livello subcellulare ed individuare chiaramente le differenze e le somiglianze nelle distanze tra i due gruppi di campioni analizzati è stato utilizzato un microscopio a trasmissione (TEM). Dopo aver ottenuto le immagini TEM, sono state adottati due metodi per la loro analisi: 1) un metodo manuale che sfrutta le proprietà di $\text{\textcircled{R}}$ ImageJ per eseguire le misurazioni di distanze inter-dischi ed intra-dischi; 2) un metodo automatico che invece utilizza un algoritmo $\text{\textcircled{R}}$ MATLAB per condurre la stessa analisi ma in modo automatico.

Risultati. La distanza inter-dischi media dei campioni LA è risultata uguale a 5.803 ± 1.88 nm mentre quella dei campioni DA 7.750 ± 1.79 nm. Le distanze intra-disco (spessore trasversale del disco)

ottenute misurano 13.668 ± 1.84 nm e 13.362 ± 1.52 nm rispettivamente per campioni LA e DA. Per avere risultati utilizzabili in studi futuri, è stato necessario effettuare analisi statistiche per valutarne la loro veridicità. Infatti, anche se il valore medio calcolato su un grande quantitativo di campioni era certamente un punto di partenza, non era sufficiente a dimostrare oltre ogni ragionevole dubbio che i due gruppi considerati erano diversi o meno. Detto ciò, sono stati eseguiti più *t*-test per valutare la significatività statistica del valore medio considerando diversi gruppi, campioni e categorie. Successivamente sono stati confrontati risultati automatici e manuali per ottenere conclusioni più precise e significative. Entrambi i metodi utilizzati portano alla stessa conclusione: le rane LA hanno mostrato una riduzione in lunghezza nel OS rispetto ai campioni DA causata dallo stimolo luminoso. Inoltre, questa riduzione è stata principalmente presente nella parte terminale del OS, concentrata nelle distanze inter-dischi, ovvero nello spazio tra due dischi adiacenti, mentre le misurazioni di intra-disco non hanno mostrato differenze statisticamente importanti. Queste differenze tra campioni LA e DA risultano intorno ai 2 nm nelle distanze inter-dischi.

Conclusioni. L'innovazione di questo progetto comprende l'analisi comparativa di retine di rane adattate al buio e alla luce utilizzando un microscopio elettronico per focalizzarsi nella scala nanometrica, al fine di ottenere informazioni in più riguardanti il TRP. Questo studio ha permesso di scoprire nuove caratteristiche di questo evento biofisico, non solo valutando in modo preciso le differenze morfologiche che avvengono nel segmento esterno dei fotorecettori causate dalla luce ma scoprendo anche dove queste modificazioni avvengono e precisamente quali strutture sono coinvolte. Per quanto queste scoperte sono e saranno utili, questo studio è solo l'inizio di una ricerca che speriamo possa permettere di semplificare l'individuazione di alcune patologie in modo che i pazienti possano ricevere cure in tempo, proteggendo il più possibile l'incredibile meccanismo che è la nostra vista. L'innovazione principale sta nella raccolta di dati analitici relativi alla modifica di forma dei dischi che ha consentito di eseguire analisi statistiche tra i due gruppi. L'identificazione e la quantificazione delle differenze e delle somiglianze tra i campioni non solo ha portato ad una

comprensione più profonda su dove e quando il fenomeno TRP si svolge, ma ha anche aggiunto un piccolo mattone ad un muro di scoperte che speriamo possa permettere di condurre una diagnosi precoce di patologie retiniche quali l'AMD o retinopatia diabetica

CHAPTER 1

INTRODUCTION

Our eyes are marvelous sensing organs. They help us to process the world, to appreciate all the beauty, to read and gain knowledge and to connect our feelings and emotions with others fellow humans, for example through the visual arts [1].

The Visual system captures the light stimulus through the eye. The system is composed by a refractory mechanism with its lenses interacting with light beams, focusing and bending them, thus allowing a perfect localization on the retina surface and consequent transduction in electrical impulses by retinal cells, which permits vision. This incredible mechanism was born few hundred million years ago thanks to a microscopic copying error in the DNA of a bacterium who lived in the water. This random mutation gave that microbe a protein molecule that absorbed sunlight. Because of this mutation those bacteria could discern night and day cycles and fled from intense and harsh ultraviolet light which damaged DNA. Because of the utility of that protein, the mutation was inherited by the following generations and the molecule started to be concentrated in a pigment spot in the more advanced one celled organism. This represented an enormous advantage for those organisms that harvest sunlight to make food. With evolution, more and more complex systems were created. In thousands of generations natural selection was slowly sculpting the eye, creating at the end the complex and marvelous mechanism that is our vision.

To understand visual mechanisms, an introduction about eye anatomy and structures is presented.

1.1 The Eyeball

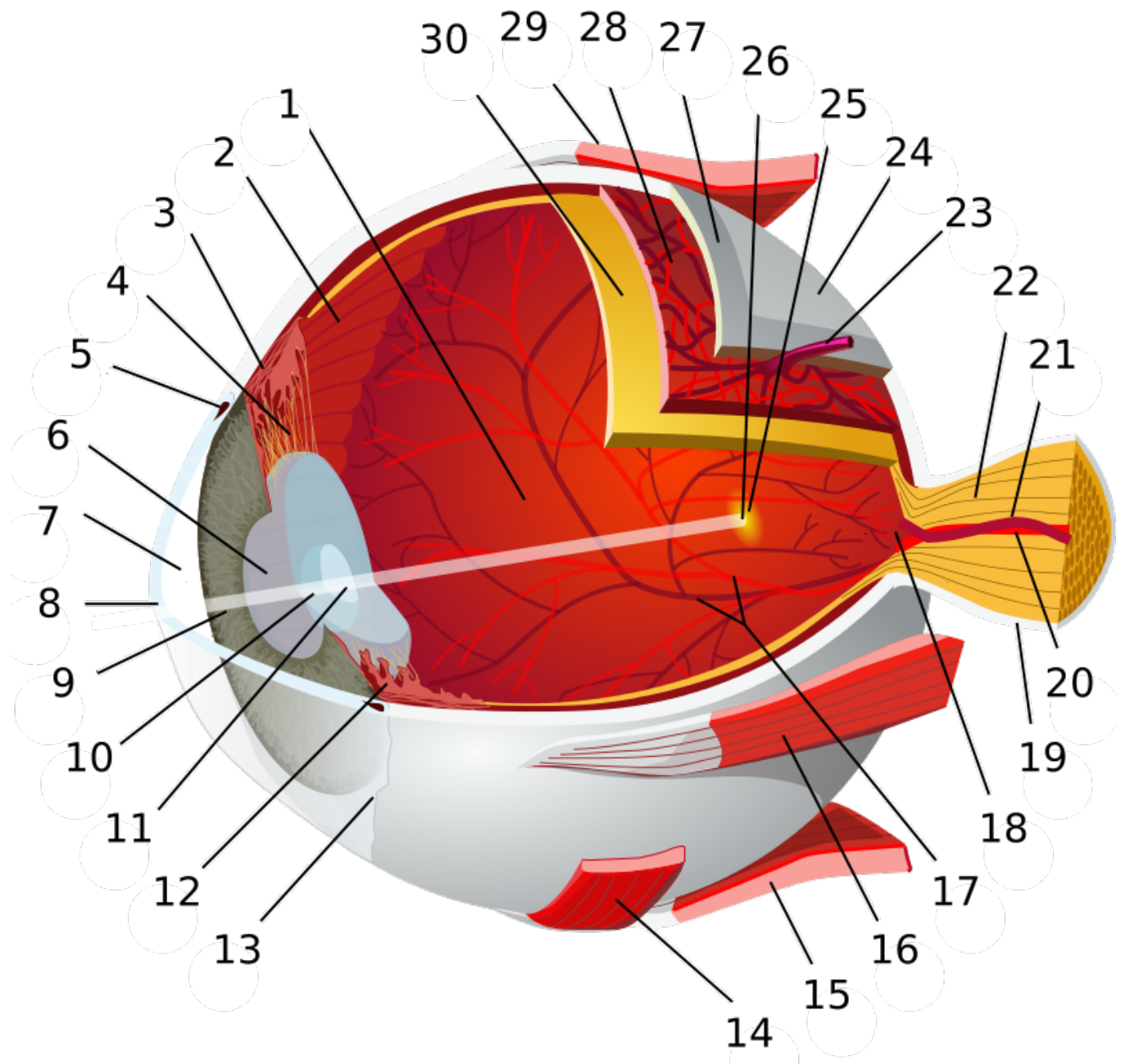


Figure 1 - The Eyeball.

Reprinted with permission. By Chabacano - References: 1. 2. 3. among others, CC BY-SA 3.0,

<https://commons.wikimedia.org/w/index.php?curid=1759001>

1. Posterior segment
2. Ora serrata
3. Ciliary muscle
4. Ciliary zonules
5. Schlemm's canal
6. Pupil
7. Anterior chamber
8. Cornea
9. Iris
10. Lens cortex
11. Lens nucleus
12. Ciliary process
13. Conjunctiva
14. Inferior oblique muscle
15. Inferior rectus muscle
16. Medial rectus muscle
17. Retinal arteries and veins
18. Optic disc
19. Dura mater
20. Central retinal artery
21. Central retinal vein
22. Optic nerve
23. Vorticose vein
24. Bulbar sheath
25. Macula
26. Fovea
27. Sclera
28. Choroid
29. Superior rectus muscle
30. Retina

The eye represents the interface between the stimulus and the nervous system. Iris, pupil and lens compose the optics element. The eye is anatomically divided in three concentric layers: **sclera**, **choroid** and **retina**. The **sclera** is the thickest of these layers and it is composed by fibrous connective tissue, which makes the white part of the eye white. The anterior part of the sclera is transparent (because in this area there aren't blood vessels) and it's called **cornea**; it provides two thirds of the total refraction in the eye, due to the interface between air (refraction coefficient $n \approx 1$) and a high-density tissue ($n = 1.38$). The **choroid** is a layer very rich of blood vessels and myelin, a pigment that captures light rays within the eyeball impeding reflection (like the interior black structures of a camera) [6]. Its anterior part it is composed by the **iris**, formed by colored muscular smooth fibers (the color is a genetic characteristic and it is due to a pigment similar to melanin) circular and radial to a hole called **pupil**. The dimension of the pupil, and so the conformation of the iris, determines the quantity of light that enters the eye. Contraction of the circular fibers constricts the pupil while contraction of radial muscles enlarges it, thus increasing the light that will enter in the eye. This mechanism is controlled by the Central Nervous System (CNS): specifically, the parasympathetic system response constricts the pupil, while the sympathetic stimulation rules its dilation. These two nervous systems are antagonist, if one is stimulated the other is inhibited and vice versa. The antero-medial region of the choroid is formed by the **ciliary body**, a circular smooth muscle that surrounds the edge of the lens. Attached to the ciliary body are suspensory ligaments called zonules. The **crystalline lens** is suspended inside the eye by the zonular fibers, and it is made of a transparent elastic protein. The lens, like the cornea, has no capillaries. The ciliary body is nourished by the same blood vessels that supply the iris. One of the main functions of the ciliary body is the production of aqueous humour, the clear fluid that fills the anterior and posterior chambers of the eye. It also regulates accommodation by modifying the shape of the crystalline lens, allowing the image to be focalized at short distance.

The crystalline lens is normally stretched by the ciliary body and ligaments, and contributes to the

total 59 diopter sphere (DS) by 20 DS, when looking at ∞ . Looking at a near object, the ciliary muscle contracts and the lens becomes rounder. In this way, it is able to accommodate and its dioptric power rises to 34 DS (+14 DS), thus the eye reaches $59 + 14 = 73$ DS.

1.1.1 The Retina

The **retina** constitutes the actual interface between the sensory part and the Central Nervous System, decoding the collected visual information into electrical impulses. It is a multi-layered sensory tissue lining the back of the eye with several neural cells interconnected by synapses. It contains approximately 120 million of **photoreceptors** [7] that capture light rays and convert them into electrical impulses. The human visual system, among all the biological ones, is the most complex and structured. In fact, as aforementioned, in the retina more than hundred million receptors are present, while in the auditory system the number of ciliated cells (the receptors that are divided into Outer Hair Cells and Inner Hair Cells) is approximately sixteen thousand [8]. There is a difference of almost four orders of magnitude between these two sensory systems; the sentence is self-explaining but can only give a glance of the total complexity of the visual system.

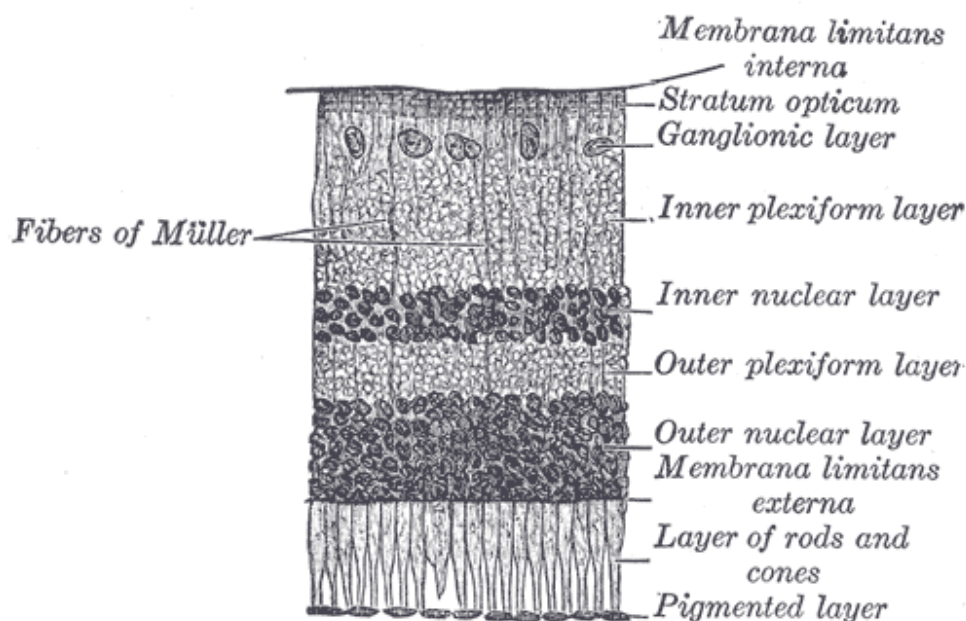


Figure 2 - Retina Layers. Reprinted with permission. Open Source:

<https://en.wikipedia.org/wiki/Retina#/media/File:Gray881.png>

This tissue is composed by both the sensorial cells that are light sensitive and the neural ganglions that perform the first stage of image processing.

The retina, which is a filmy piece of tissue barely half a millimeter thick (thinner in the peripheral areas and in the fovea) [10], is divided in different layers: a support layer, the retinal pigment epithelium (RPE), and seven functional layers: the photoreceptors layer (also divided into outer segments, inner segments, and a synaptic terminal), the outer nuclear layer, the outer plexiform layer, the inner nuclear layer, the inner plexiform layer, the ganglion cell layer and the nerve fiber layer, consisting in a bundle of neural connection headed towards the optic nerve. Externally to the RPE, the Bruch's membrane is found, a tiny basal membrane mainly made off collagen [9] and the Choriocapillaries, the capillary's lamina of the choroid.

The light, after having entered the pupil and travelled inside the eyeball, crosses all the layers and hits the photoreceptors, causing morphological and chemical changes that create a signal, then this information travels back to the ganglion cells layer which send the electrical impulses through the optic nerve. The sensory cells, the photoreceptors, unlike what one might expect, lie at the very back of the retina and not on its most internal side (the layer exposed to the liquid in the eyeball's vitreous chamber), so that light beams must cross the entire retina before meeting the photo-pigments molecules to excite them. Photoreceptors are arranged in this position because the membranes bearing the photopigments must be next to the Retinal Pigment Epithelium which provides a steady flow of Retinal (one of the forms of Vitamin A), which represent the “fuel” for these cells.

The Retinal Pigment Epithelium (RPE) is a thin layer rich in Melanin, which absorbs any light ray not captured by the retina.

The retinal pigment epithelium (RPE) performs five important tasks:

- Supplies blood for the outer two thirds of the retina.
- Resynthesizes photo-sensitive pigments.
- Phagocytes and recycles shed rod tips.

- Keeps the retina attached via a sucking force.
- Blocks light reflection thanks to melanin.

The photoreceptor layer is divided into the outer segment layer (outer photoreceptive segments), inner segment layer, and the synaptic terminal (Fig. 3A).

All vertebrate retinæ are composed at least by two types of photoreceptors: rods (square shape) and cones (pointy shape). Rods are usually employed for low-light (Scotopic vision) while cones are used in daylight (Photopic vision). Both rods and cones have three major functional regions: the

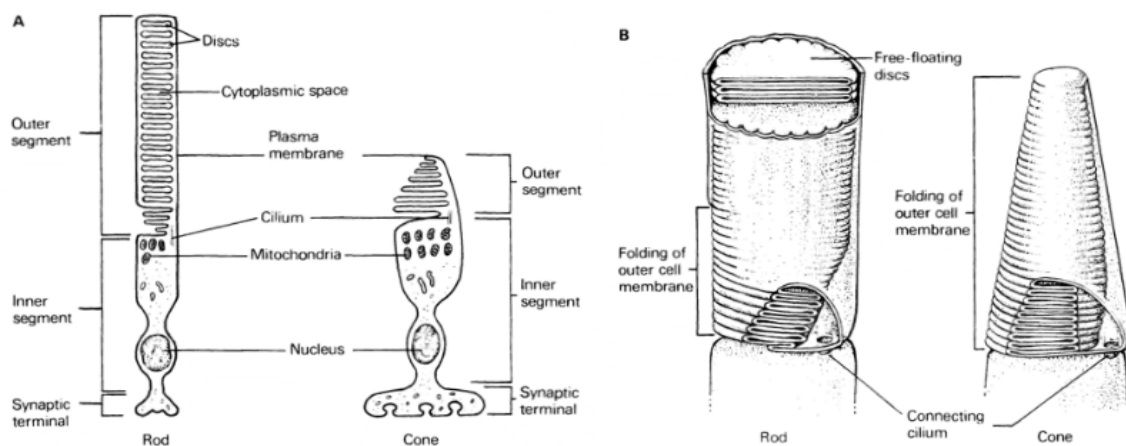


Figure 3 - (A) Cones and rods photoreceptors anatomy. (B) Details of the photoreceptors OS: the system of stacked discs.

Reprinted with permission. Open Source: <http://rspb.royalsocietypublishing.org/content/275/1653/2777>

outer segment (OS), specialized for photo-transduction, the inner segment, which contains the cell's nucleus and organelles, and a synaptic terminal, where the synaptic junction is located. The outer segments of both rods and cones are filled with an elaborate system of stacked membranous discs (Fig. 3B), which contain in their phospholipidic bilayer a spanning protein called Rhodopsin, comprising the light-absorbing molecules responsible for the initiation of phototransduction.

These discs are consumed by the light hitting them, but are continuously renewed and resynthesized by the RPE, with a rate of three discs per hour in humans [11]. The inner segment contains mitochondria, ribosomes and membranes, where pigment molecules are formed and transported to be included in the outer segment discs, and a cell body which contains the cell's nucleus. The latter part

of these cells is morphologically constructed to provide communication with the second order neurons. They form synaptic terminal where neurotransmission of information occurs.

The best way to underline differences between rods and cones is the dark adaptation psychophysical curve (Fig. 4). A subject exposed to intense daylight is put into complete darkness and his/her sensitivity threshold (vertical axis) is measured through a test light after an increasing adaptation time (horizontal axis). Obviously, threshold decreases with adaptation time. More interestingly, the curve is made by two exponentials (see Figure 4): the bigger black dots line represents cones rapidly adapting a high minimum threshold level, while the smaller dots line represents rods psychophysical curve, a slower adaptation but to a very low threshold (so a very high sensitivity).

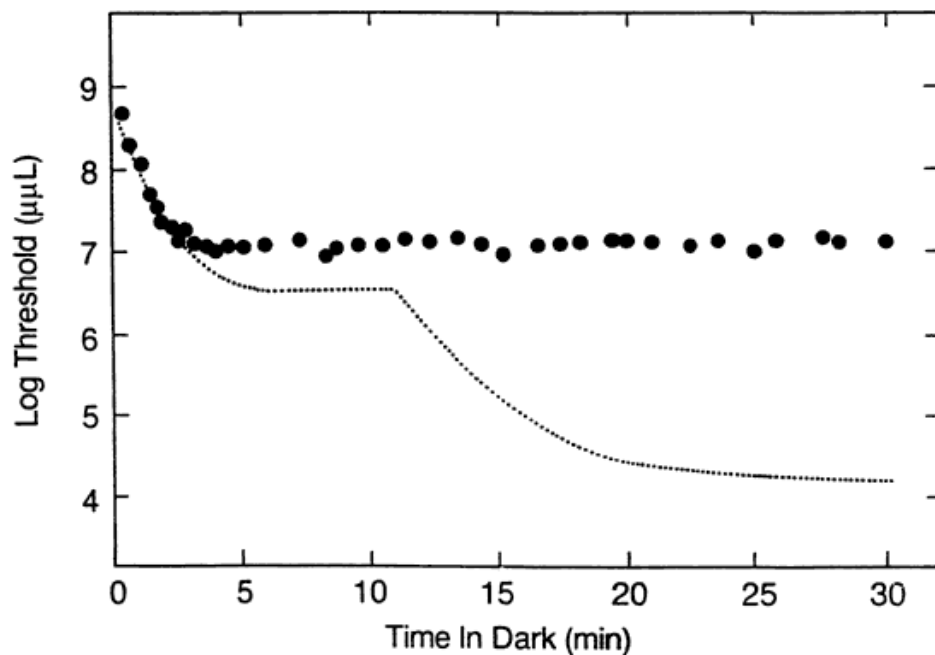


Figure 4 - Dark Adaptation Psychophysical curve. Reprinted with permission. Open Source:

<http://www.oculist.net/downaton502/prof/ebook/duanes/pages/v8/v8c016.html>

Therefore, at daylight rods are bleached (without photo-pigment); photopic vision is carried out by cones that adapt quite rapidly to illumination changes.

At night, cones do not work since illumination is below their minimum threshold; scotopic vision is carried out by rods, if adaptation permits to lower their threshold below illumination level.

The fovea, which is a depression in the central part of the *macula lutea*, which in turn is an oval

pigmented area close to the center of the retina, contains the clear majority of the cones, arranged together exploiting all the possible space, and permits a defined daylight vision. More peripheral parts of the retina are responsible for the detection of the feeblest light rays, thanks to rods.

Human eyes possess three slightly different types of cones: isomers, which differ in the morphological composition of the light-absorbing molecule, thus having different sensitivity according to the light wavelengths (Fig. 5): Blue cones, which are more sensitive to blue light ($\lambda=420$ nm); Red cones, which are more sensitive to red light ($\lambda=560$ nm) and green cones which are more sensitive to green light ($\lambda=530$ nm).

The exact and specific sensitivity of each of the three cone families is difficult to find, but can be

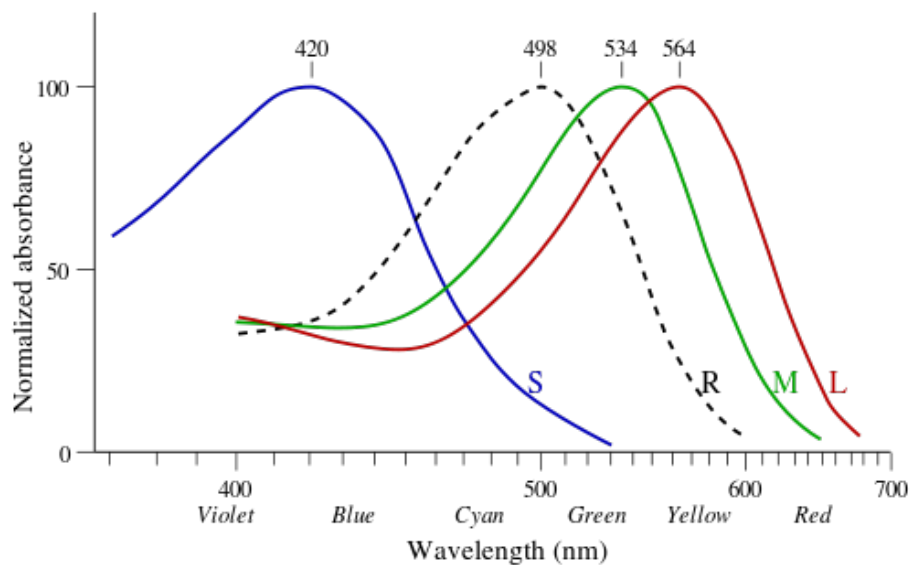


Figure 5 - Cones wavelengths sensitivity. Reprinted with permission. Open source:

<https://commons.wikimedia.org/wiki/File:Cone-response.svg>

derived from studies on colorblind subjects lacking one or two families. Besides, selective neurophysiology measure on cone cells and the biophysics of the specific absorbance of the three cones opsin-retinal complexes can be find [12].

Our color representation stresses Medium (M) and Long (L) wavelengths sum (yellow) and differences (red-green opposition) [13]. Blue is the color of dark, and green and red are the colors that allow us to define our images; there is an anatomical reason that explains that: in the *fovea*, which

is the maximum point of definition, the majority of cones are green and red.

In Table I the main differences and similarities of the two families of photoreceptors that populate the deeper layers of the retina are presented.

TABLE I: RODS AND CONES SYSTEM CHARACTERISTICS: DIFFERENCES AND SIMILARITIES

Rods and Rod System	Cones and Cone System
Cells which are more sensitive to light, nightlight vision	Cells which are less sensitive to light, daylight vision
Filled with more photo-pigment molecules	Filled with less photo-pigment molecules
Able to detect also a single photon	Not able to detect a single photon, low amplification
Have a slow response	Have a fast response
Mostly localized in peripheral area, not present in the fovea	Mostly present in the central part of the <i>macula lutea</i> (fovea)
Achromatic: only one type of photo-pigment	Trichromatic: three different cones with different light wavelengths sensitivity

When the light beam strikes the retina, rods and cones are able to generate an electrical impulse that propagates to other cells along different retina's layers (i.e. bipolar, horizontal and amacrine cells), thus reaching the ganglion neurons that bundle together at the level of the optic disc forming the optic nerve. Then, the information travels through the nerve, passing for the optic chiasm, the lateral geniculate nucleus up to the occipital striate cortex, where the brain starts the analysis of the electrical impulses ending with the perception of the world we are used to.

1.2 Eye Physiology

1.2.1 Phototransduction cascade

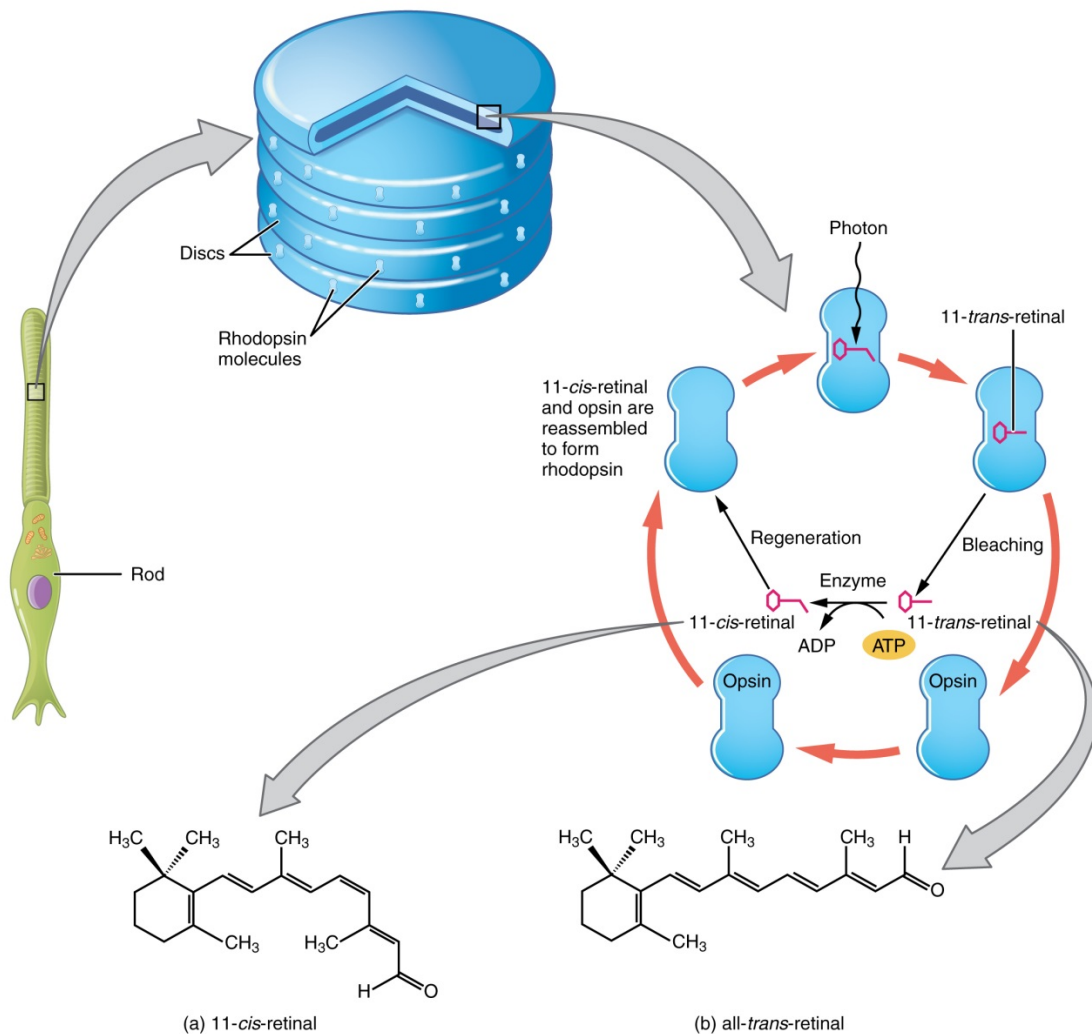


Figure 6 - Phototransduction cascade scheme.

Reprinted with permission. Open source: By Opens tax College - Anatomy & Physiology, Connexions Web site.

<http://cnx.org/content/col11496/1.6/>, Jun 19, 2013., CC BY 3.0, <https://commons.wikimedia.org/w/index.php?curid=30148001>

To understand the details of the experiment proposed in this thesis, it is necessary to include a section related to the phototransduction cascade (Fig. 6). How physiologically the eyes, specifically the

photosensitive area that lays on the very back of the eyeball, i.e. the retina, does process light, and how this light interaction entails physical changes.

For our purposes, it is critical to understand the underlying molecular mechanism responsible for the vision. The Rods Outer Segment (ROS), as well as the cones one, in the years have evolved as an elaborate system of staked membranous discs. These structures contain a large number of membrane spanning proteins (as many as 10^8 in each cell) [14] called Rhodopsin. Embedded in their cores retinal molecules are found, constituted by small light-absorbing particles responsible for the initiation of the phototransduction cascade. The outer segments are continuously renewed; in human rods, for example, three new discs per hour are created [15] while in frogs about 80 discs are generated every day [16]. These disc-shape structures are filled with thousands of rhodopsin complexes. Light exposure changes a linkage in the retinal molecule that twirls, modifying the shape of the protein from *retinal 11-cis* (attached to rhodopsin) to *retinal 11-trans* (detached to rhodopsin and starting the transduction). In rest conditions (dark), two ionic currents are dominant in a photoreceptor. An outward current of potassium ions (K^+) flows through non-gated potassium-selective ion channels located in the inner segment, while an inward current of sodium ions (Na^+) flows through cyclic guanosine 3'-5' monophosphate (cGMP) gated channels, which are mostly circumscribed in the photoreceptor's outer segment. While the outward current of potassium ions tends to hyperpolarize the cell's membrane to a potential equal to -70 mV, the inward sodium current tends to depolarize the photoreceptor's membrane. In darkness, the cytoplasmic concentration of cGMP is high enough to maintain open the cGMP-gated channels, thus allowing a steady current, called the dark current, to freely flow inside the photoreceptor. As a result, in the dark the photoreceptor's membrane potentials are set at an equilibrium voltage of -40 mV.

The absorption of light by retinal, the visual pigment comprised into the rhodopsin, initiates and triggers a cascade of events that leads to a change in ionic fluxes across the plasma membrane of these cells, which consequently cause a modification in the membrane potentials. This cascade can be summarized as follows [17]:

1. Light activation of a photo-pigment called Retinal. Two parts compose the pigment: the protein portion Opsin, which spanned the discs' membrane, and the light-absorbing portion Retinal, a derivate of vitamin A. In its non-activated form, Rhodopsin contains the *11-cis* isomer of retinal, which is fitted perfectly into the binding site in the Opsin molecule.

When the light absorption occurs, retinal *11-cis* changes to a *11-trans* (*all-trans*) conformation. The Opsin therefore evolves in a semistable conformation called Metarhodopsin II, which triggers the second step. This unstable form splits in few minutes, due indeed to its unstable conformation, forming Opsin and *all-trans* retinal. The *all-trans* retinal then is transported at the RPE level where it's firstly transformed in *all-trans* retinol (Vitamin A) and then in *11-cis retinal* again. Thanks to other actors involved in the process, this final molecule is transferred back again to photoreceptors.

2. The reduction of the cytoplasmic concentration of cGMP caused by Retinal activation. Rod phototransduction is typical example of heterotrimeric G-protein signal pathways (Fig. 10). The receptor represented by the rhodopsin has a G-protein, the transducin, attached, thus forming a modular system. The effector of the system is cGMP phosphodiesterase (PDE or PDE6) [18]. After photon absorption, the rhodopsin molecule becomes enzymatically active and catalyzes the activation of the G protein transducin. Transducin, in turn, activates the PDE6. The effector activation causes an hydrolization of the cyclic guanosine 3'-5' monophosphate (cGMP) which is profoundly broken down into 5' - GMP.

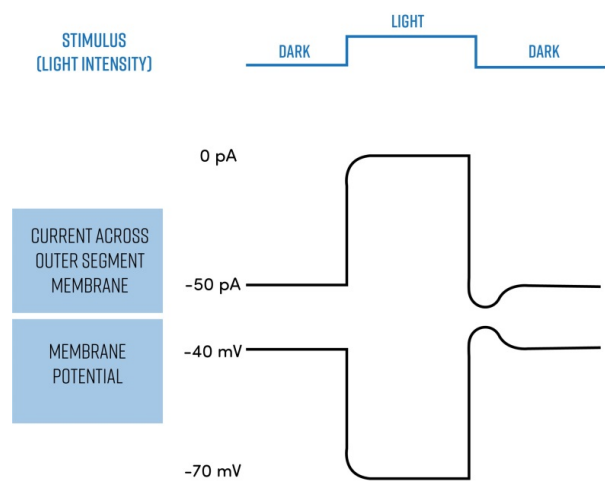


Figure 7 - Stimulus, Current and Membrane potential diagrams

The obtained decrease in concentration of cGMP entails and leads to a closure of the cGMP-gated channels, that stops the Na^+ outward current (Fig. 7).

This is a very high gain mechanism, as a single photon can activate this chain reaction, leading to the hydrolyzation of more than 10^5 molecules of cGMP per second [19]

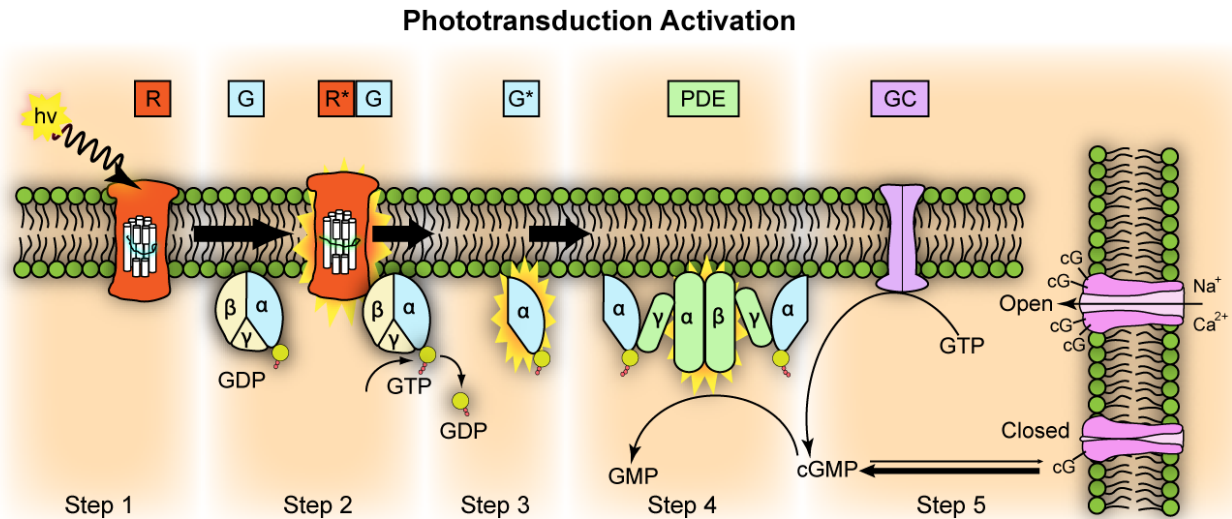


Figure 8 - Representation of molecular steps in photoactivation (modified from Leskov et al. [20]).

Depicted is an outer membrane disk in a rod. Step 1: Incident photon ($h\nu$) is absorbed and activates a rhodopsin by conformational change in the disk membrane to R^* . Step 2: Next, R^* makes repeated contacts with transducin molecules, catalyzing its activation to G^* by the release of bound GDP in exchange for cytoplasmic GTP, which expels its β and γ subunits. Step 3: G^* binds inhibitory γ subunits of the phosphodiesterase (PDE) activating its α and β subunits. Step 4:

Activated PDE hydrolyzes cGMP. Step 5: Guanylyl cyclase (GC) synthesizes cGMP, the second messenger in the phototransduction cascade. Reduced levels of cytosolic cGMP cause cyclic nucleotide gated channels to close preventing further influx of Na^+ and Ca^{2+} . Reprinted with permission. Open Source: By Jason J. Corneveaux, wiki user: Caddymob

(talk) - <http://en.wikipedia.org/wiki/File:Phototransduction.png>, CC BY 3.0,

<https://commons.wikimedia.org/w/index.php?curid=10051519>

3. The stop of Na^+ outward current causes a hyperpolarization of the photoreceptors membranes. The closure of the cGMP-gated inward channels interrupts the dark current and causes a slow hyperpolarization of the cell. It is important to note that, in contrast with most of other sensitive and non-sensitive neurons, the signal is represented by a hyperpolarization and not from a depolarization of the membrane. Consequently, no threshold is present. This reflects the weird

behavior of these cells (cones and rods) that release neurotransmitter (Glutamate) in the dark, when the membranes are depolarized, while they stop its delivery when the light hits them generating hyperpolarization of their membrane, that continues until the light shines on the photoreceptors.

1.2.2 [From Photoreceptors to Ganglion Neurons](#)

The other layers that compose the retina implement the first stages of visual processing. The inner nuclear layer and the ganglion cell layer are cellular layers; the outer and the inner plexiform, instead, are layers formed by axons and dendrites that link the different structures.

The photoreceptors are localized in the deepest layer, close to the pigment epithelium. The inner nuclear layer is composed by the nucleus of horizontal and bipolar cells while amacrine cells are situated in more inner layers, close to retina surface, where ganglion neurons are found. Axons and dendrites of these cells create neural connection between different cell bodies constituting the plexiform layers.

The first synaptic junction is made between photoreceptors and bipolar cells. The human retina presents two different bipolar cells that are characterized by different receptors for the neurotransmitter glutamate. This distinction allows having opposite responses according to which cells are excited. The OFF bipolar cells, active in dark condition and firing in response to glutamate, which is continuously released when light doesn't shine on photoreceptors, are able to detect dark images against a lighter background, and this behavior is known as the OFF pathway in the visual process.

Other bipolar cells have inhibitory glutamate receptors; in other words, a photoreceptor hyperpolarization stops the bipolar cell inhibition, which in turn permits to the connected neuron to fire. This constitutes the ON pathway in the visual process, and it is represented by the ability to detect light images on a darker background. Other cells, horizontal and amacrine cells, connecting several cells at different levels, are supposed to integrate information to obtain stronger and efficient transmission of the receptive fields.

But the retina wasn't simply created to transmit opposite-contrast images directly from the photoreceptors to the brain, because in that case the images created would have been blurred and poor in quality. At this level, instead, there is an incredible integration of information both in a vertical and in a transverse direction [21].

Different cones send information to the same horizontal cell at the first synaptic level in the retina, which in turn integrates the inputs enhancing the image quality at the very first step of the visual process. Each horizontal cell receives impulses from many cones, creating a very wide receptive field or collection area. This receptive field becomes even larger due to the ability of these cells to create gap junctions with the neighboring horizontal cells.

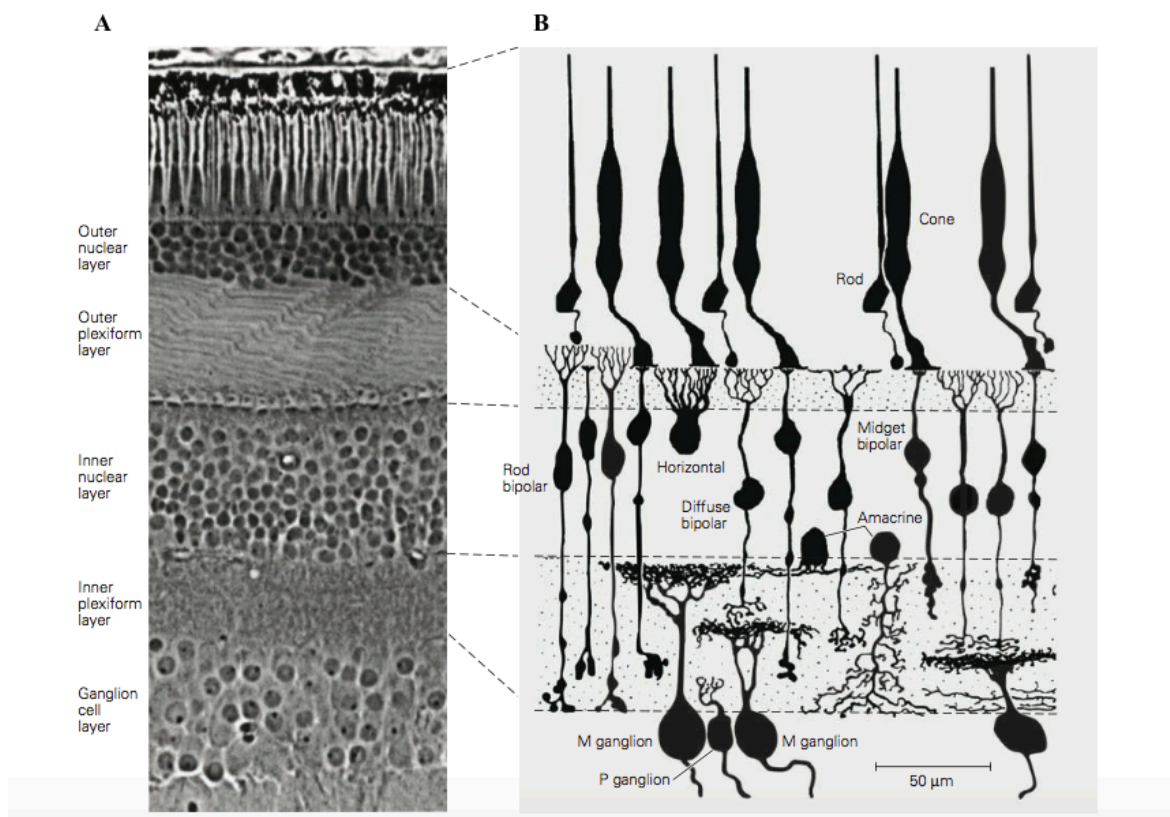


Figure 9 - (A) A perpendicular section of the human retina seen through the light microscope.

Three layers of cell bodies are evident. The outer nuclear layer contains cell bodies of photoreceptors; the inner nuclear layer includes horizontal, bipolar, and amacrine cells; and the ganglion cell layer contains ganglion cells and some displaced amacrine cells. Two layers of fibers and synapses separate these: the outer plexiform layer and the inner plexiform layer. (B) Neurons in the retina of the macaque monkey based on Golgi staining. The cellular and synaptic layers are aligned with the image in part A. Reprinted with Permission by Eric Kandel, Principles of Neural Science, 5th edition [Appendix A].

The horizontal cells receive inputs from the cones and transfer them to the bipolar cells that integrate the information of different cones, far away from each other. At a higher level, in the inner plexiform layer, more than 22 different types of amacrine cells are found [22], thus creating neural connections with about 20 different types of ganglion cells, while retinal synapses are mostly organized in an outer plexiform layer. In this layer, synaptic terminals of rods (called *spherules*) and cones (called *pedicles*) are presynaptic to bipolar and horizontal cells.

The rods and cones retinal pathways signals are relatively independent until they reach the ganglion cell layer, where both systems share the same output neurons and the information is integrated. However, these signals are not completely independent because electrical synapses occur between processes that extend from cone pedicles to rods. There is only one type of rod bipolar cell, but there are at least two different classes of cone bipolar cells [7]: invaginating and flat. The invaginating cone bipolar cells send their dendrites into invagination in the cone pedicle, where they form the central element of three processes in each invagination centered on a synaptic ribbon. The two lateral elements in this "triad" relationship are dendrites of horizontal cells. It is possible to discriminate between two types of amacrine cells, the ones that use glycine and those that use GABA (gamma-aminobutyric acid) as neurotransmitters.

The last retinal main components are the Muller cells. These cells are the principal glial cells of the retina [23]. They provide architectural support structures spanning radially the entire thickness of the retina, thus creating its limits both at the outer and at the inner membrane. They provide critical functions, such as supplying end-products of anaerobic metabolism, cleaning out products such as CO₂ and NH₃, controlling homeostasis (the fixity of *milieu interior*) and protecting neurons by maintaining fixed the concentration of ions such as K⁺ and Na⁺, synthesizing retinoic acid from retinol [24] and probably being involved in both phagocytosis of neural residues and releasing of substances such as GABA, taurine and dopamine [25].

1.2.3 From Ganglion Neurons to the Occipital Cortex

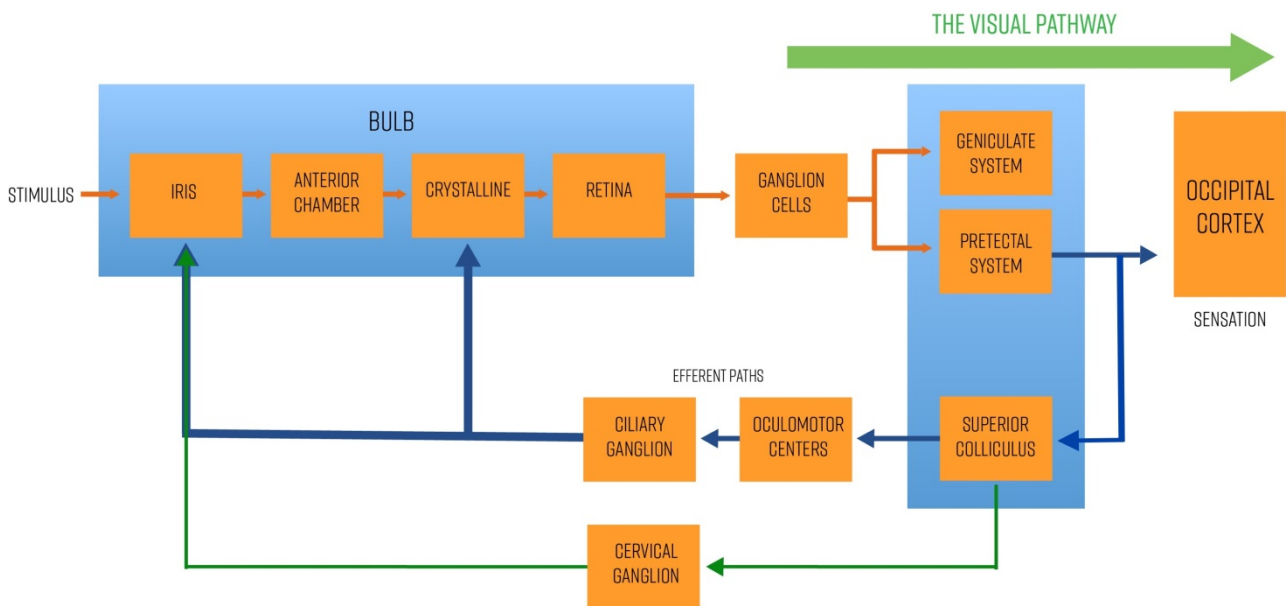


Figure 10 - The Visual Pathway block diagram

The path from the stimulus to the ganglion cells has been already discussed in previous sections. In this paragraph, for sake of completeness the path from ganglion cells to the occipital cortex, passing by different nuclei which perform several tasks, is showed. Higher order analysis is computed by different areas of the cortex, thus resulting in an image formation that is characterized by depth, colors and shapes. However, the knowledge about this higher order integration is partial, very complicated and out of scope in respect to the current thesis. The interested reader is invited to have a look at the Chapters 25, 27 and 28 of the "Principles of Neural Science" [26].

CHAPTER 2

STATE OF THE ART AND AIMS OF THE THESIS

2.1 Previous research on Transient Retinal Phototropism

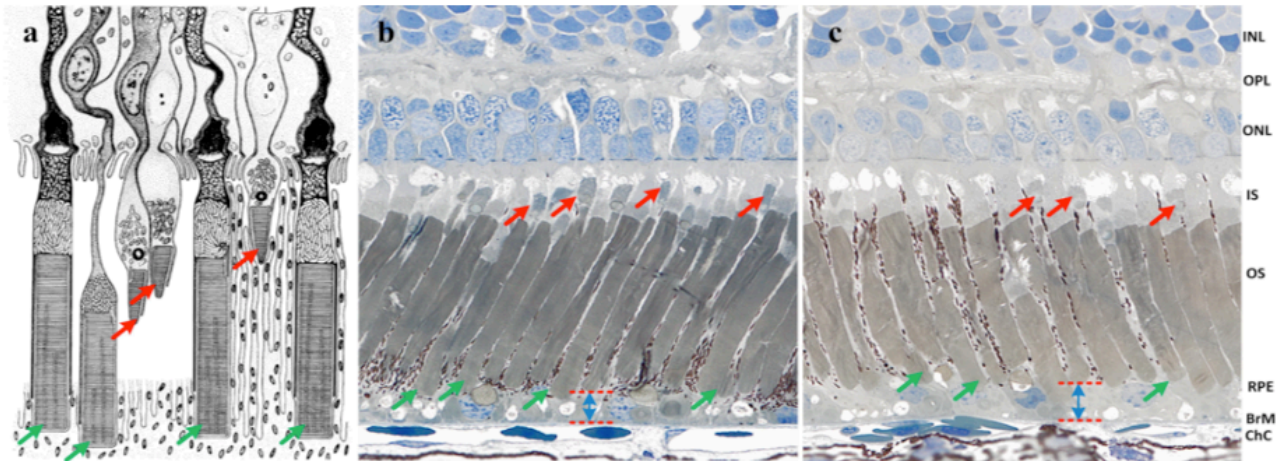


Figure 11 - (a) Schematic diagram of retinal photoreceptors of the leopard frog (*Rana pipiens*). (b) Histological images of dark-adapted and (c) light-adapted frog eyes. The red arrows indicate cone photoreceptors and the green arrows indicate rod photoreceptors. INL: inner nuclear layer; OPL: outer plexiform layer; ONL: outer nuclear layer; IS: inner segment; OS: outer segment; RPE: retina pigment epithelium; BrM: Bruch's membrane; ChC: choriocapillaris. [45]

Transient Retinal Phototropism (TRP) is a phenomenon that occurs mainly at the level of photoreceptors Outer Segment (OS). TRP describes the photoreceptor behavior when stimulated with light: OS subjected to light beam shrinks while photoreceptors located at the borders of the light stimulus bend towards the direction of radiation [30].

In the lower part of Fig. 11 (c) and (b) light-blue arrows identify the photoreceptors' shrinkage: the distance between the Bruch's membrane (BrM) and the tip of OS is clearly increased in light-adapted samples, which means that the outer segments have shrunk [30].

Opposite to the Stiles-Crawford effect (SCE) that is predominant in cones [31], high spatial and temporal resolution images demonstrate a higher presence of TPR in rods [32]. The SCE refers to the

directional sensitivity of the retina, which means that light rays impinging at the center of the eye evoke a greater response of these neural cells with respect to rays that enter the pupil more peripherally. TRP occurs mainly in the photoreceptors OS and it is correlated with the oblique light stimulation. Receptors move towards the direction of the oblique light and this phenomenon perhaps could compensate for some light efficiency loss caused by oblique light stimulation. This discovery was the starting point of all the previous research relevant to this topic. Carrying out different experiments, it has been proved by Zhao et al. [45] that this shrinkage and bending happened in the OS and that's why all the conducted tests focused the attention on these structures, both physically and chemically.

Traditionally, the hybrid confocal microscopy and the spectral-domain optical coherence tomography (SD-OCT) were used to study the sub-cellular source of this phenomenon [33]. In that study, the aim was to identify precisely the axial location (i.e. in which segment of the photoreceptor the effect was predominant) and to understand if it was possible to map the Phototropism through the reflected light imaging modality. The experiment consisted in an oblique light stimulation of $+20^\circ$ and -20° on a living frog retina contemporaneously with the recording of images with the two microscopes described above. Thanks to an optical flow algorithm [34] following motion of the different structures in sequential images, the researchers were able to calculate the micrometric displacement of photoreceptors. Interesting results were found: photoreceptors clearly move toward the direction of the incident oblique light stimulation, to the right for the $+20^\circ$ light stimulus and to the left for the -20° radiation flashes (Fig. 12). This behavior was previously observed in experiments carried out with a digital NIR microscope [35], and confirmed by such a study.

The additional information given by this last experiment is related to the intrinsic property of SD-OCT imaging, able to obtain depth resolved cross-sectional retinal images and thus accurately pinpoint where this photoreceptor movement was localized. This analysis revealed that TRP predominantly occurred in the ROSs.

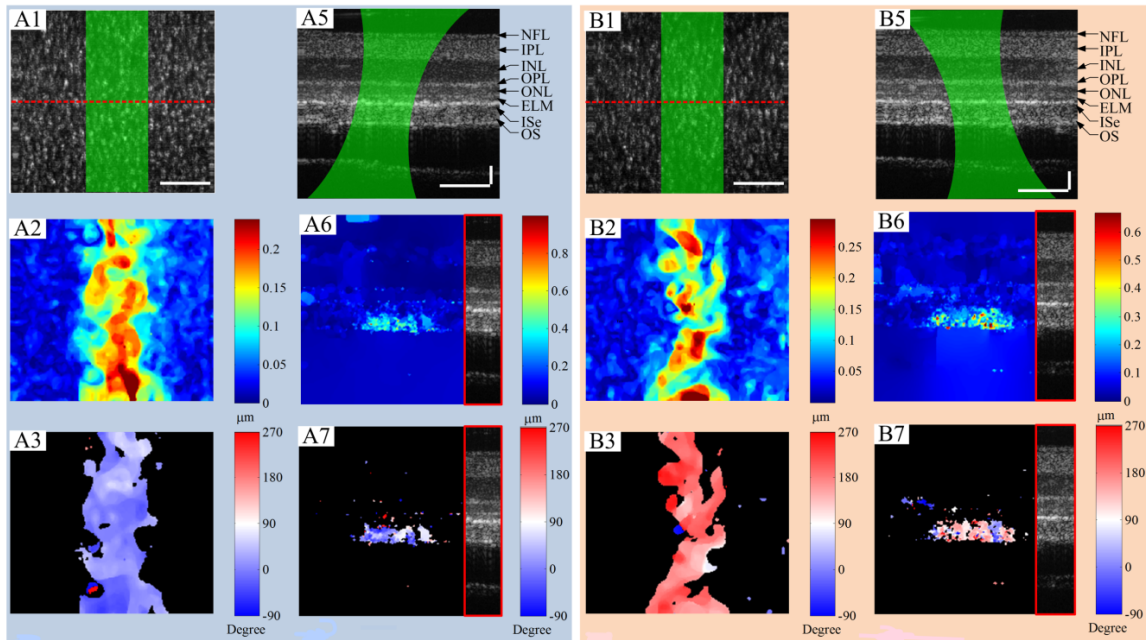


Figure 12 - (A) Confocal (left) and OCT (right) observation of transient phototropic changes evoked by a 20° oblique light stimulation. (B) Confocal(left) and OCT (right) observation of transient phototropic changes evoked by a - 20° oblique light stimulation.

(A2, A6) TRP magnitude map of Confocal and OCT respectively. (B2, B6) TRP magnitude map of Confocal and OCT respectively. (A3, A7) TRP direction map derived from confocal and OCT images respectively. (B3, B7) TRP direction map derived from confocal and OCT images respectively. We can clearly observe that as far as the 20° oblique light stimulation the color of the direction map is light blue, that means 0° of the unit circle, which in turn means right movement. The same is also true for the -20° oblique light stimulation, in this case the direction map color is light red, or 180°, which means left movement. Reprinted with permission by The Optical Society [Appendix B] - Wang, B., Zhang, Q., Lu, R., Zhi, Y., and Yao, X.: Functional optical coherence tomography reveals transient phototropic change of photoreceptor outer segments. *Optics letters*, 2004, pp. 6923 to 6926. [33].

After this discovery, researchers started to investigate the physiological mechanism lying behind this phenomenon. When exactly did this effect take place? At which level of the phototransduction chain of events was this phenomenon taking place? What were the conformational changes within ROS? To these open questions the scientific community is still trying to give an answer.

To discover more about these rod outer segment (ROS) changes, electroretinogram (ERG) studies have been done in order to compare ROS movement with the hyperpolarization of retinal photoreceptors, showing that ROS shrinkage happens before the onset of the a-wave, which is known

to reflect the membranous hyperpolarization of photoreceptors [36]. This event might indicate that the phototropic changes could be dependent on ROS discs' shape modification happening during the phototransduction cascade. This discovery was consistent with earlier studies in which ROS discs changes due to light interaction were reported [37].

Summarizing, ROS movements are driven by receptorial events that occur before the light dependent closure of cGMP-gated ion channels takes place. These signals build upon an upstream mechanism, on the stimulation of photo-pigment molecules (disc-based phototransduction cascade), and involve the activation of several effectors, such as rhodopsin, transducin and cGMP phosphodiesterase (PDE6). It has not yet been discovered at which level of this sequential activation of molecules the TRP takes place; possible replies include stimulus-evoked rhodopsin-, transducin- and PDE-dependent permeability changes [38], compression of disc membrane or discs interspace [39] and the distribution of phospholipids in the disc membrane [40].

The goal of Wang's project was the comparative analysis between phototropism, associated with the dynamical movement of ROS, and the electrophysiological behavior in frog's retina stimulated by oblique visible light. This ROS bending and shrinking was not clearly understood but perhaps the shifting of the rods towards the central region could be due to the partial stimulation of discs that could only have a part of the OS stimulated by light rays. This behavior may also explain the lack of TRP in cones for the simple fact that in these types of cells the discs are linked with the membrane of the OS, while in rods these discs are stacked one over the other and are not attached to the OS membrane. So, because rod's discs are relatively free to float inside the OS, a light stimulation may entail and provoke a modification of these structures, shrinking what can be called the *intradisc* length (the cross-sectional height of a disc) or the *interdiscs* length (distance between two adjacent discs), while in cones this behavior would be a lot more complicated due to the linkage of discs with the OS membrane. Furthermore, a partial stimulation of discs might cause a partial disc shape modification and shrinkage, while the unstimulated area won't undergo modification in its structure, resulting in a misalignment between them that may cause the bend of ROS [30].

2.2 Aims of the Thesis

The proposed project aimed to continue along the path already followed by previous experiments. The goal was to clarify the biophysical mechanism underlying rod OS dynamics, to investigate the conformational changes of the OS and to provide a quantitative explanation of this process.

Previous studies utilizing time-lapse microscopy revealed stimulus-evoked conformational changes of rods OSs, while dynamic confocal microscopy and optical coherence tomography (OCT) have revealed rod outer segment movement as the physical source of phototropism.

The objective of this project was the investigation and analysis of differences in the rod OS as estimated from two groups of samples: Light Adapted and Dark Adapted leopard frog's retinas using a high-resolution (0.2 nm [41]) Transmission Electron Microscopy (TEM) to allow an accurate observation of the rods OS discs to clearly identify where changes happen.

Aim 1: Distinction between Dark Adapted and Light Adapted frog's retinas.

Comparative histological images analysis obtained in previous studies have demonstrated that Light Adapted retinas showed increased distances between rod tips and Bruch's membrane (BrM) [30] in respect to the Dark Adapted ones. Utilizing a high-resolution microscope such as the TEM it was possible to conduct a better investigation of the differences in these two types of retinas, focusing the attention in the elements within the rod OS, the pile of stacked membranous discs.

Aim 2: Location of the shrinking.

Our second aim pertains to the identification of the location where the shape modification happens. Thanks to the massive resolution of the transmission electron microscopy it was possible to accurately pinpoint the rod OS. The further goal was to discover where the shrinkage happened, if it was due to a modification of the discs' membrane or otherwise if it was due to a reduced distance of the space between adjacent discs. Furthermore, of primary importance was not only the differentiation between *intradisc* and *interdiscs* modifications but also the detection of where precisely along the

photoreceptors OS these modifications were greatly remarked. For this reason, three different locations were considered.

The innovation of this project included the comparative analysis of Dark Adapted and Light Adapted frog's retinas utilizing TEM for a better understanding of the phenomena underlying the retinal phototropism effect focusing on the structures within the photoreceptors. It was an innovative research from the moment that nobody previously had done such a comparative study analyzing different groups' samples at the nano scale level and it could be useful and helpful for the discovery of new features that cause this biophysical event. Trying to identify and quantify the differences between these two categories can bring to a deeper understanding on where and when this phototropism effect takes place and how it affects the phototransduction cascade.

CHAPTER 3

MATERIAL, METHODS AND EXPERIMENTAL SET-UP

Retina Preparation

Leopard frogs (*rana pipiens*) retinal samples were used for the experiment. The utilized animal model was the frog because this animal' physiological visual characteristics are very similar to the human ones, mainly differing in the higher number of rods [44] and in the size of the neural cells [45].

Two groups of samples were considered, Light Adapted frogs (LA) and Dark Adapted ones (DA). For each group, two eyes were analyzed. LA animals were left in normal light condition before the euthanization and enucleation of both eyes. The globe was hemisected along the equator with fine scissors and the lens and anterior structures were removed from the retina. The hemisected eyeball then was inserted in a glass vial containing the fixative solution (see Figs. 13 and 14)

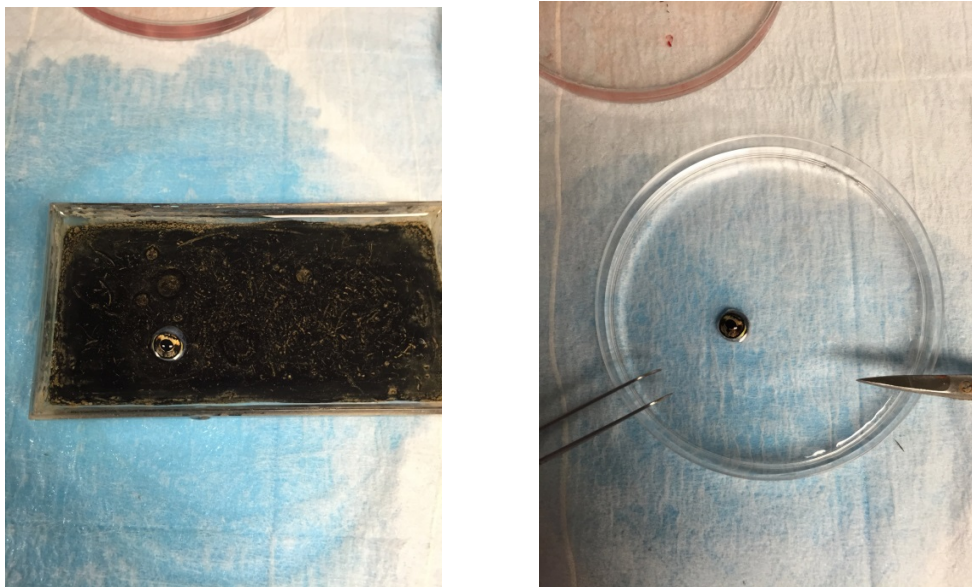


Figure 13 – On the left the enucleated frog's eye. On the right the same eye in a Petri dish containing Ringer's solution and the two tools (tweezers and scissors) used for the hemisection procedure



Figure 14 – Hemisected frog's eye inside a glass vial containing the fixative solution

For the DA group, after at least 24 h of dark adaptation, the procedure was performed in a dark room under dim red light in order not to contaminate with light the samples. The samples preparation was performed in Ringer's solution containing 110.0 mM NaCl, 2.5 mM KCl, 1.6 mM MgCl₂, 1.0 mM CaCl₂, 22.0 mM NaHCO₃, 10.0 mM D-glucose infused with O₂ for 5 minutes [46-48].



Figure 15 – Dim red light environment to process DA eyes

All experiments were performed following the protocols approved by the Animal Care Committee (ACC) at the University of Illinois at Chicago, as part of a research study under the supervision of Prof. Yao.

The hemisection was done as quickly as possible and the samples were exposed to air only for a few seconds corresponding to the time to soak them in the vial with fixative solution. This was one of the most critical steps of the experiment, as it has been demonstrated that the time elapsed from death to fixative solution and the air exposure could greatly affect the final TEM results [49]. After an accurate literature review, a combination of fixatives containing 4% paraformaldehyde (p-FA) and 1% glutaraldehyde (GA) in 0.1 M sodium phosphate at pH 7.3 [50] was chosen. The small percentage of GA allows a good fixation but also a great preservation of samples over time. Since the fixative solution was highly toxic, facial protection was mandatory during this procedure.

The hemisected eyes were fixated for at least 48 hours. In order not to affect the dark-adapted samples with light, all the DA vials were stored in a dark box (Fig. 16).



Figure 16 – Box with black taped glass vials filled with fixative solution containing hemisected DA eyes

The hemisected eyeball (incised with a fine knife at the corneal level to allow for the fixative solution to penetrate inside) was chosen, rather than the entire eyeball, because it was observed under the light microscopy that the latter showed more detachment between the retina and the choroid, thus affecting the natural biological morphology (Fig. 17 C).

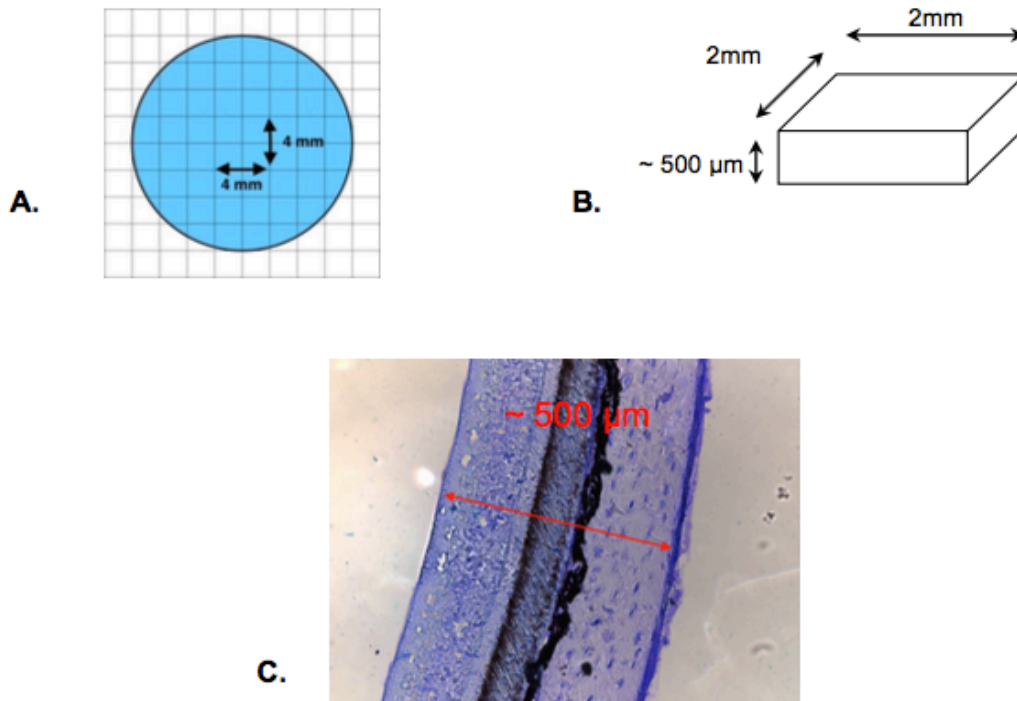


Figure 17 - Model of hemisected eyeball.

(A) Circular perimeter and grid obtainable thank to cryosection. (B) actual lengths of different sides of the parallelepiped samples. (C) 40X light microscope magnification of a 10 μm slice. Absence of detachment in the complex retina-choroid-sclera length (crystal violet stained)

Cryosectioning

After fixation, the samples were cryosectioned. Each hemisected eye has been transferred from fixative to 300 μl 2.3 M sucrose (Sucrose 99%, @SIGMA life science) in 0.1 M sodium phosphate buffer pH 7.3 at 4°C for 1 hour, then embedded and quick frozen in an O.C.T. compound (@Tissue-Tek) that facilitates the cutting procedure [50]. The samples were cut to form squared specimen of 2x2 mm of area (Fig. 17) while the width was approximately 500 μm (length of the complex retina-

choroid-sclera). Then, samples were washed from O.C.T. compound with a phosphate buffer saline solution (PBS) at pH 7.4 (®Gibco by life technologies) and then reinserted into the glass vial containing new fixative solution. It was essential to have different transversal and axial lengths in order to discriminate easily the cross-sectional area where photoreceptors were localized, which means where TEM was needed to be focused.

Post-fixation and dehydration

After cryosection, the samples were thawed and washed, and then underwent a secondary fixation (osmication), because lipid-rich structures (including membranes) are not well preserved by aldehydes [51]. This secondary fixation was performed using osmium tetroxide (OsO₄), which also helped to stabilize proteins. Sections were then dehydrated through a graded series of ethanols (30%, 50%, 70%, 90%, 95% and 3 x 100%) [50].

Subsequently, specimens were picked up on carbon-coated copper grids with 200 meshes and stained with alcoholic uranyl acetate, or with uranyl acetate followed by alkaline lead citrate [49], or with lead hydroxide [52]. Finally, samples were stained with saturated methanolic uranyl acetate (5 min) and Venable and Coggeshall's lead citrate (5 min) [50].

Transmission Electron Microscopy

In order to study the photoreceptors behavior at the subcellular level and clearly pinpoint the differences and similarities in discs' distances between the two groups of samples, an imaging device based on Transmission Electron Microscopy (TEM) was utilized. This technique was first introduced in 1932 by Knoll and Ruska [53], who were able to visualize internal structures of biological samples with a very fine resolution and without damaging them thanks to a highly-focused beam of electrons. The instrument utilized in the current research was the ®Life Science JEOL JEM-1220 TEM, a 120 kV transmission electron microscopy fitted with a LaB₆ electron source. Images were obtained using

a microscope at 80 kV. The microscope has a Gatan Es1000W 11MP CCD camera above the viewing chamber, which reads out into a Windows XP computer using Digital Micrograph software. It is composed by an electron source, and electromagnetic lens system, a sample holder and an imaging system.

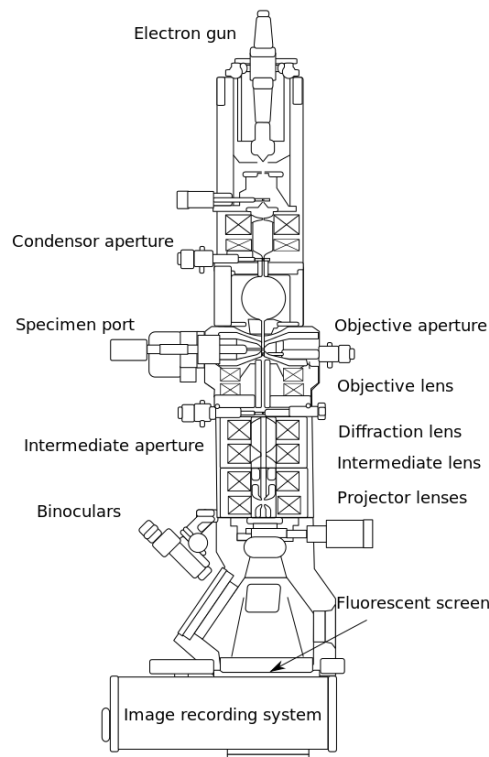


Figure 18 - Schematic Outline TEM. The electron source consists in a cathode and an anode. The cathode, composed by a tungsten filament, emits electrons when heated and the beam is then accelerated towards the specimen thanks to the positive anode [54]. After leaving the electron source, the beam is tightly focused using electromagnetic lenses that allow electrons with a small energy range to pass through the sample held in position by the sample holder, a platform with a mechanical arm. Lastly, the electrons after having crossed the sample impact onto the fluorescent screen where the image is formed.

Reprinted with permission. Open Source:

https://en.wikipedia.org/wiki/Transmission_electron_microscopy#/media/File:Scheme_TEM_en.svg

Physical Principles and Parameters

In a TEM, the electrons that constitute the beam pass through a section where the vacuum has been previously created, and then cross the sample. The sample thickness needs to be extremely reduced, in the range between 50 and few hundreds nm, in order to allow the beam to pass through it [55]. The

analyzed samples indeed had a thickness of around 70 nm.

The resolving power (the minimum distance between two points that can be resolved) is around 0.2 nm, more than 500 thousand times greater than that of the human eye. This type of microscope is provided, along the electro-optical axis, with a complex system that exploits the modification of electrical and magnetic fields [56], thus driving electrons through magnetic "lenses" necessary to enlarge the electron beam considerably to obtain magnified images. Additionally, electrostatic fields can cause the electrons to be deflected through a constant angle [57].

As previously noted, the sample consists of very thin sections, positioned on a small disk of fenestrated copper to form a network (the "screen" used had 200 meshes) so that the section can be observed between its meshes without interposition of glass that would not be crossed by the electrons. After having crossed the specimen the electron beam struck a fluorescent electron-sensitive screen projecting on it a greatly enlarged real image of the specimen.

This microscopy provides images in grey scale, which were further processed for the image analysis. The used accelerating voltage was 80 kV, high enough to have good resolution but not too strong to damage the samples. Different magnifications were explored, from the 2000 X for the visualization of the entire photoreceptor to the 250,000 X for the detailed analysis of disc's characteristics. The exposure time was set at 2.0 s while the objective lens presented a focal length of 1.9 mm and a minimum focus step of 0.25 nm.

Image analysis

After the TEM images were obtained, a pre-processing step was necessary to eliminate the background noise and to enhance image quality. Accordingly, both brightness and contrast were augmented by 25 %. It is known that these procedures simplify the image content, removing some information and condensing it in a smaller scale of grey levels, but it was necessary to have a better

visualization of the boundaries for further steps. In Fig. 19 the original image and the modified one are reported, with augmented contrast and exposure, which allowed to carry out a more detailed and precise analysis.

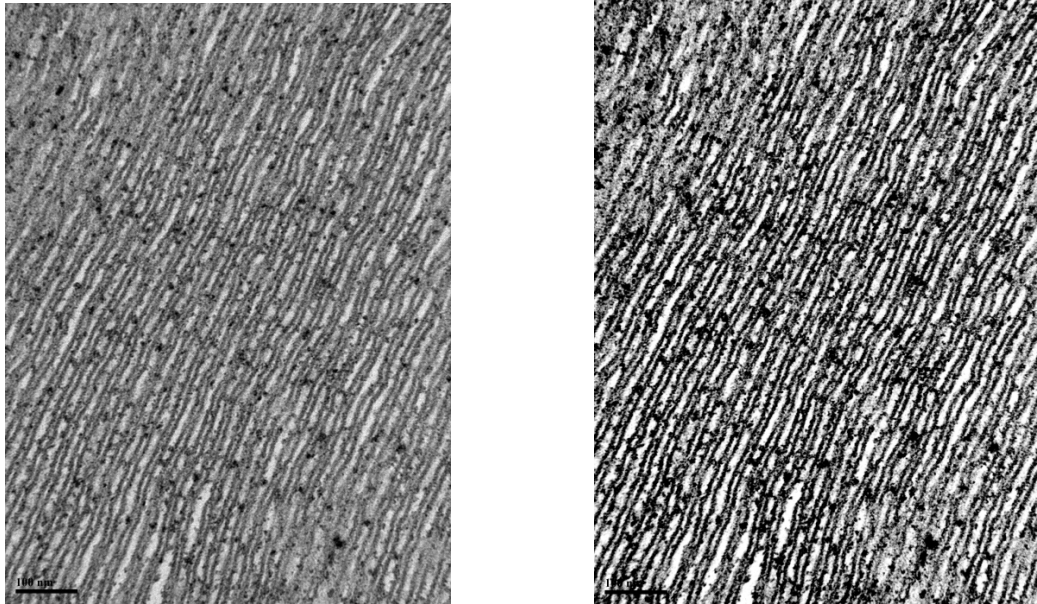


Figure 19 - Original (left) and modified (right) DA image obtained from the Central OS of the second DA eye.

In Fig. 20 are shown, instead, the histograms of the above images. Contrast and brightness modification caused a worsening of the image content, by saturating part of the videointensity range, but as already said, it was the only way to calculate distances.

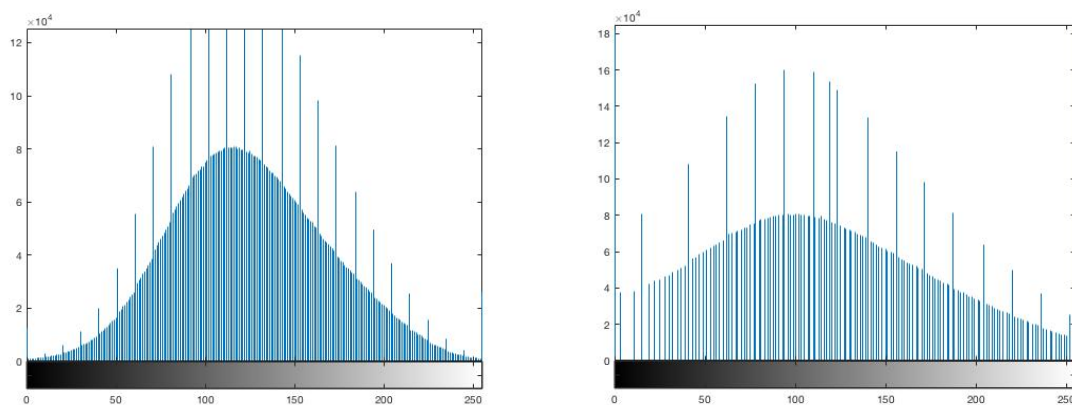


Figure 20 – On the left the original histogram, while on the right the histogram of the modified image.

It is important to mention that all the images underwent the exact same sequence of operations: although some information was lost, every image was consistent with this analysis and could be compared with the others. The images were manually analyzed using ImageJ (ver. 1.50i) [58]. Different TEM magnification scales have been explored: 2500 X, 8000 X, 100 kX, 150 kX, 200 kX and 250 kX. The lower magnification was used to obtain images of the overall photoreceptors while the others were used to obtain the details and characteristics of photoreceptor OS. Image size is equal to 2672 x 3608 pixels, while the $\Delta = \text{nm/pixel}$ (pixel resolution) varies accordingly with applied magnifications, spanning from $\Delta=0.21 \text{ nm/pixel}$ for the 250 kX to $\Delta=0.54 \text{ nm/pixel}$ for 100 kX images (pixel resolution for lower magnifications is not specified because those images were not used for distance calculation). The lower the Δ the better, but increasing the magnification increases also the blurring effect; for this reason, most of the images analyzed were obtained with 150 kX ($\Delta=0.36$) and 200 kX ($\Delta=0.27$), where the resolution was high enough together with an acceptable blur. The following figures (21-26) show examples of images obtained with different magnifications.

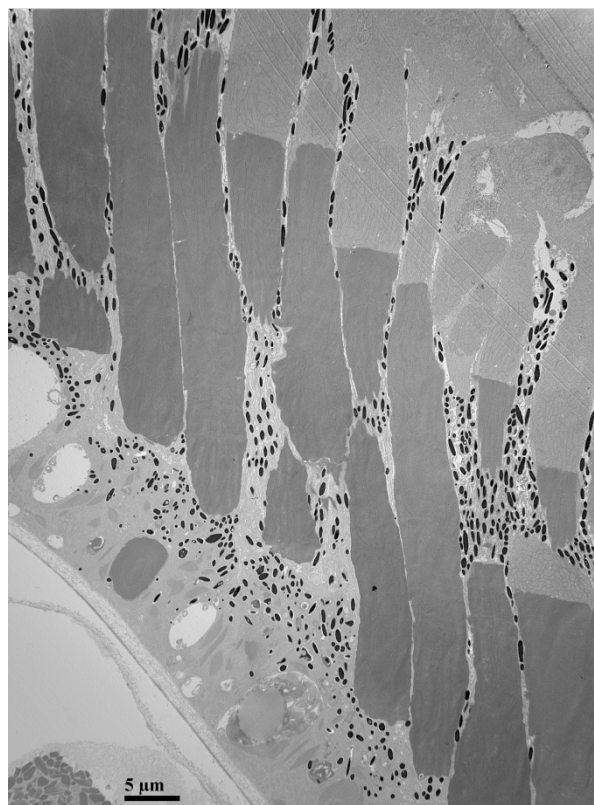


Figure 21 – TEM image, 2500 X magnification

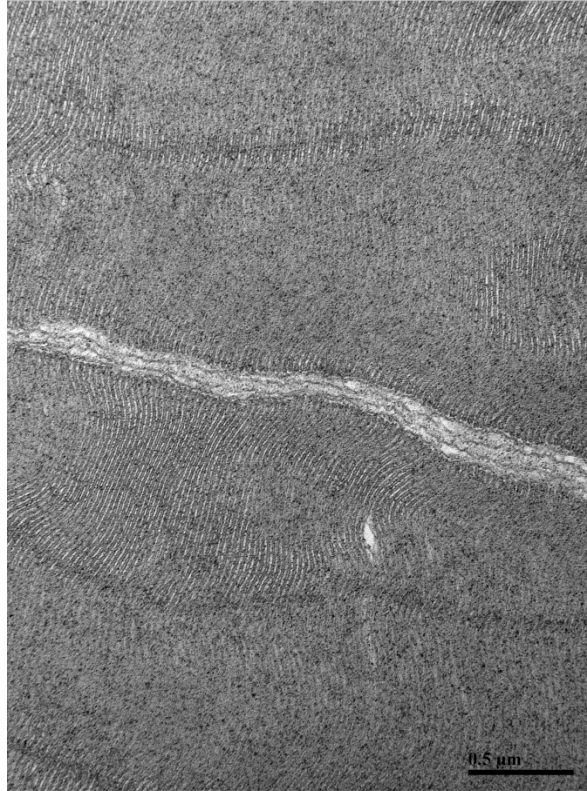


Figure 22 – TEM image, 80 kX magnification



Figure 23 – TEM image, 100 kX magnification



Figure 24 - TEM image, 150 kX magnification

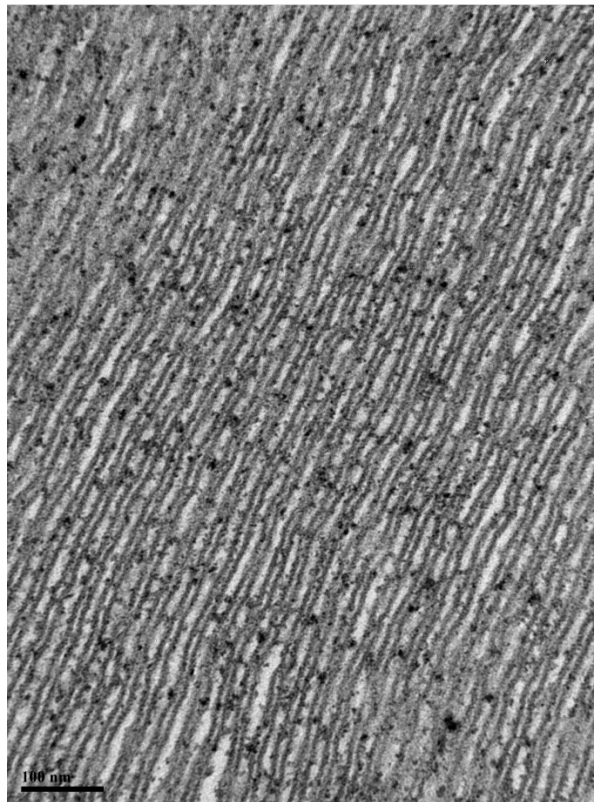


Figure 25 - TEM image, 200 kX magnification

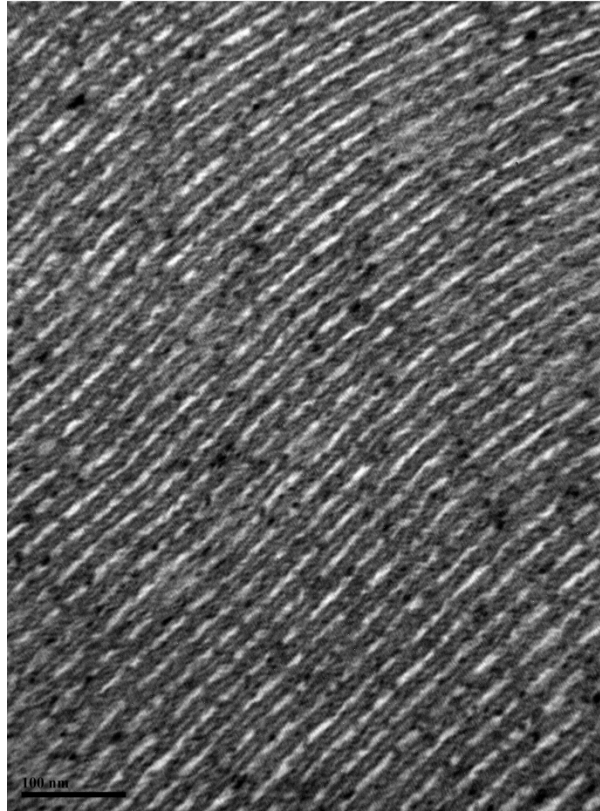


Figure 26 - TEM image, 250 kX magnification

We have devised a novel definition of photoreceptor disc distance, as well as novel algorithms for its computation from TEM images. The aim was to be as objective as possible and to create a flow of processes that could be easily followed by both expert and non-expert users. In a first step the distance estimates (both *interdiscs* and *intradisc*) were obtained manually. A second step of the study has been devoted on implementing an automatic MATLAB® routine able to carry out distance estimation automatically. Both manual and automatic algorithms are compared in the Results section.

One of the main drawbacks in the manual procedure is due to the fact that estimated distances are biased by the operator, and an inter-variability between different users has been observed (mean distance difference = 1.24 ± 0.67). To minimize these biases the following algorithm was devised:

- Images were divided into 400 smaller region of interest (ROI) of rectangular shape, with length = 133 pixels and width = 180 pixels, and labelled from 1 to 400 starting, from the left

corner of the first row (the first rectangle of the second row was the 21st);

- the MATLAB function $R = \text{randi}(400,50,1)$ was used in order to obtain 50 random integer numbers between 1 to 400, corresponding to the ROI labels that the operator will manually analyze;
- From the randomly chosen 50 ROIs, the first 20 in which discs could be distinguished were analyzed by measuring for each one *interdiscs* distance and one *intradisc* distance.

Following these steps, the discs to be analyzed are not chosen by the user, but they are randomly selected, thus eliminating any bias from the operator's decisional process.

Thanks to the measurement bar displayed in every image, it was possible to translate the pixels in nm and obtain the Δ previously described. This passage entailed the use of an ImageJ®'s tool called *straight-line*: the measurement bar's lengths were first computed in pixels, and then translated in nm.

Fig. 27 shows an example of the procedure. For the computation of the *interdiscs* distance, the user had to position the two final spots of the ruler on the very first black borders of the membrane (Fig. 27 C). For the computation of the *intradisc* distance, manual calculation is shown in Fig. 27 D, where the two final spots of the ruler needed to be positioned with their internal edge overlapped to the two external black borders of the disc membrane. Two DA eyes and two LA ones, for a total of four eyes, were analyzed. For each eye, 50 images were obtained but only around half of them were taken into consideration for the analysis. In fact, some of the acquired images had to be discarded because they did not meet the minimum quality requirements. As a result, a total of 4286 distances were analyzed, 2143 *interdiscs* and 2143 *intradisc*.

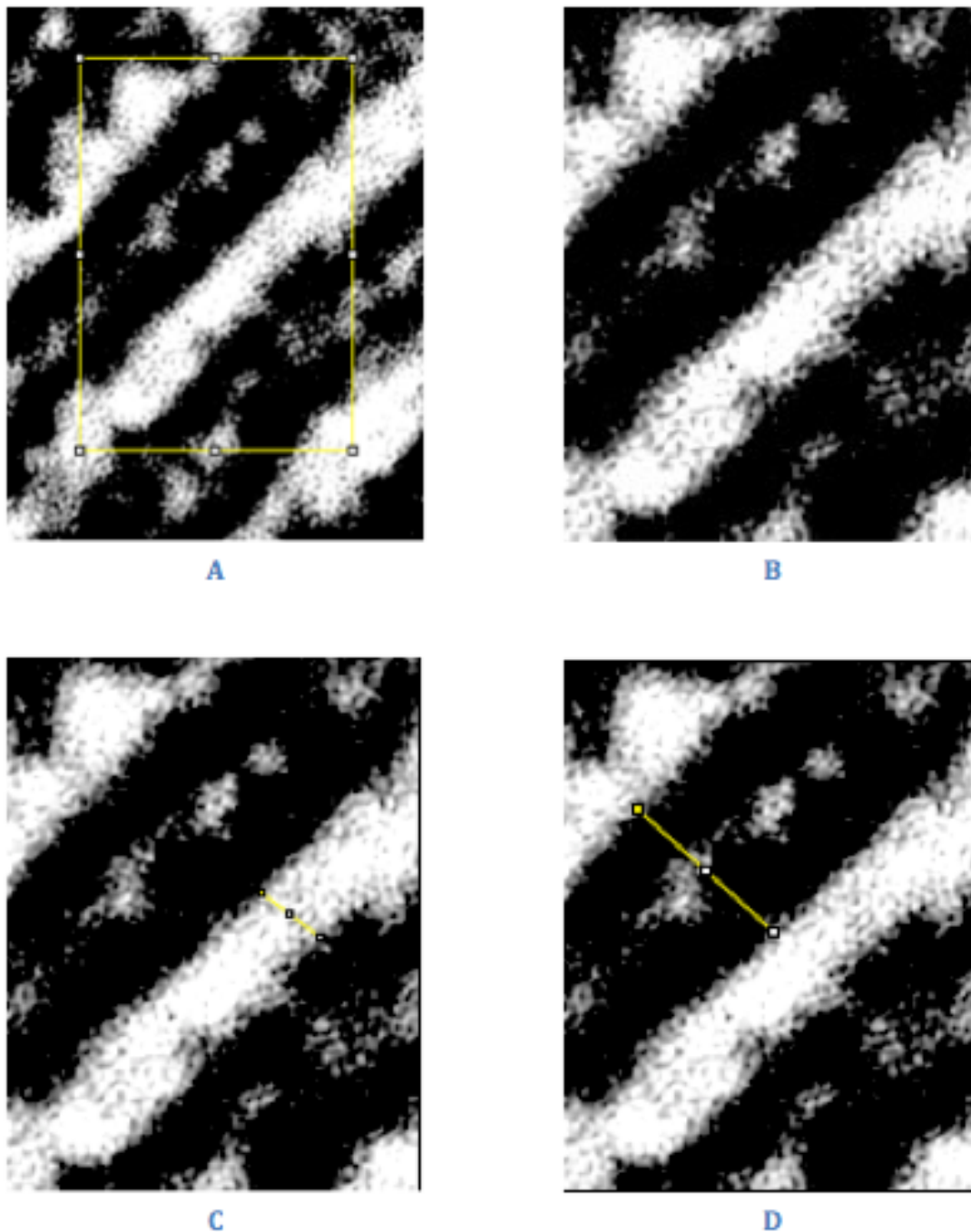


Figure 27 - (A) detail of one randomly selected rectangle (133.6 x 180.4 pixels). (B) Rectangle magnification (115%). (C) *Interdiscs* distance manual calculation, the two final spots of the ruler touch with their extreme part the very first black border of the membrane. (D) *Intradisc* distance manual calculation, the two final spots of the ruler touch with their internal edge the two external black borders of the disc membrane.

Both the LA and the DA images were further divided into 3 categories: Outer OS, Inner OS, and Central OS (Fig. 28), in order to compare each LA category with its DA counterpart and detect

differences or similarities according to the precise location of the discs within the photoreceptors.

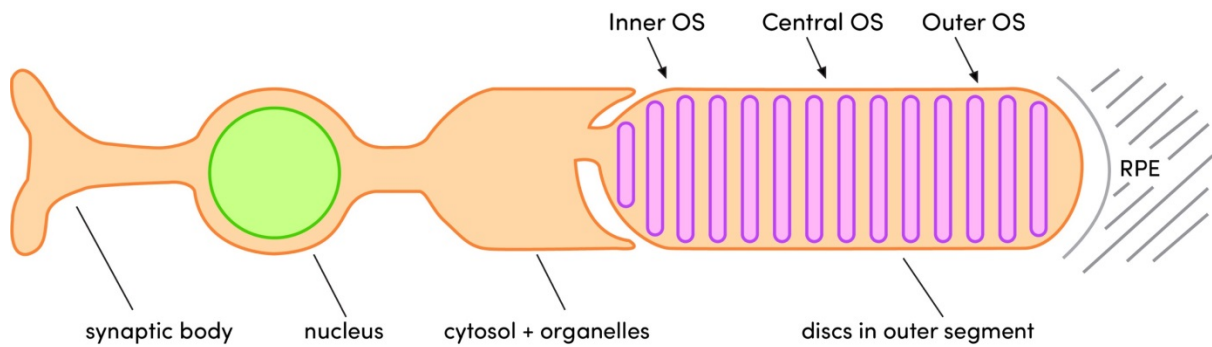


Figure 28 - Photoreceptor segments, from left to right: Synaptic Body, Inner Segment (nucleus, cytosol and organelles) and Outer Segment (OS) divided into: Inner OS, Central OS, Outer OS.

In order to identify a possible location where the shrinkage took place in each eye, the average of measurements obtained in the Outer, Inner and Central OS, respectively, were computed, both for the *intradisc* and the *interdiscs* distances. Then, the total mean, summing the results of these three categories was found, both for the *interdiscs* and for the *intradisc*. The two final results for each eye could be directly compared in order to assess the different behavior of the two groups of samples analyzed, Light Adapted and Dark Adapted. Finally, we averaged and statistically analyzed all *interdiscs* and *intradisc* LA and DA measurements to provide basic statistical summaries based on the resulting means and standard deviations related to each location (see Results section).

3.1 MATLAB® algorithm implementation

The aim of the MATLAB® algorithm was the automatic calculation of *interdiscs* and *intradisc* distances. From a thorough literature search, it was possible to ascertain that only few research groups throughout the world have focused their attention on the calculation of photoreceptor disc distances, mostly employing software for tomographic reconstruction (3D-modelling software like Amira® [59]). As previously described, the TEM images to be analyzed are characterized by a large size of 3608x2672 pixels, with a spatial resolution ranging from 0.21 nm/pixel to 0.54 nm/pixel, different videointensity patterns and orientations, and an 8-bit grayscale (256 grey levels).

The first step consisted in pre-processing of the images to remove possible noise. From the analysis of the image histogram, it was visible that the affecting noise was of “salt and pepper” type. To remove it, median filter with a size 21x21 was applied [68] (Fig. 29).

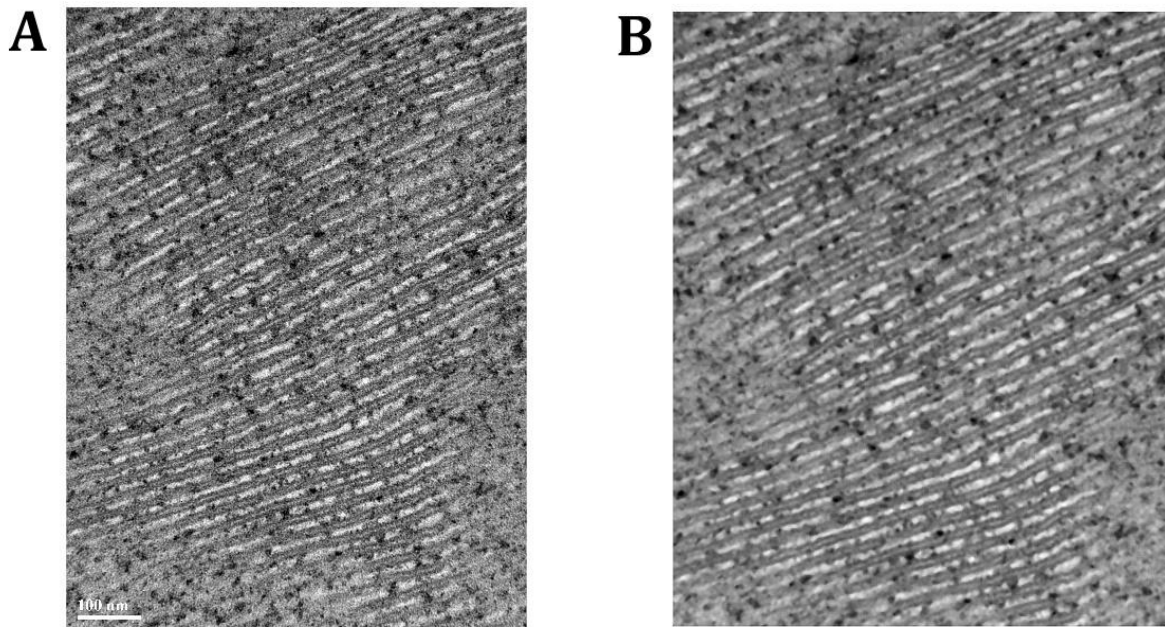


Figure 29 – A) Representative image with salt and pepper noise, before filtering. B) Same image after filtering.

The next step consisted in edge detection. Two different methods were tested: the simple computation of the gradient in x and y directions, and the Kirsch compass masks. The Kirsch method is one of the

most used algorithms for edge detection [69], although in some case its complexity can also become a drawback, as it is significantly more time consuming with respect to other methods. Furthermore, the results achieved with the Kirsch compass mask, for this specific analysis were worse than the ones obtained from the simplest gradient method (Fig. 30).

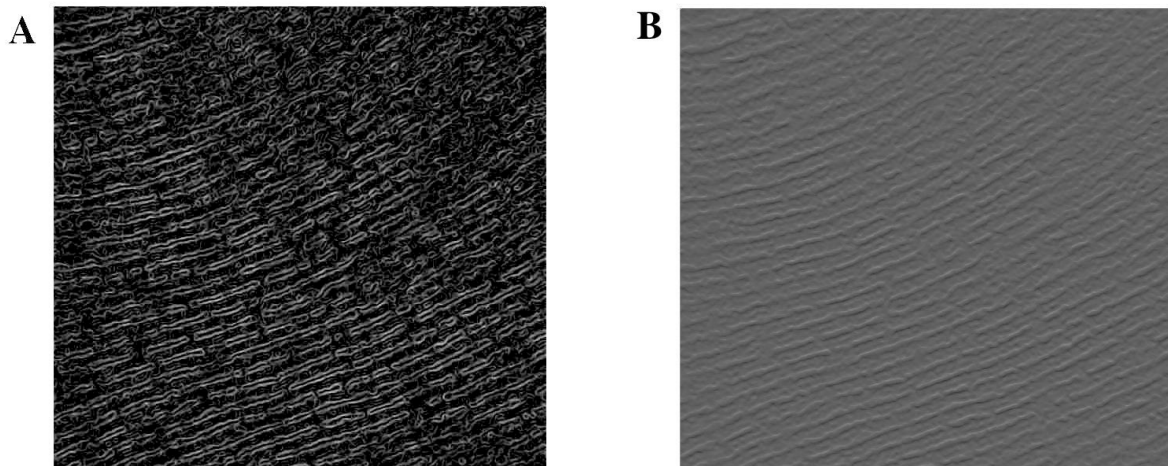


Figure 30 - A) Kirsch compass mask edge detection. B) Gradient in x edge detection.

After completing this preliminary evaluation, it was chosen to use the *imgradientxy* command in order to compute the mean gradient for both direction and their magnitude.

Subsequently, a subsampling of the images was implemented. The image was cropped in a series of ROIs with dimensions 150x150 pixels each. These dimensions were chosen to include approximately 2 discs each. This procedure was performed to find the best portions of the images with larger gradients. To this purpose, the information relevant to each ROI was stored in two look-up tables, one for abscissa and one for ordinate. These tables were used to speed up the process and the *integralImage* function in both directions was implemented. This summed area tables, indeed, are data structures for quickly and efficiently generating the sum of values in a rectangular subset of a grid [71]. In the image processing, this algorithm is called integral image and can be done in MATLAB® using the aforementioned command.

To select the areas with gradient levels providing sufficient information from the ones without, a

simple comparison of the mean gradient magnitude of the ROI with the mean gradient magnitude of the entire image was performed. A first visual color-coded procedure simply assigned the color green to the ROI where the mean gradient magnitude of the ROI was greater than the total average of the entire image, whereas all remaining areas were color-coded in red. An example is shown In Fig. 31.

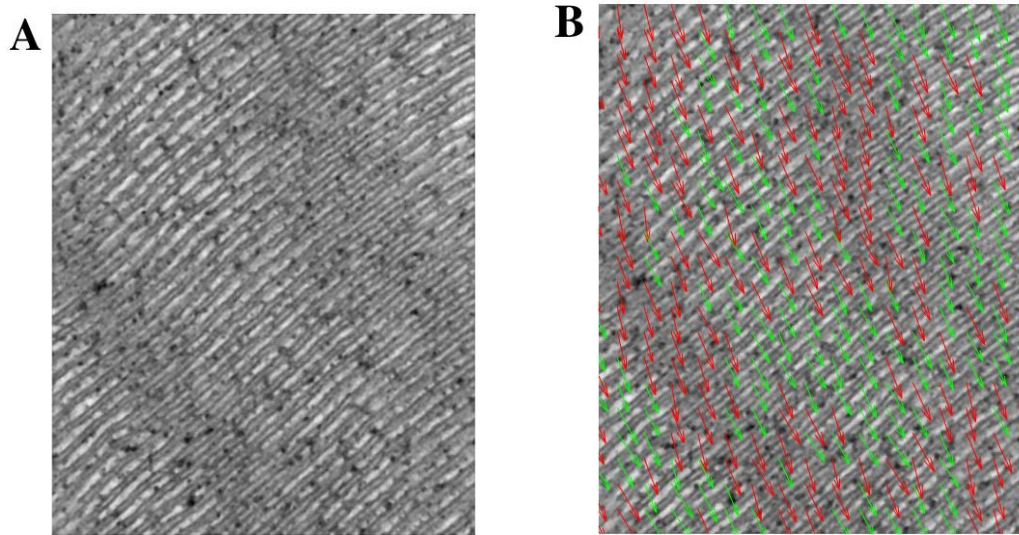


Figure 31 – A) Original filtrated image. B) Original filtrated image with gradients superimposed. Red arrows characterize ROIs with low values while green arrows represent ROIs with higher values.

The numerical procedure just ordered gradients computed for each ROI from highest to lowest, and selected only the top half ROIs for further analysis. For each of these ROIs, a discretizing step was achieved using the MATLAB®’s function *imbinarize*, specifically designed for 8-bit grayscale images with the hypothesis of bimodal histograms [70], using the Otsu’s method to find the threshold that best binarizes the image. Although all the ROIs were 8-bit grayscale, their histograms were not bimodal; for this reason, the *kmeans* clustering function with $k=4$, was also tested. Mean *interdiscs* and *intradisc* results between the two approaches showed differences less than 0.4 nm. In Fig. 32, an example of the original image and the two binarized ROIs, one obtained with Otsu and the other one with the clustering method, are shown: it is worth noting that results from the two methods look very similar.



Figure 32 – On the left, original gray scale cropped image. In the middle, cropped binarized image obtained with Otsu's method. On the right, cropped binarized image obtained with *kmeans* function with $k=4$.

Binarized ROIs were also rotated of the same angle described by the gradient vector in order to obtain images with vertical black and white alternated lines to facilitate the following steps.

Finally, the distances were computed: first, the *interdiscs* distances were considered and then, the *intradisc* ones were derived. The implemented solution includes three steps. First, for each row of the image a pixel counting, from right to left, was performed so that the ones closer to the border (step black-white) were the ones with minimum values, while proceeding to the left, pixels were marked with higher numbers. Each pixel was marked with a number which represents its distance, in pixel, from the closer boundary. Then, the same procedure was repeated from the left side, from left to right. In the last step, the two previous results were put together and a comparative analysis between rows and columns was carried out. For each row, the pixel with the highest value was found scanning the horizontal line both from the left and from the right. That pixel represented, for each row, the point with maximum distance from the borders. Subsequently, all the columns were scanned and a mean value point, representing the center of the *interdiscs* space for each rectangle 150x150 pixels was found (Fig. 33). The *interdiscs* space distance was then computed by doubling this value. Hence slightly approximated, the results from each ROI were then averaged to have a more precise value.

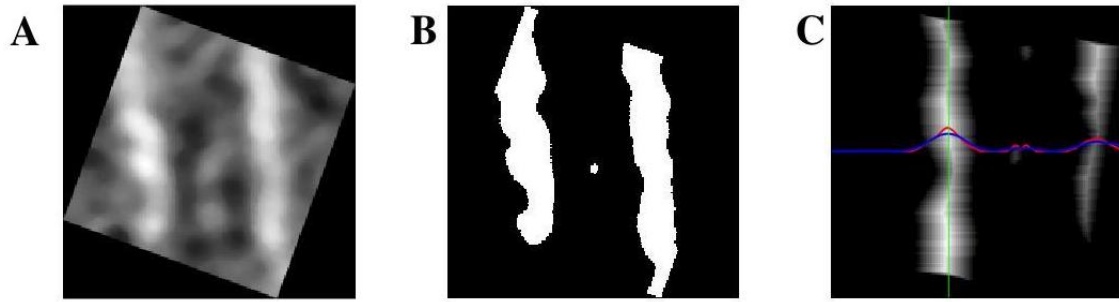


Figure 33 – A) Example of a rotated rectangle, the angle of rotation is given by the gradient vector. B) Binarized image of the rectangle shown in A). C) Result of the algorithm for distance calculation. The green line represents the averaged distance from the borders, while the red and blue line represent respectively the signal (peaks/valleys according to white and black regions) unfiltered and filtered (moving mean 1D)

To compute the *intradisc* distance, the same algorithm was applied after inverting the histogram of the image, thus operating on its negative.

Finally, the numerical values were transformed from pixels to nm, based on the scale previously defined by the calculated image magnification.

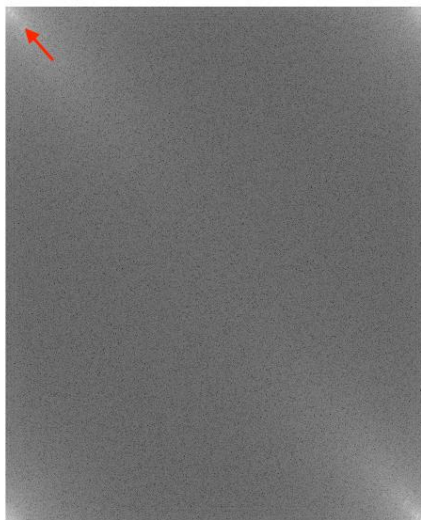


Figure 34 – Fourier Transform magnitude

To further validate the calculated distances, a spatial frequency analysis approach was carried out. The aim of this last step was to find the frequency peaks corresponding to changes in video-intensity through the ROI with a specific period, due to alternation between black (*intradiscs*) and white (*interdiscs*) spaces. Once the Discrete Fourier transform of the images was calculated by *fft2*, its magnitude was visualized (Fig. 34). By detecting the pixels with higher intensity, their location (x, y) were determined, from which the peak closer to 0 Hz was selected.

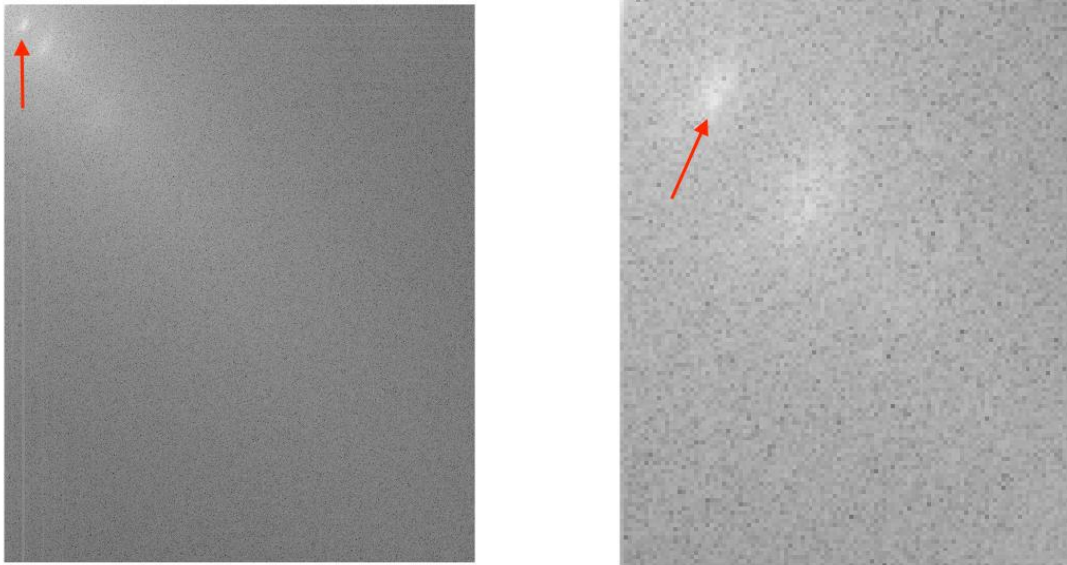


Figure 35 – Fourier transform magnitude details. On the left a magnified image where it is possible to visualize the peaks. On the right a further magnification to better pinpoint the first peak location.

The Euclidian distance from the 0 Hz center to the selected peak location (x,y) was computed by taking into consideration the different axis resolution, and by then transforming again from the frequency to the time domain to obtain the distance in nm. This procedure was carried out for twenty-five mages, and the final mean distance obtained by this calculation was 22 ± 2.67 nm. This distance represents one cycle of the sinusoid, which is the sum of the *interdiscs* and *intradisc* distances.

CHAPTER 4

RESULTS

Figs. 36 and 37 portray several details of images obtained with the different magnifications, relevant to outer, central and inner OS, with the related computed *interdiscs* and *intradisc* distances.

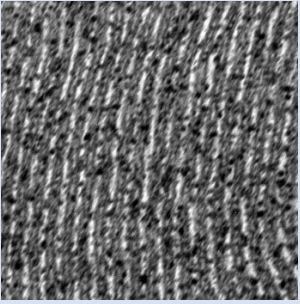
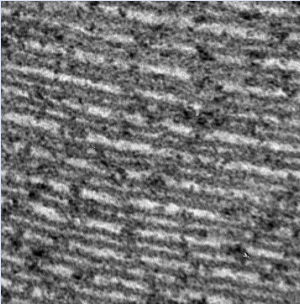
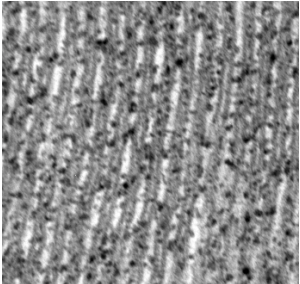
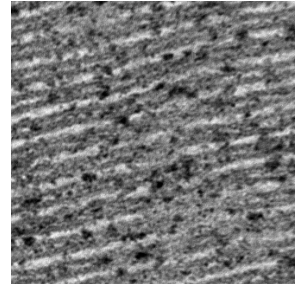
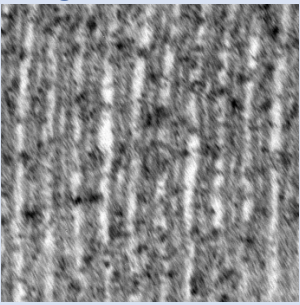
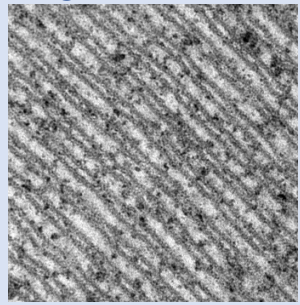
Location	1° LA EYE	2° LA EYE
OUTER OS	<p>Magnification: 150 KX</p>  <p>Inter = 4.615 ± 0.98 nm Intra = 12.178 ± 1.59 nm</p>	<p>Magnification: 200 KX</p>  <p>Inter = 4.857 ± 1.07 nm Intra = 12.739 ± 1.51 nm</p>
CENTRAL OS	<p>Magnification: 150 KX</p>  <p>Inter = 5.172 ± 1.66 nm Intra = 14.078 ± 1.61 nm</p>	<p>Magnification: 200 KX</p>  <p>Inter = 5.310 ± 1.24 nm Intra = 13.540 ± 1.80 nm</p>
INNER OS	<p>Magnification: 200 KX</p>  <p>Inter = 6.664 ± 1.46 nm Intra = 13.497 ± 1.94 nm</p>	<p>Magnification: 150 KX</p>  <p>Inter = 7.642 ± 2.30 nm Intra = 13.780 ± 1.93 nm</p>

Figure 36 – TEM images with mean values related to the first and second LA eye

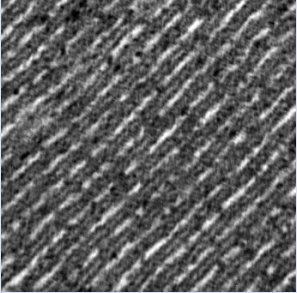
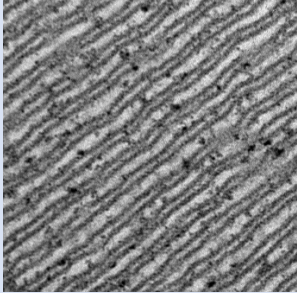
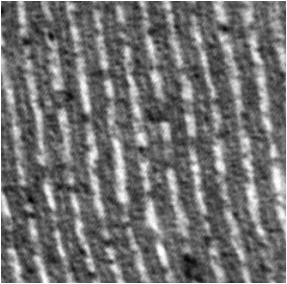
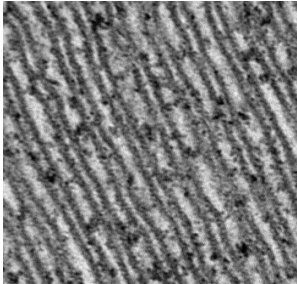
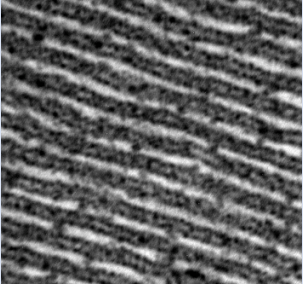
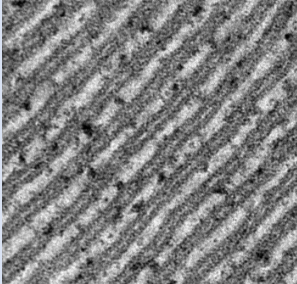
Location	1° DA EYE	2° DA EYE
OUTER OS	<p>Magnification: 150 KX</p>  <p>Inter = 6.466 ± 1.07 nm Intra = 12.678 ± 1.28 nm</p>	<p>Magnification: 150 KX</p>  <p>Inter = 7.785 ± 1.94 nm Intra = 13.422 ± 1.66 nm</p>
CENTRAL OS	<p>Magnification: 200 KX</p>  <p>Inter = 7.394 ± 1.36 nm Intra = 13.441 ± 1.23 nm</p>	<p>Magnification: 200 KX</p>  <p>Inter = 8.148 ± 1.73 nm Intra = 13.761 ± 1.61 nm</p>
INNER OS	<p>Magnification: 200 KX</p>  <p>Inter = 7.931 ± 1.48 nm Intra = 13.603 ± 1.60 nm</p>	<p>Magnification: 200 KX</p>  <p>Inter = 8.589 ± 1.91 nm Intra = 13.344 ± 1.29 nm</p>

Figure 37 - TEM images with mean values related to the first and second DA eye

The achieved pixel resolution was equal to $\Delta=0.27$ nm/pixels for the 200 KX, while for the 150 KX the resolution was equal to $\Delta=0.36$ nm/pixels.

All distances displayed in the previous two figures were calculated considering all the images (120) analyzed per each location. Forty images per location (Outer, Inner and Central) were considered,

and for each image 20 *interdiscs* and 20 *intradisc* measurements were computed by corresponding ROIs. It is important to highlight that the numbers reported above were obtained considering 60 images per group (LA and DA).

4.1 Statistical Analysis – *Interdiscs* distances

Multiple *t*-tests were performed to assess the statistical significance of the mean value considering different groups, samples and categories. In this paragraph, the performed analyses are shown considering the results obtained by the manual assessment of distances. In the following paragraph, the comparative study between distances calculated manually and automatically will be presented.

First of all, a comparative analysis taking into consideration the whole group of LA eyes and DA ones was performed.

The first two tailed unpaired *t*-test compared all the DA *interdiscs* measurements to all the LA ones, as obtained by several experiments summed together, thus assuming a Gaussian distribution and considering the standard deviations of each group.

The Null hypothesis (H^0) was that the difference of means between DA and LA was equal to 0. The resulting *p*-value equal to 3.445e-116, significantly smaller than the threshold value α , conventionally fixed at 0.05 or 5 %, indicated a highly significant difference between the two groups of samples.

Details on all the parameters adopted in the tests can be found in [APPENDIX C].

In Fig. 38 the bar plot concerning the above explained *t*-test is reported. DA mean *interdiscs* distance assessed was 7.750 ± 1.79 nm while the LA one was equal to 5.803 ± 1.88 nm. Standard deviations are shown for each plot.

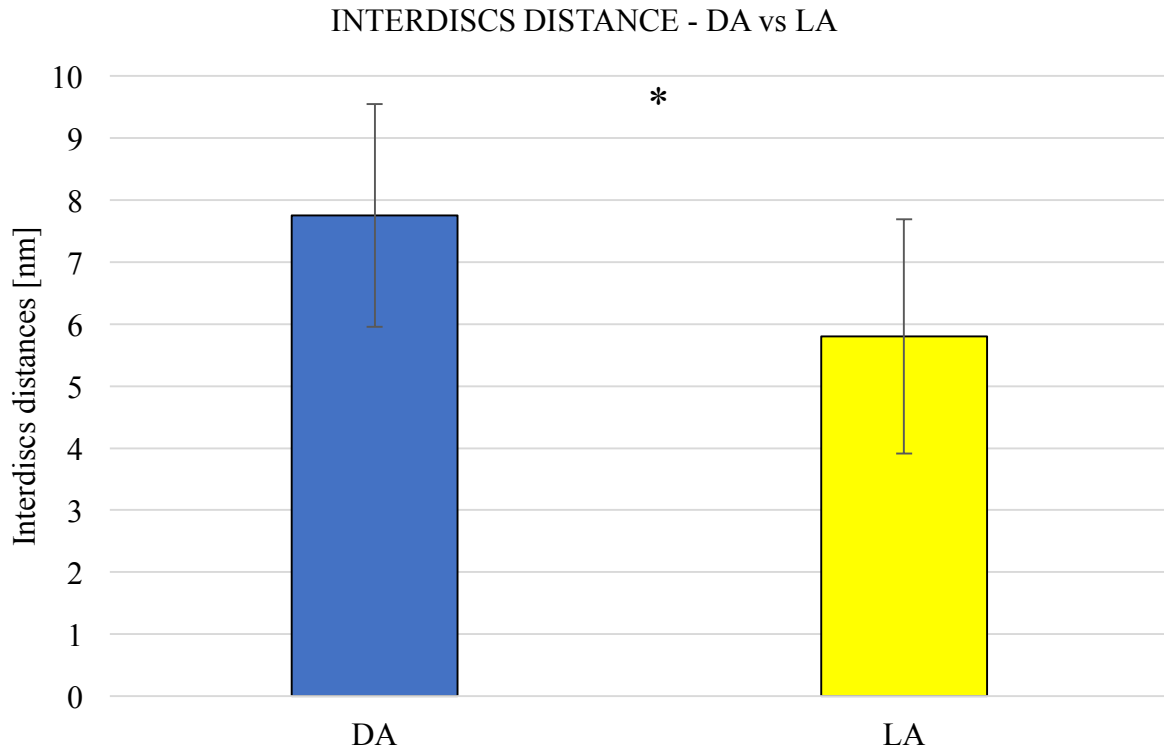


Figure 38 - Bar plot of the DA vs. LA *interdiscs* mean distances with superimposed standard deviation bars. Statistical significance is highlighted by *.

Other tests were performed to understand the location most greatly affected by these variations, by comparing DA Outer, Central and Inner vs the corresponding LA (see APPENDICES D, E and F]. All these tests confirmed significant mean *interdiscs* differences between DA and LA (See table II and Fig. 39)

TABLE II – INTERDISCS DISTANCES PER CATEGORY AND *t*-TESTS RESULTS

	Mean <i>Interdiscs</i> distances	Standard Deviation	Two-tailed <i>p</i> -value	H^0 : Difference of means = 0 (*: Significance)
DA Outer	7.211 nm	1.74	1.338e-98	Rejected *
LA Outer	4.800 nm	1.04		

	Mean <i>Interdiscs</i> distances	Standard Deviation	Two-tailed <i>p</i> -value	H^0 : Difference of means = 0
DA Central	7.933 nm	1.67	5.098e-69	Rejected *
LA Central	5.299 nm	1.42		
DA Inner	8.297 nm	1.76	1.636e-15	Rejected *
LA Inner	7.157 nm	2.036		

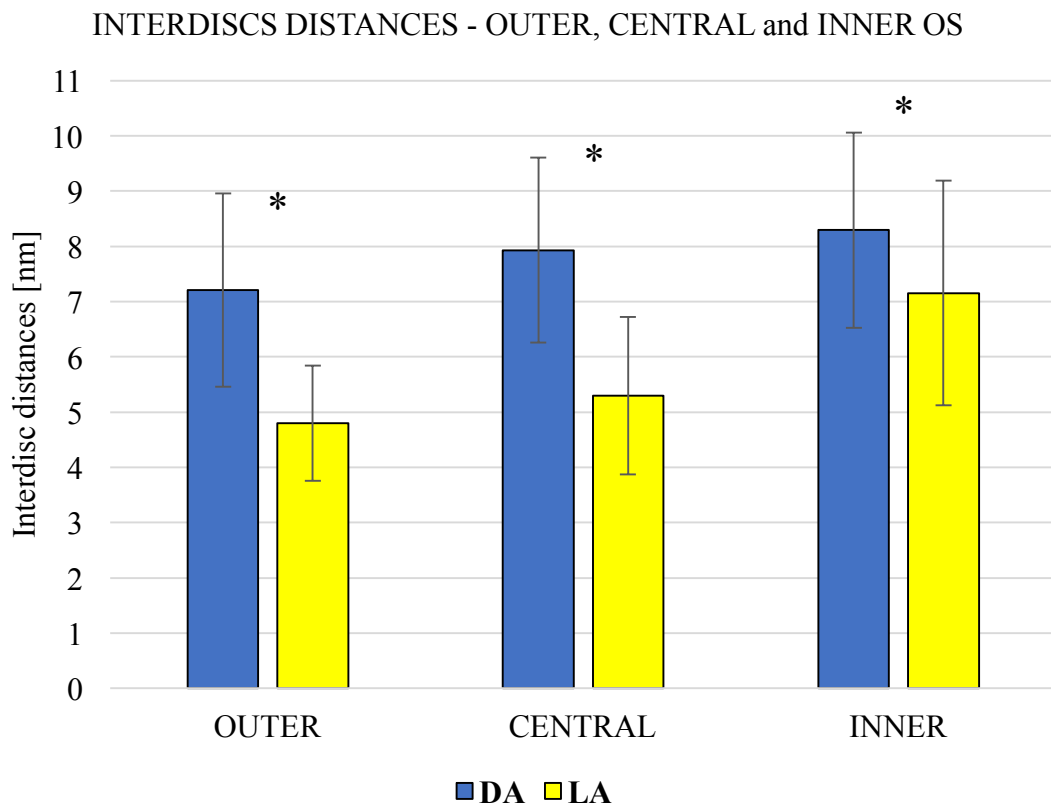


Figure 39 - *Interdiscs* bar plots (with superimposed std) of different categories showing differences between the two groups, DA and LA. Asterisks highlight the statistical significance.

It is worth noting a trend in the mean value, with lower *interdiscs* distances in the outer region slightly increasing towards the inner one until reaching the base of the OS in the inner areas. Moreover, for the three different categories, DA values were larger than LA.

For sake of completeness, in Fig. 40 is also reported the bar plot obtained from the two different experiments. The first experiment consisted in the examination of the first LA and DA eyes that were analyzed contemporaneously at the first TEM scope session. The second experiment was a repetition of it using two new LA and DA eyes.

The displayed behaviour is consistent with everything previously observed, *interdiscs* LA distances in both examinations resulted smaller than the DA counterparts.

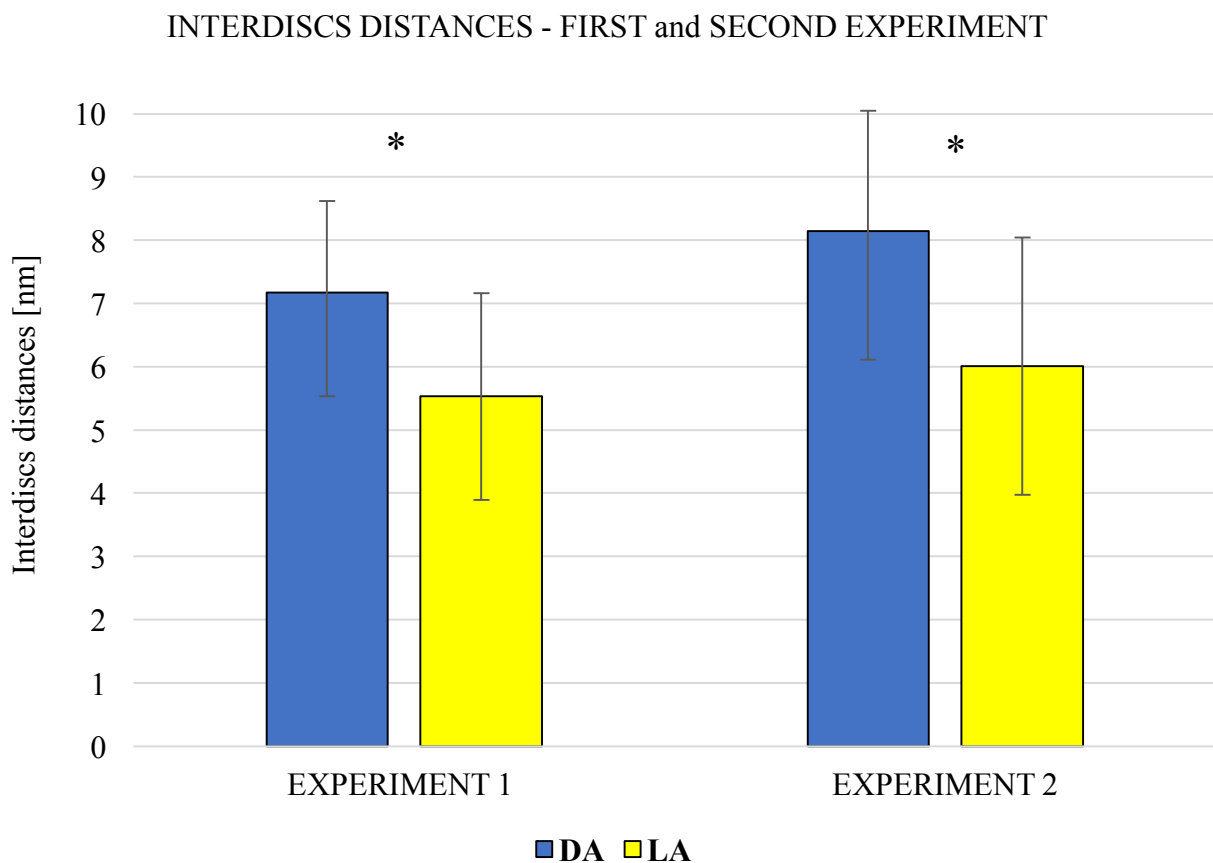


Figure 40 – *Interdiscs* bar plots (with superimposed std) of the two experiments between the two groups, DA and LA.

Asterisks highlight the statistical significance

4.2 Statistical Analysis – Intradisc distances

As far as *intradisc* distances are concerned, the same statistical tests were carried out. Firstly, an unpaired t-test was applied considering all DA and LA measurements to compare these groups. The resulting *p*-value was equal to 3.194e-05, meaning that the two samples were different. All parameters adopted are reported in [APPENDIX G]. Mean *intradisc* LA distance was equal to 13.668 ± 1.84 nm while mean *intradisc* DA distance was 13.362 ± 1.52 nm.

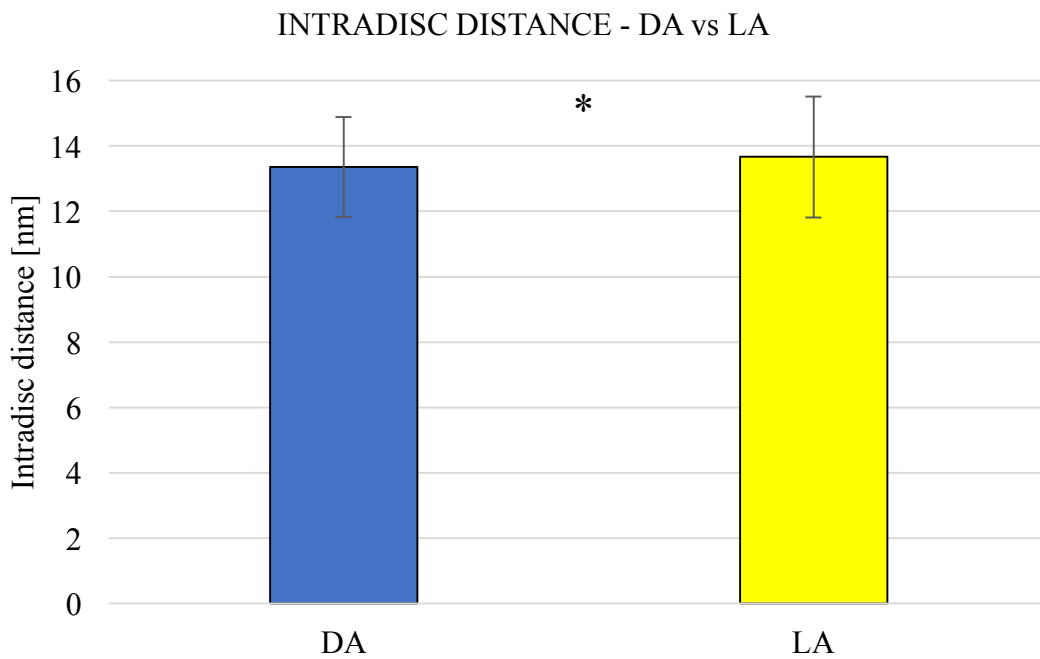
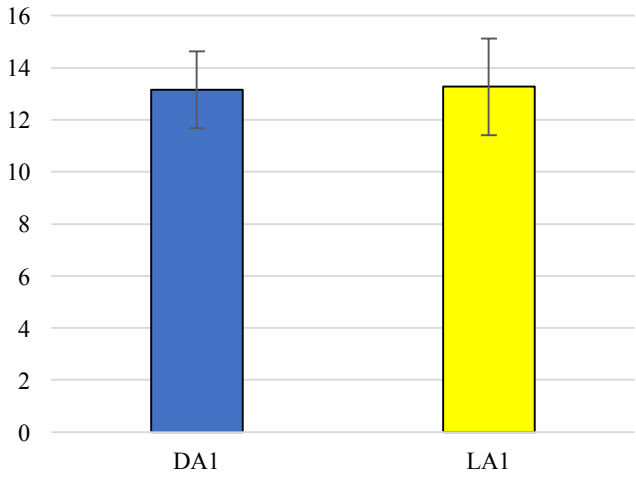


Figure 41 - Mean *intradisc* distance bar plot LA vs DA with superimposed std. Asterisks highlight the statistical significance.

The critical issue of this result stands in the fact that a similar behavior of these two elements was expected while instead the result showed a statistical difference considering the mean of all *intradisc* distances. Indeed, from the values obtained both automatically and manually, the *intradisc* measurements between LA and DA samples were very similar, especially comparing data from the same experiment or from the same location. To further investigate this behavior other tests were planned: *t*-tests between experiments, *t*-tests considering the locations, a linear regression and a modified *t*-test.

First, a comparative analysis between DA and LA *intradisc* measurements obtained by the first experiment was performed. Then, the first DA against the second LA it was considered, then the second DA against the first LA, and the last conducted analysis took into consideration the second DA eye against the second LA (APPENDICES H, I, L, M). As a matter of fact, something interesting was found: two of the four analyses resulted in the non-rejection of the H^0 , which in turn meant that in half of the tests carried out the means did not show statistical differences (see Fig. 42). These tests were not done to find a random significance considering a subset of measurements but instead were carried out to have a deeper understanding on the *intradisc* behavior.

The following figures display the bar plots of the previously discussed *t*-tests. Graphs with asterisk were the significant ones, while in the other the null hypothesis is not rejected.

BARPLOTS	P-VALUE
<p style="text-align: center;">INTRADISC DISTANCE</p>  <p style="text-align: center;">DA1 LA1</p>	<p>DA 1° vs LA 1°: <i>p</i>-value: 0.3158</p> <p>Null hypothesis H^0 is not rejected, samples do not show differences</p>

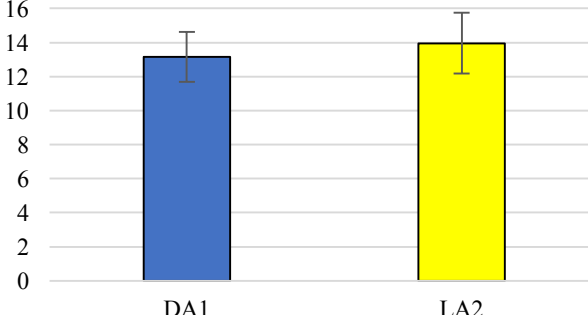
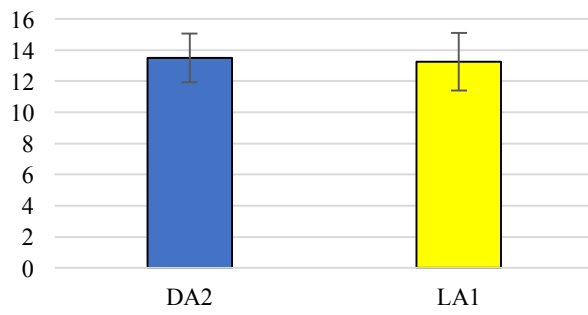
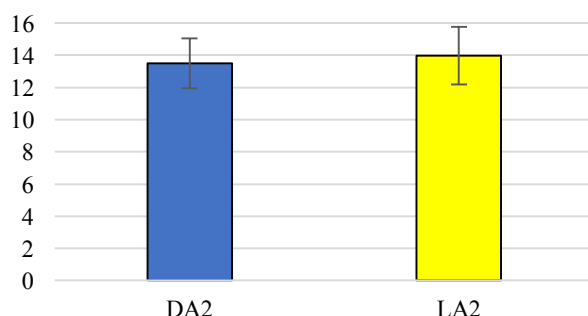
<p style="text-align: center;">INTRADISC DISTANCE</p> <p style="text-align: center;">*</p>  <table border="1" style="margin-left: auto; margin-right: auto;"> <thead> <tr> <th>Group</th> <th>Mean Distance</th> </tr> </thead> <tbody> <tr> <td>DA1</td> <td>~13.2</td> </tr> <tr> <td>LA2</td> <td>~14.0</td> </tr> </tbody> </table>	Group	Mean Distance	DA1	~13.2	LA2	~14.0	<p>DA 1° vs LA 2°:</p> <p><i>p</i>-value: 2.585e-15 *</p> <p>Null hypothesis H^0 is rejected, samples show differences</p>
Group	Mean Distance						
DA1	~13.2						
LA2	~14.0						
<p style="text-align: center;">INTRADISC DISTANCE</p>  <table border="1" style="margin-left: auto; margin-right: auto;"> <thead> <tr> <th>Group</th> <th>Mean Distance</th> </tr> </thead> <tbody> <tr> <td>DA2</td> <td>~13.5</td> </tr> <tr> <td>LA1</td> <td>~13.2</td> </tr> </tbody> </table>	Group	Mean Distance	DA2	~13.5	LA1	~13.2	<p>DA 2° vs LA 1°:</p> <p><i>p</i>-value: 0.05111</p> <p>Null hypothesis H^0 is not rejected, samples do not show differences</p>
Group	Mean Distance						
DA2	~13.5						
LA1	~13.2						
<p style="text-align: center;">INTRADISC DISTANCE</p> <p style="text-align: center;">*</p>  <table border="1" style="margin-left: auto; margin-right: auto;"> <thead> <tr> <th>Group</th> <th>Mean Distance</th> </tr> </thead> <tbody> <tr> <td>DA2</td> <td>~13.5</td> </tr> <tr> <td>LA2</td> <td>~14.0</td> </tr> </tbody> </table>	Group	Mean Distance	DA2	~13.5	LA2	~14.0	<p>DA 2° vs LA 2°:</p> <p><i>p</i>-value: 2.617e-06 *</p> <p>Null hypothesis H^0 is rejected, samples show differences</p>
Group	Mean Distance						
DA2	~13.5						
LA2	~14.0						

Figure 42 - Barplots of different tests with superimposed s.d. Asterisks highlighted statistical significance

In Fig. 43 the bar plots with the respective standard deviations of the *intradisc* distances differentiated per location are reported. The null hypothesis considered was still the same.

As far as the Outer location concern, the conducted *t*-test resulted in the non-rejection of the null hypothesis, meaning that the two groups did not show differences and that the test was not significant.

At the same time the test carried out on the Central and Inner location showed a statistical significance.

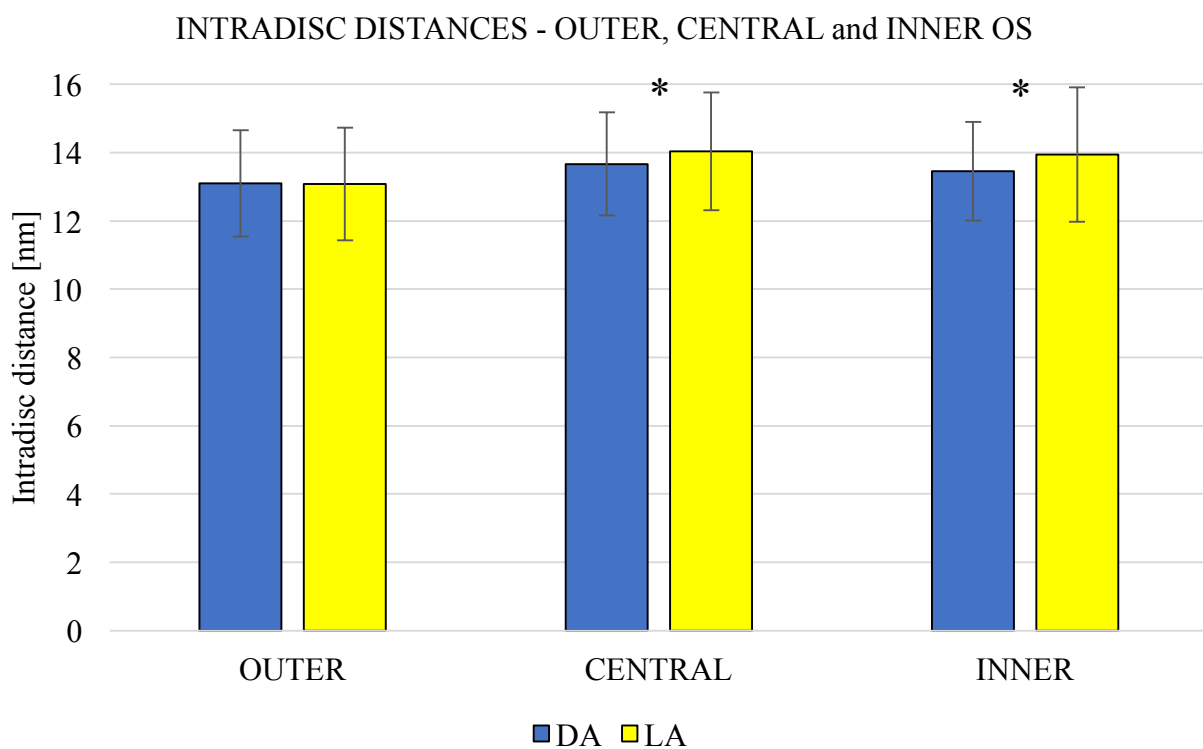


Figure 43 - *Intradisc* bar plots of different categories. Standard deviations bars are superimposed. Asterisks highlight the statistical significance

There were also conducted *t*-tests differentiated per category and per experiment. Also in this case, the results were ambiguous: some of them were significant while others were not.

To further test the *intradisc* behavior, a linear regression was applied, considering all the observations, both the *intradisc* and the *interdiscs*. The multiple linear regression is a fast and easy

method for predicting a quantitative response Y , based on a multiple predictors $X_1 \dots X_i$, which has the following formula:

$$Y = \beta_0 + \beta_1 X_1 + \dots + \beta_i X_i \quad (4.1)$$

The linear regression adopted was:

$$D/L = \beta_0 + \beta_1 * INTRADISC + \beta_2 * INTERDISCS \quad (4.2)$$

Where D/L referred to the DA and LA and was the dependent variable, $INTRADISC$ and $INTERDISCS$ were the independent variables and β_i were the multiplicative coefficients or parameters. The coefficients were estimated to find the hyperplane that interpolated in the best way the "cloud" of experimental points: the aim was to find the hyperplane that minimizes the sum of squared distances from the points. This parameter estimation approach is defined in the literature as OLS (Ordinary Least Squares).

The goal (and the expectation) of this analysis was to prove that the *interdiscs* measurements were statistically more important in respect to the *intradisc* ones, which led to the conclusion that the coefficient β_1 should have been smaller respect the coefficient β_2 . The test went as expected, indeed β_1 resulted equal to -0.044 while β_2 was 0.116 [APPENDIX N].

This result suggested that the differences in the DA/LA samples were more dependent on the *interdiscs* measurements than on the *intradisc* ones. At the same time both the p -values calculated for this two coefficients were significant, so further investigations were needed to prove if *intradisc* differences between groups were significant or not.

The linear regression gave another piece of information about the *interdiscs* and *intradisc* distances but still not strong enough to accurately state that the *intradisc* distances of the DA and LA sample were almost identical.

As the best $\Delta = \text{nm/pixels}$ achievable ($\Delta=0.217 \text{ nm/pixels}$) was the one obtained with a TEM magnification of $250,000 \text{ X}$, but at expenses of the long exposure time causing blurry images, most of the pictures were acquired with lower magnification as $200,000 \text{ X}$ or $150,000 \text{ X}$, with $\Delta = 0.27$

nm/pixels and $\Delta = 0.36$ nm/pixels, respectively. Considering that 70 % of the images were taken with those two magnifications (35 % and 35 %), 20 % with 100,000 X and the remaining 10 % with a magnification equal to 250,000 X, knowing the Δ of each one, their weighted average resulted in $\Delta' = 0.353$ nm/pixels. This value represents the minimum averaged resolving distance of all the samples. A modified *t*-test was then applied to test the null hypothesis that the difference of means was equal to $\Delta' = 0.353$ nm/pixels, representing the maximal sensitivity of the instruments.

The *t*-test resulted in the non-rejection of the null hypothesis, which meant that the *intradisc* distances of the LA and DA samples were statistically not different considering the sensitivity of the utilized instrumentation, and also the variability in the measures due to the manual calculation of distances ($\Delta' = 0.353$ nm/pixels represents a difference of one pixel in the image!) [see APPENDIX O].

Here are two tables containing all the most important values obtained. Special attention is given to the *interdiscs* and *intradisc* total mean distances.

TABLE III – INTERDISCS MEAN VALUES MANUALLY OBTAINED (*: statistical significance of the unpaired *t*-test)

Mean Distances	Dark Adapted (DA) [nm]	Light Adapted (LA) [nm]	* of the unpaired <i>t</i>-test
<i>Interdiscs Outer</i>	7.211 ± 1.74	4.800 ± 1.04	Significant
<i>Interdiscs Central</i>	7.933 ± 1.67	5.299 ± 1.42	Significant
<i>Interdiscs Inner</i>	8.297 ± 1.76	7.157 ± 2.03	Significant
<u><i>Interdiscs Total</i></u>	<u>7.750 ± 1.79</u>	<u>5.803 ± 1.88</u>	<u>Significant</u>

TABLE IV – INTRADISC MEAN VALUES MANUALLY OBTAINED (*: statistical significance of the unpaired *t*-test)

Mean Distances	Dark Adapted (DA) [nm]	Light Adapted (LA) [nm]	* of the unpaired <i>t</i> -test
<i>Intradisc Outer</i>	13.099 ± 1.55	13.076 ± 1.65	Not Significant
<i>Intradisc Central</i>	13.669 ± 1.51	14.035 ± 1.73	Significant ¹
<i>Intradisc Inner</i>	13.459 ± 1.44	13.943 ± 1.97	Significant ¹
<u><i>Intradisc Total</i></u>	<u>13.362 ± 1.52</u>	<u>13.668 ± 1.84</u>	<u>Significant¹</u>

1. Statistical significance related to the null hypothesis H^0 : difference of means equal to 0. All the above described tests considering the instrumentation sensitivity for *intradisc* distances were not significant.

4.3 Comparison between manually and automatically obtained results

As already described in material and methods section, two automatic thresholding method for image binarization, Otsu's and the *kmeans* clustering, were applied. In the following table the obtained results for both are reported, compared with the manual ones.

TABLE V – INTERDISCS AND INTRADISCS DISTANCES, MANUAL AND AUTOMATIC RESULTS

	Otsu [nm]	<i>Kmeans</i> [nm]	Manual [nm]
<i>Interdiscs DA Outer</i>	11.923 ± 0.89	11.631 ± 1.33	7.211 ± 1.74
<i>Interdiscs LA Outer</i>	10.075 ± 1.36	10.066 ± 1.01	4.800 ± 1.04
<i>Interdiscs DA Inner</i>	12.576 ± 1.53	12.817 ± 1.82	8.297 ± 1.76
<i>Interdiscs LA Inner</i>	12.605 ± 1.45	12.042 ± 1.37	7.157 ± 2.03

	Otsu [nm]	Kmeans [nm]	Manual [nm]
Intradisc DA Outer	21.623 ± 2.77	22.499 ± 3.61	13.099 ± 1.55
Intradisc LA Outer	21.726 ± 1.86	21.428 ± 1.91	13.076 ± 1.65
Intradisc DA Inner	22.643 ± 3.27	22.623 ± 3.11	13.459 ± 1.44
Intradisc LA Inner	22.627 ± 2.41	22.309 ± 2.08	13.943 ± 1.97

As it can be seen in Table V, results achieved with the two automatic methods were very similar. Indeed, they were tested for significance and no differences between them were found. It is also worth noting that it was proved the congruency: automatic and manual results, although slightly different in their absolute values, displayed the same outcome in the difference between LA and DA samples, confirming the previous conclusions.

Multiple linear regressions between automatic and manual mean distances were carried out to further compare the used methods [APPENDICES R and S]. It was conducted an analysis comparing the differences between LA and DA *interdiscs* among methods, first taking into consideration Otsu's one against the manual and then comparing the latter with the *kmeans* measurements. The R^2 found in the first regression was 0.480, while the second resulted 0.452.

Two similar multiple linear regressions were also obtained for *intradisc* distances [APPENDICES T and U]. In the first case the R^2 was equal to 0.244 while in the second resulted 0.467.

Furthermore, in Table VI biases and limits agreements are showed

TABLE VI – BLAND-ALTMAN STATISTICAL APPROACH, BIASES AND LIMITS OF AGREEMENTS DISPLAYED

	BIASES [nm]	LIMITS OF AGREEMENT [nm]
E[DA OTSU, INTER – DA MANUAL, INTER]	4.621	4.621 ± (2*1.62)
E[DA KM, INTER – DA MANUAL, INTER]	4.595	4.595 ± (2*1.74)
E[LA OTSU, INTER – LA MANUAL, INTER]	5.935	5.935 ± (2*2.52)
E[LA KM, INTER – DA MANUAL, INTER]	5.911	5.911 ± (2*2.47)
E[DA OTSU, INTRA – DA MANUAL, INTRA]	8.850	8.850 ± (2*3.41)
E[DA KM, INTRA – DA MANUAL, INTRA]	8.829	8.829 ± (2*4.12)
E[LA OTSU, INTRA – LA MANUAL, INTRA]	9.126	9.126 ± (2*2.98)
E[LA KM, INTRA – LA MANUAL, INTRA]	9.145	9.145 ± (2*3.01)

Here are reported the *t*-tests conducted on MATLAB®'s outputs, the bar plots with standard deviations and the comparison with manual ones.

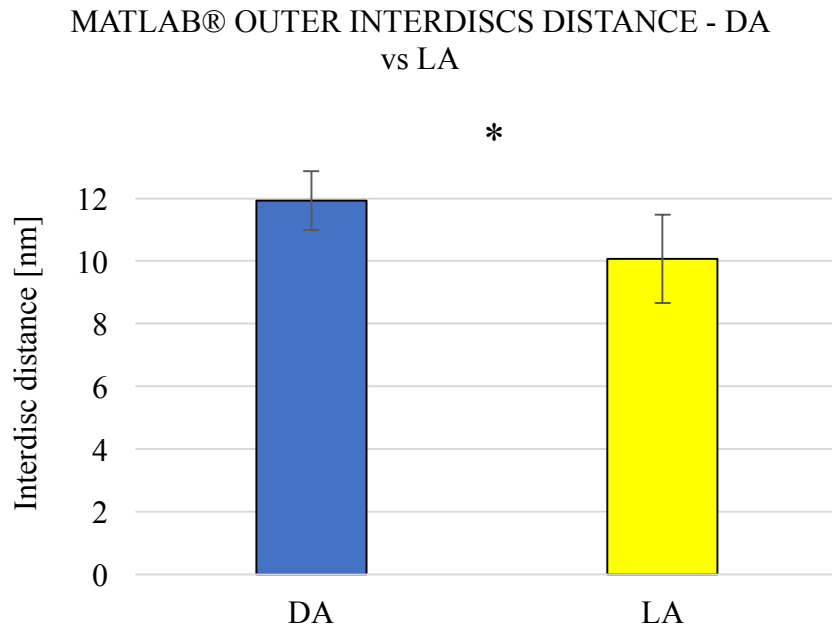


Figure 44 - Bar plot of the DA vs. LA *interdiscs* mean distances obtained using MATLAB®. Standard deviations bars are superimposed to the histograms. Asterisks highlight the statistical significance

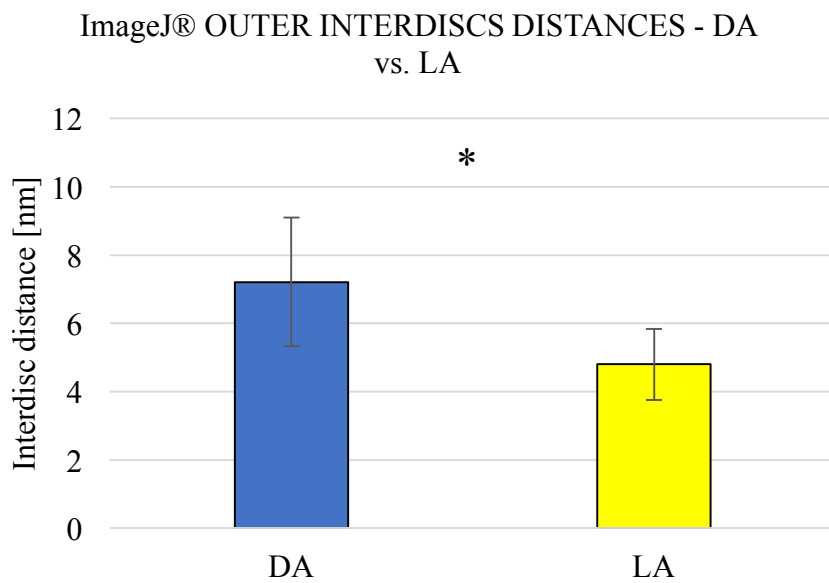


Figure 45 - Bar plot of the DA vs. LA *interdiscs* mean distances obtained using ImageJ®. Standard deviations bars are superimposed to the graphs. Asterisks highlight the statistical significance

In Figs. 44 and 45 the two bar plots regarding the mean *interdiscs* distances between the two samples, obtained automatically and manually, are shown. It is possible to notice the differences in the absolute values:

TABLE VII –MEAN OUTER INTERDISCS DISTANCES OBTAINED WITH THE TWO METHODS

	DA [nm]	LA [nm]	<i>t</i>-test significance
MATLAB®	11.928 ± 0.93	10.075 ± 1.41	*
ImageJ®	7.211 ± 1.88	4.800 ± 1.04	*

Both *t*-tests conducted for *interdiscs* measurements were significant.

The results between manual and automated differ of about 5 nm, which is significant difference. Despite this, the Δ between LA and DA in the automatic calculation was 1.853 ± 2.34 nm while for the manual was 2.411 ± 2.92 nm that, considering the mean spatial resolution of .353 nm, represent a difference between one and two pixels, thus showing that the two approaches produced a very similar output, which again was tested and in this case, did not produce statistical differences. This fact support the hypothesis that the differences between LA and DA found in both the manual and automated approaches were effectively present, and that the light could cause some changes.

A *t*-test was carried out on the Outer *interdiscs* distance values attained with MATLAB®. All parameters regarding this test can be found in [APPENDIX P]. In Fig. 46 the bar plot with superimposed standard deviation regarding this analysis is shown. It is worth to highlight the significance of the test: the *p*-value indeed is equal to 0.0002.

Fig. 38, shows the bar plot built with the manually obtained values.

MATLAB® OUTER INTERDISCS DISTANCE - DA vs
LA

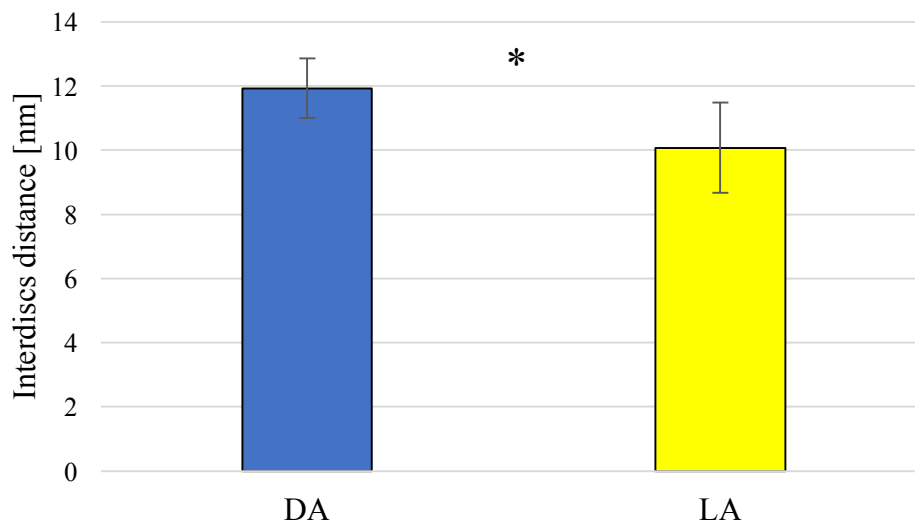


Figure 46 – Bar plot with superimposed s.d. of DA Outer OS and LA Outer OS *interdiscs* distances obtained using MATLAB®

In both tests (manual and automatic) the resulting p -values were smaller respect to the acceptance threshold α conventionally fixed at 5 %, which again entailed the rejection of the null hypothesis, statistically demonstrated that the two samples were not equal.

A similar test considering the instrumentation sensitivity ($\Delta' = 0.353$ nm/pixels) was conducted, results are not reported because identical to the previous ones.

However, although the Outer OS *interdiscs* distances gave the same conclusion for both automatic and manual analysis, the Inner OS *interdiscs* study carried out with MATLAB® slightly differ with the previous one. Indeed, the ImageJ® investigation in some test resulted in the rejection of the null hypothesis, which meant that the two groups, light and dark, were considered different, but in some others the null hypothesis was not rejected.

On the other hand, using the automatic software the resulting two measurements were statistically identical. The t -test gave as outcome a p -value equal to 0.97, which brought to the rejection of the

null hypothesis H^0 . Again, for all details regarding the test the interested reader is recommended to refer to [APPENDIX Q]. This finding further confirms what was also observed in the previous tests: most of the difference between the samples is focused in the Outer OS, the part closer to the RPE, while instead the Inner OS among the two groups has been discovered to be very similar.

Therefore, the automatic analysis not only overcome the weaknesses of the manual calculation but also gave a further confirmation of the localization of the shrinkage which was not previously clear.

Fig. 47 reports the bar plots concerning the *intradisc* distances calculated with the two thresholding methods, Otsu and *kmeans* clustering. Both tests were not significant, which meant that the *intradisc* distances between the two groups were almost identical. This important result was not achievable with the manual analysis but was possible thanks to the MATLAB® algorithm.

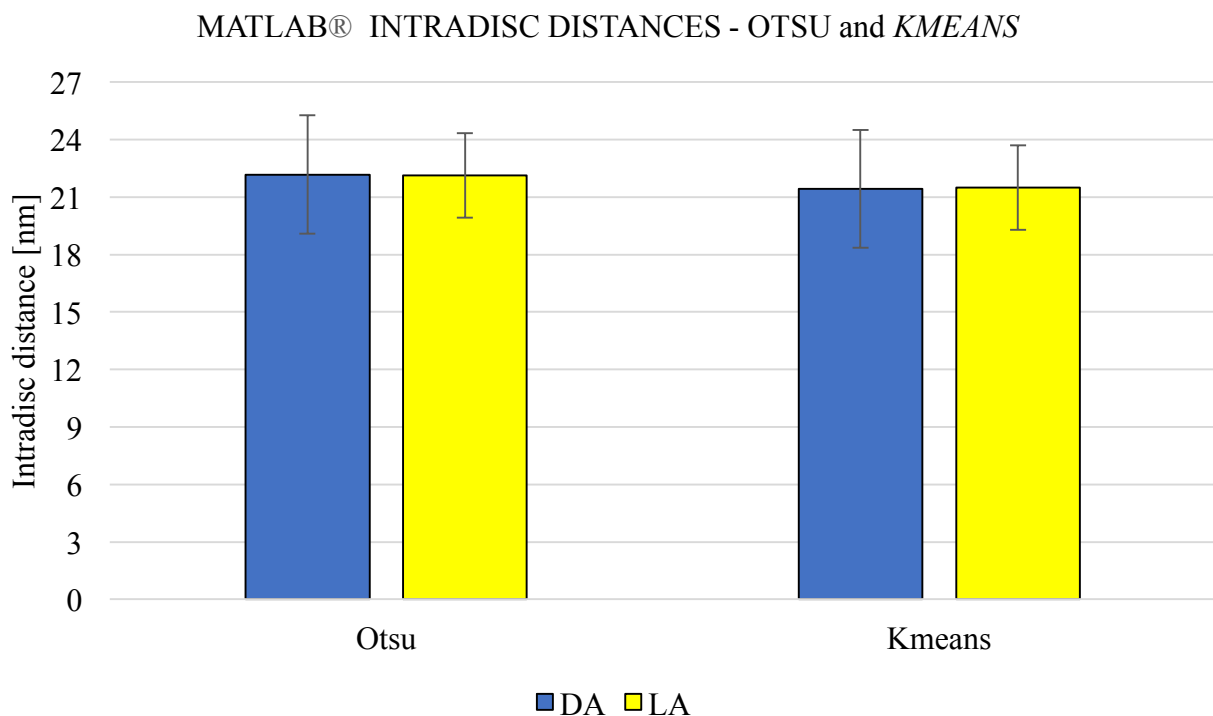


Figure 47 - Bar plots with superimposed s.d. of DA and LA *intradisc* distances obtained using MATLAB®. Two different thresholding methods were used: Otsu's and the *kmeans* clustering. Both tests are not significant

CHAPTER 5

DISCUSSION AND CONCLUSION

The aim of this project was the investigation of rods outer segment shrinking and to try to find statistically important differences between the two groups analyzed. A critical passage of the entire project was the experimental procedure. The hemisection of the eyeball was a critical step as this procedure had to be done as quickly as possible due to exposure of the samples to air affecting the plasma and membrane structures [64].

Previous experiments carried out on the entire structures of the photoreceptors, but not on the ultrastructures within them, discovered interesting behaviour: a shrinkage in the central region hit by light and a bending of the ROS at the borders of the light stimulus [30]. It was speculated that a modification at the level of the discs within the ROS could be the explanation for that, furthermore it was thought that a partial stimulation of these membranous structures could entail a partial morphological shape difference (disc misalignment) resultant in the bending of them towards the direction of light stimulus (Figs. 48 - 49).

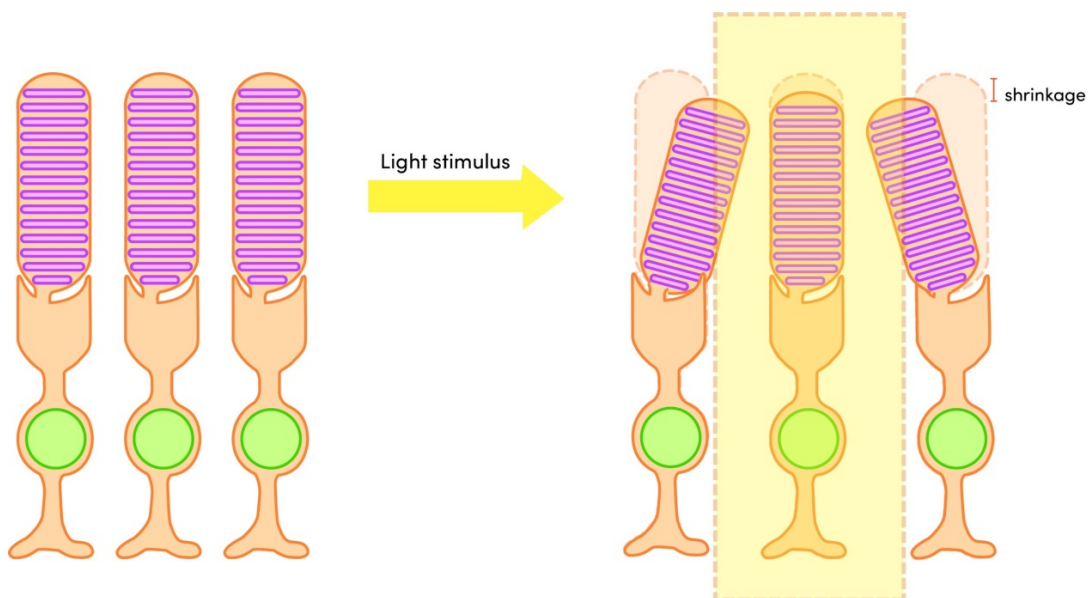


Figure 48 – Rods Outer Segment shrinkage and bending when stimulated by light

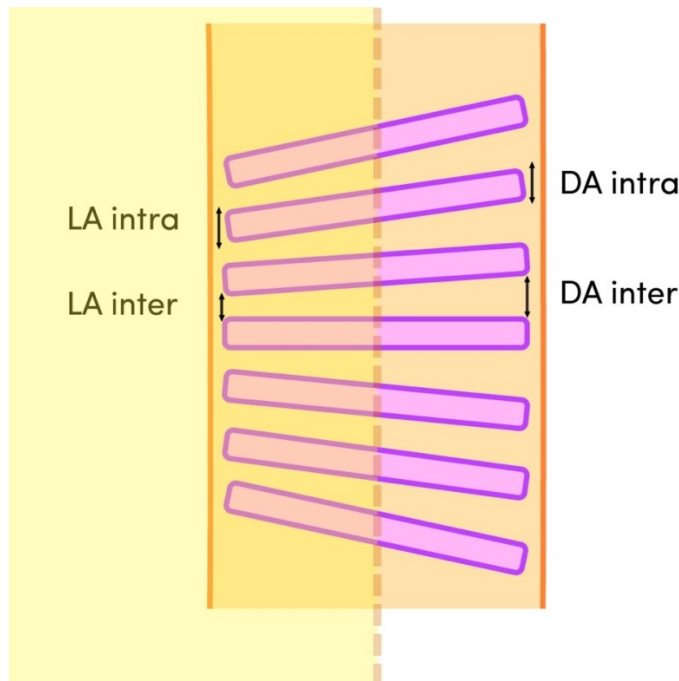


Figure 49 – Discs misalignment, hypothesized behavior to explain rod OS bending towards the direction of light

This behavior can also explain the lack of TRP in cones for the simple fact that in this type of cell the discs are linked with the membrane of the OS, while in the rods these discs are stacked one over the other and are free to float within the OS membrane [65]. A greater knowledge of this phenomenon can be useful not only because it reflects a functional retinal response but also for an early detection of degenerative eyes pathologies.

In Fig. 36 and 37 reference images obtained using the electron microscopy are presented. By looking at them one can only take a hint about the differences and similarities between the two groups but it is difficult to appreciate these disparities and analogies visually. The statistical analyses that were conducted are self-explanatory. To have a deeper understanding of the mechanism involved in the ROS movement it was necessary to compare different specimens, considering both the experiments and their precise locations.

In Fig. 38 the bar plot took into consideration all the computed *interdisc* measurements from all DA and LA samples. Interestingly, the expected results were obtained: LA *interdisc* distances were statistically different compared to the other group and showed a mean distance difference of $1.947 \pm$

3.67 nm. As previously discussed, in earlier experiments a similar behaviour was recorded at a greater scale, considering the entire photoreceptor in the isolated frog retinas [30]. In one study, the average recorded shrinkage was around 0.2 μm and it was dependent on the light stimulation intensity. If we consider that, on average, photoreceptors' membranous discs in *rana pipiens* are ~1500 - 2000 units [59], due to the data obtained by this research, it is possible to state that on average the photoreceptors would shrink by ~3.3 μm . This number is about fifteen times greater than the one calculated in the previous study [30]. However, there could be several causes of this discrepancy. Firstly, in the previous experiment isolated retinas were used. Those retinas reproduced the behaviour of physiological cells but did not mimic them, so they were different from natural conditions. This study used entire hemisected eyeballs comprising of the retina, choroid and sclera. In addition, the light stimulus duration adopted in the first study was one second, while in this project animals were maintained for at least 24 hours under constant illumination. Finally, in the first study the behaviour of individual photoreceptors was examined so that their movement could not be influenced by the physical connections to their neighbouring cells. However, this study considered the retina as a whole, so every photoreceptor moved accordingly.

Despite the differences highlighted above and the total photoreceptor shrinkage value (which could be greatly affected by a lot of factors and was qualitatively calculated considering the *interdiscs* distances) both studies obtained the same results: LA photoreceptors shrunk in their OS. This leads to important questions, such as why is this happening? And what are the molecules involved? Further studies are required to have a deeper understanding of this. However, there are explanations to be found in the relevant literature. There are numerous studies on photoreceptor disc renewal. It has been proven that light increases the rate of disc regeneration [66]. In fact, the addition rate of new discs in frogs increases threefold during the first eight hours of light adaptation [67]. This phenomenon can partly explain why in the proposed experiment OS shrinkage was greater than the one presented in Zhao's manuscript [30]. The morphogenesis of new discs, which started at the base of the OS and entails complex mechanisms, involving massive membrane growth and shaping, is highly increased

by light. Essentially, whenever newer discs are juxtaposed, the older ones are gradually displaced sclerally by the subsequent addition of those discs [65]. The oldest discs, the ones situated in the OS apical zone, are instead shed and phagocytized by the retina pigment epithelium (RPE). It is possible to speculate that light rays, which increase the rate of this mechanism, can also be a cause of the reduction in *interdisc* distances due to the greater need for new membranous ultrastructures, which in turn means a greater thrust of discs from the base to the apex. This may be an explanation, but goes beyond the effect known as Transient Retinal Phototropism. Indeed, other studies verified that this ROS movement happened in ~28 ms before the hyperpolarization of these cells [36], while instead the effect of illumination is in the order of hours. Another drawback of this hypothesis is shown in Tab. II and Fig. 39 where the *interdiscs* distance dependence on the location within the photoreceptors is displaced. There are greater changes between LA and DA in the Outer OS in respect to the Inner OS, which means that discs were closer to each other in the region near the RPE in respect to the ones close to the cilium, where indeed new discs are created and brought up. This discovery can suggest that perhaps the RPE is involved somehow in this shrinkage of *interdisc* distance, but the widely-held hypotheses are correlated to stimulus-evoked rhodopsin-, transducin- or PDE-dependent permeability changes [38]. During photo-transduction, cascade light rays catalyse a series of events that bring to the hyperpolarization of cell's membrane. These events consist in the sequential activation of molecules, which change morphologically and chemically, and then bring to the closure of cGMP-ion channels. It was proven that the ROS movement happens before the light-induced closure of these channels [36], which means that Na^+ ions concentration does not entail it but, instead, the cause must be found in previous passages of the cascade. The suspected involved molecules are rhodopsin, transducin and phosphodiesterase (PDE). Light activates rhodopsin which in turn activates transducin and their combine effort activates the heterotrimeric G protein, which releases the bound GDP in exchange for a cytoplasmatic GTP. Successively, PDE is activated and catalyses the formation of GMP from cGMP. This is a high gain mechanism so a significant amount of GTP is required and just as much GDP and GMP are released. It is thought that the change in cytosolic concentration of these

molecules can somehow cause a reduction in *interdisc* distances. In this regard, future developments concerning the TRP should be focused on trying to implement a method for the detection of the biophysical dynamics of these molecules, find out how the concentration difference can affect the photoreceptors' ultrastructure and how the permeability changes can modify their behavior and if these changes can be the cause of *interdiscs* shrinkage.

A more complete TEM analysis than the presented one should also be conducted: mainly, the study of the LA and DA behavior should be pursued on the same animal instead of analysing it on different samples. Further improvements such as delivering the light stimulus on a precise spot of the animal's retina, identifying uniquely that precise region during the hemisection/cryosection procedure and being able to focus the TEM on that exact area, are difficult to achieve. Future experiments could also be focused on the study of this phenomenon in a mouse model with the PDE gene knockout, to study its influence on the ROS dynamic.

The aim of this investigation was to find differences and similarities between two groups of samples (Light Adapted and the Dark Adapted), so the interesting parameter was the arithmetic difference of distances between those two. Following the algorithm, the obtained images could be directly compared because all the distances were calculated in the same way. Confirming references were also found in literature, as results from this analysis were consistent with previous experiments [59-62]. The manual procedure was developed first, because faster and easier to implement, although, as already described, having some serious drawbacks: the inter-individual variability and the user-dependent precision. To obtain a more accurate analysis and to strengthen previous results we decided to implement an automatic algorithm.

The automatic analysis was devised to simplify and speed the measuring process and at the same time to further improve accuracy of the results. The main advantage of the automatic analysis stood in the

possibility to analyse the image in its entirety. This allowed a greater number of results and took into consideration only those which were more significant, thanks to how the code was built.

The real advantage the MATLAB®'s routine brought is intrinsic in the software. It completely avoids the inter-variability between users. This, indeed, was probably the main problem of the entire ImageJ®'s project. Although the manual calculation of distances was carried out following a specific protocol guarantee precision, different users obtained slightly different values (1.24 ± 0.67). Therefore, it was decided to strengthen the power of this research implementing also a method which permits to bypass those problems.

The analysed images were the same but the processing of them was different. That is also why the results are congruent but not identical in absolute values.

The aim was to build an automatic tool to make the same exact calculations of the ones done manually. In order to automatize the entire process, it was necessary, after the filtering and pre-processing of the images, to transform them in black and white. This was the only way to differentiate *interdiscs* and *intradisc* measurements. At the same time binarizing an image implies loss of information, which generates different values if we compare the automatic results with the manual ones. Moreover, the manual calculations were carried out on processed greyscale images, on matrixes with more information.

The differences between manual and automated results are of 5.27 nm for *interdiscs* distances and 8.98 nm for *intradisc*. This divergence was mainly due to the pre-processing of the images which was to some extent different. Indeed, although the algorithm received in input grayscale images the distances calculation was done on black and white ones. To prove that the two automatic methods, Otsu's and *kmeans*, gave the same outcome, multiple linear regressions comparing automated and manual distances were carried out. The analyses considered the differences between LA and DA manual values with the same differences obtained with MATLAB®'s routine. The resultant R^2 was higher using Otsu's as far as *interdiscs* distances concerned, but was greater using *kmeans* for *intradisc* measurements. So, the tests were useful but they did not give a definitive answer.

The correct statistical approach to further test the congruency of results was not obvious. Many studies give the correlation coefficient (R^2) between the results of the two measurement methods as an indicator of agreement, but it is no such thing. For this reason, it was followed the Bland-Altman statistical approach comparing individually the automatic methods with the manual one. In Tab. VI are displayed the biases (calculated as the mean of the difference between automatic and manual measurements) for both groups, divided into *inter-* and *intra-discs*. In the same table are also shown the limits of agreement. Firstly, it is worth noting that the *kmeans* and Otsu's methods produced almost identical biased and standard deviations. Furthermore, these biases demonstrate that the automatic methods overestimated the manual values with a systematic error, meaning that the two techniques could be interchangeable. Secondly, the discrepancy of the data extraction mode between manual and automated could be the reason of the not elevated correlation values found in the multiple regressions and of the not so small limits of agreement, which although were small enough for us to be confident that the new methods could be used in place of the manual one.

The OSs division in three categories (Outer/Inner/Central) may be considered a limitation for how this differentiation was done, but it was performed in an accurate way: before focusing the microscope at high magnifications (150 kX or 200 kX) lower zooms were used to pinpoint the entire photoreceptor (see Fig. 21). From that view, the outer part of OS was first focused, an image was acquired, and then the microscope was brought again at a lower magnification. The procedure was then repeated for the acquisition of one central OS image and one Inner OS image. After having completed the series of three images, another cell was selected and these steps were carried out again. So, following this procedure the distinction between Outer, Inner and Central OS could be done accurately, avoiding mistaking one category with the other.

Another important aspect is highlighted in Fig. 39 (and Tab. II): both LA and DA eyes showed a trend of increase in *interdiscs* distances going from the Outer to the Inner OS. Moreover, this behaviour was more stressed in LA specimens, meaning that most of the shrinkage occurs at the level of the Outer and Central OS, while in the Inner region the differences between the two groups were

weaker ($\Delta_{\text{Outer}} = 2.411 \pm 2.78$ nm, $\Delta_{\text{Central}} = 2.634 \pm 3.09$ nm and $\Delta_{\text{Inner}} = 1.140 \pm 3.79$ nm). This finding was also confirmed by the automatic computation of distances. Furthermore, it was proved that the inner OS *interdiscs* distances between the two samples showed the same results, so these disparities were not only weaker but mainly null.

A reason for the incongruency between the manually and automatically obtained results could be found in the different amount of data analyzed but also in the type of images used to conduct the analysis. It is possible to notice in Fig. 39, looking at the Inner bar plots, how the difference is not significant and how large the standard deviations are, for both the samples, indeed crossing the opposite maximum values. Thanks to the automatic analysis, the amount of data computed for each image was larger and better achieved in respect to the ones done with ImageJ®, thus obtaining more reliable results.

The conducted frequency study on the images further proved the congruency of the methods. The sum of the mean values of the *interdiscs* and *intradisc* measurements obtained with the algorithm resulted closer to 30 nm, while the one calculated manually was around 22 nm. This was not an error, and it actually confirmed the parallelism of results. The frequency analysis was carried out on the original greyscale images, not on the binarized ones. This is the reason for the existing distance differences. Instead, those distances were almost identical to the sum of the mean *interdiscs* and *intradisc* values obtained by the manual calculation, because in the manual calculation the images used were not black and white but grayscale. In conclusion, although the algorithm gave different results from the manual calculation, the frequency response analysis confirmed the achieved conclusions. Thanks to the assessment of the Euclidian distance in the frequency domain it was possible to prove that the two methods, the automatic and manual, attained the same outcome: *interdiscs* measurements of LA animals displayed shorter distances in respect to their DA counterparts.

Figs. 41, 42 and 43 show the bar plots concerning the *intradisc* distances. Thanks to the explanation of the statistical tests and looking at those graphs we can claim that the two samples did not show differences in the discs' transversal thickness or *intradisc* distance. This behaviour was also tested and achieved with the MATLAB® algorithm, increasing the strength of the findings.

These results pinpoint that the TRP is mostly concentrated in the OS distal areas and mainly dependent on *interdiscs* differences while *intradisc* distances between the two groups are comparable and almost identical.

The main innovation of this project entails the construction of an automatic tool for comparative analysis of dark-adapted and light-adapted frog's retinas utilizing an electron microscope able to focus at the nano-level scale. This allowed to achieve a deeper understanding of the phenomena underlying the Transient Retinal Phototropism effect. This study allowed for the discovery of new features pertaining to this biophysical event, and can be considered as a small, but significant, step towards a procedure that can help simplify the detection of specific pathologies of the visual system and will allow the patient to receive timely treatment, protecting as much as possible the incredible mechanism that is our vision. The main innovation stands in the collection of analytical data related on disc-shape modification that permitted to carry out statistical analysis on the different level and locations of shrinkage among the two groups.

In 1975, the scientists who discovered the light-induced conformational changes in rod photoreceptor disc membrane, stated "It is unfortunate that we have no idea how to measure any change in the thickness of the photoreceptor disc membrane induced by the bleaching" [43]. Using transmission electron microscopy, we further improved the ability to measure these changes. The identification and quantification of the differences and similarities between the two groups has not only brought a deeper understanding of when and where the TRP phenomenon takes place, but has also contributed critical findings that will ultimately allow earlier diagnosis of retinal pathologies such as AMD or diabetic retinopathy.

APPENDICES

APPENDIX A



Department Of Bioengineering - University of Illinois at Chicago (UIC)

3/17/2017

I am writing to request permission to use an illustration about the section of the retina and the neurons of the retina present in the book Principles of Neural Science Fifth edition in my thesis. This material will appear as originally published. Unless you request otherwise, I will use the conventional style of the Graduate College of the University of Illinois at Chicago as acknowledgment.

I am currently writing a thesis about Retinal Phototropism and in my introduction I am including a section related to Eye Anatomy and Physiology. The Illustration I am talking about is: Figure 26-2, A and B, page 579.

A copy of this letter is included for your records. Thank you for your kind consideration of this request.

Sincerely,

Jacopo Benedetti

LIERI Building
1905 West Taylor Street University of Illinois at Chicago (UIC)
Chicago, IL 60612

The above request is approved.

Approved by: _____

Date: 3/17/17

APPENDIX B



Department Of Bioengineering - University of Illinois at Chicago (UIC)

3/21/2017

I am writing to request permission to use a figure present in the article: Wang, B., Zhang, Q., Lu, R., Zhi, Y., and Yao, X.: Functional optical coherence tomography reveals transient phototropic change of photoreceptor outer segments. *Optics letters*, 2004, pp. 6923 to 6926. This material will appear as originally published. Unless you request otherwise, I will use the conventional style of the Graduate College of the University of Illinois at Chicago as acknowledgment.

I am currently writing a thesis about Retinal Phototropism and in the State of Art paragraph I'd like to include the figure 3 of the above article.

A copy of this letter is included for your records. Thank you for your kind consideration of this request.
Sincerely,

Jacopo Benedetti

LIERI Building
1905 West Taylor Street ☐ University of Illinois at Chicago (UIC) ☐
Chicago, IL 60612

The above request is approved.

Approved by: _____

A handwritten signature in black ink, appearing to be "J. Benedetti", written over a horizontal line.

Date: March 23, 2017

APPENDIX C

Figure 23 *t*-test parameters of INTERDISCS measurements:

Null hypothesis: Difference of means = 0	
<p>DA Samples: n = 1100, mean = 7.75069, s.d. = 1.79889 standard error of mean = 0.0542384 95% confidence interval for mean: 7.64427 to 7.85711</p>	<p>LA Samples: n = 1042, mean = 5.80352, s.d. = 1.8877 standard error of mean = 0.058479 95% confidence interval for mean: 5.68877 to 5.91827</p>
<p>Test statistic: $t(2117) = (7.75069 - 5.80352)/0.0797597 = 24.413$</p> <p><u>Two-tailed p-value = 3.445e-116</u> (one-tailed = 1.722e-116)</p>	

If $\alpha < p$ -value: the null hypothesis H^0 is not rejected;

If $\alpha \geq p$ -value: the null hypothesis H^0 is rejected;

Where $\alpha = 0.05$;

All conducted *t*-test were performed using Gretl [63].

APPENDIX D

Figure 25 *t*-test parameters of INTERDISCS measurements:

Null hypothesis: Difference of means = 0	
DA Samples Outer: n = 460, mean = 7.21187, s.d. = 1.74938 standard error of mean = 0.0815654 95% confidence interval for mean: 7.05158 to 7.37216	LA Samples Outer: n = 362, mean = 4.8001, s.d. = 1.04398 standard error of mean = 0.0548704 95% confidence interval for mean: 4.6922 to 4.90801
Test statistic: $t(768) = (7.21187 - 4.8001)/0.098304 = 24.5338$	
<u>Two-tailed p-value = 1.338e-98</u> (one-tailed = 6.691e-99)	

If $\alpha < p$ -value: the null hypothesis H^0 is not rejected;

If $\alpha \geq p$ -value: the null hypothesis H^0 is rejected;

Where $\alpha = 0.05$;

All conducted *t*-test were performed using Gretl [63].

APPENDIX E

Figure 26 *t*-test parameters of INTERDISCS measurements:

Null hypothesis: Difference of means = 0	
DA Samples Central: n = 280, mean = 7.93318, s.d. = 1.67175 standard error of mean = 0.0999059 95% confidence interval for mean: 7.73651 to 8.12984	LA Samples Central: n = 300, mean = 5.29981, s.d. = 1.42455 standard error of mean = 0.0822466 95% confidence interval for mean: 5.13795 to 5.46167
Test statistic: $t(549) = (7.93318 - 5.29981)/0.129405 = 20.3498$	
<u>Two-tailed p-value = 5.098e-69</u> (one-tailed = 2.549e-69)	

If $\alpha < p$ -value: the null hypothesis H^0 is not rejected;

If $\alpha \geq p$ -value: the null hypothesis H^0 is rejected;

Where $\alpha = 0.05$;

All conducted *t*-test were performed using Gretl [63].

APPENDIX F

Figure 27 *t*-test parameters of INTERDISCS measurements:

Null hypothesis: Difference of means = 0	
<p>DA Samples Inner:</p> <p>n = 360, mean = 8.29725, s.d. = 1.76748</p> <p>standard error of mean = 0.0931543</p> <p>95% confidence interval for mean: 8.11405 to 8.48044</p>	<p>LA Samples Inner:</p> <p>n = 380, mean = 7.15706, s.d. = 2.03694</p> <p>standard error of mean = 0.104493</p> <p>95% confidence interval for mean: 6.9516 to 7.36252</p>
<p>Test statistic: $t(732) = (8.29725 - 7.15706)/0.139987 = 8.14493$</p> <p><u>Two-tailed p-value = 1.636e-15</u></p> <p>(one-tailed = 8.18e-16)</p>	

If $\alpha < p\text{-value}$: the null hypothesis H^0 is not rejected;

If $\alpha \geq p\text{-value}$: the null hypothesis H^0 is rejected;

Where $\alpha = 0.05$;

All conducted *t*-test were performed using Gretl [63].

APPENDIX G

Figure 30 *t*-test parameters of INTRADISC measurements:

Null hypothesis: Difference of means = 0	
<p>DA Samples: n = 1100, mean = 13.3624, s.d. = 1.52913 standard error of mean = 0.0461051 95% confidence interval for mean: 13.2719 to 13.4529</p>	<p>LA Samples: n = 1042, mean = 13.6688, s.d. = 1.84796 standard error of mean = 0.0572479 95% confidence interval for mean: 13.5565 to 13.7811</p>
<p>Test statistic: $t(2023) = (13.3624 - 13.6688)/0.0735051 = -4.16859$</p> <p><u>Two-tailed p-value = 3.194e-05</u> (one-tailed = 1.597e-05)</p>	

If $\alpha < p\text{-value}$: the null hypothesis H^0 is not rejected;

If $\alpha \geq p\text{-value}$: the null hypothesis H^0 is rejected;

Where $\alpha = 0.05$;

All conducted *t*-test were performed using Gretl [63].

APPENDIX H

Table VI (A) *t*-test parameters of INTRADISC measurements:

Null hypothesis: Difference of means = 0	
<p>DA Sample 1: n = 440, mean = 13.1535, s.d. = 1.46682 standard error of mean = 0.0699281 95% confidence interval for mean: 13.0161 to 13.291</p>	<p>LA Sample 1: n = 442, mean = 13.2666, s.d. = 1.85707 standard error of mean = 0.088332 95% confidence interval for mean: 13.093 to 13.4402</p>
<p>Test statistic: $t(836) = (13.1535 - 13.2666)/0.112661 = -1.00369$</p> <p><u>Two-tailed p-value = 0.3158</u> (one-tailed = 0.1579)</p>	

If $\alpha < p$ -value: the null hypothesis H^0 is not rejected;

If $\alpha \geq p$ -value: the null hypothesis H^0 is rejected;

Where $\alpha = 0.05$;

All conducted *t*-test were performed using Gretl [63].

APPENDIX I

Table VI (B) *t*-test parameters of INTRADISC measurements:

Null hypothesis: Difference of means = 0	
<p>DA Sample 1: n = 440, mean = 13.1535, s.d. = 1.46682 standard error of mean = 0.0699281 95% confidence interval for mean: 13.0161 to 13.291</p>	<p>LA Sample 2: n = 600, mean = 13.9651, s.d. = 1.78564 standard error of mean = 0.0728986 95% confidence interval for mean: 13.8219 to 14.1083</p>
<p>Test statistic: $t(1024) = (13.1535 - 13.9651)/0.101016 = -8.03382$</p> <p><u>Two-tailed p-value = 2.585e-15</u> (one-tailed = 1.293e-15)</p>	

If $\alpha < p\text{-value}$: the null hypothesis H^0 is not rejected;

If $\alpha \geq p\text{-value}$: the null hypothesis H^0 is rejected;

Where $\alpha = 0.05$;

All conducted *t*-test were performed using Gretl [63].

APPENDIX L

Table VI (C) *t*-test parameters of INTRADISC measurements:

Null hypothesis: Difference of means = 0	
<p>DA Sample 2: n = 560, mean = 13.5016, s.d. = 1.55487 standard error of mean = 0.0657052 95% confidence interval for mean: 13.3726 to 13.6307</p>	<p>LA Sample 1: n = 340, mean = 13.2666, s.d. = 1.85707 standard error of mean = 0.100714 95% confidence interval for mean: 13.0685 to 13.4647</p>
<p>Test statistic: $t(620) = (13.5016 - 13.2666)/0.120252 = 1.9543$</p> <p><u>Two-tailed p-value = 0.05111</u> (one-tailed = 0.02556)</p>	

If $\alpha < p$ -value: the null hypothesis H^0 is not rejected;

If $\alpha \geq p$ -value: the null hypothesis H^0 is rejected;

Where $\alpha = 0.05$;

All conducted *t*-test were performed using Gretl [63].

APPENDIX M

Table VI (D) *t*-test parameters of INTRADISC measurements:

Null hypothesis: Difference of means = 0	
<p>DA Sample 2: n = 560, mean = 13.5016, s.d. = 1.55487 standard error of mean = 0.0657052 95% confidence interval for mean: 13.3726 to 13.6307</p>	<p>LA Sample 2: n = 600, mean = 13.9651, s.d. = 1.78564 standard error of mean = 0.0728986 95% confidence interval for mean: 13.8219 to 14.1083</p>
<p>Test statistic: $t(1152) = (13.5016 - 13.9651)/0.0981396 = -4.72242$</p> <p><u>Two-tailed p-value = 2.617e-06</u> (one-tailed = 1.309e-06)</p>	

If $\alpha < p\text{-value}$: the null hypothesis H^0 is not rejected;

If $\alpha \geq p\text{-value}$: the null hypothesis H^0 is rejected;

Where $\alpha = 0.05$;

All conducted *t*-test were performed using Gretl [63].

APPENDIX N

Multiple linear regression: $D/L = \beta_0 + \beta_1 * INTRADISC + \beta_2 * INTERDISCS$

Model 1: OLS, using observations 1-2142

Dependent variable: DL

	coefficient	std. error	t-ratio	p-value	
const	0.317049	0.0786003	4.034	5.68e-05	***
INTER	0.116524	0.00455610	25.58	4.20e-126	***
INTRA	-0.0441310	0.00558978	-7.895	4.60e-15	***

Mean dependent var 0.513539 S.D. dependent var 0.499933

Sum squared resid 406.4600 S.E. of regression 0.435917

R-squared 0.240414 Adjusted R-squared 0.239704

F(2, 2139) 338.5039 P-value(F) 1.9e-128

Log-likelihood -1259.354 Akaike criterion 2524.708

Schwarz criterion 2541.717 Hannan-Quinn 2530.932

*: The more the stars the more significant is the considered *p*-value

Mutiple linear regression carrued out using Gretl [63].

APPENDIX O

Figure 31 *t*-test parameters of INTRADISC measurements:

Null hypothesis: Difference of means = -0.353	
<p>DA Sample 2: n = 1100, mean = 13.3624, s.d. = 1.52913 standard error of mean = 0.0461051 95% confidence interval for mean: 13.2719 to 13.4529</p>	<p>LA Sample 2: n = 1042, mean = 13.6688, s.d. = 1.84796 standard error of mean = 0.0572479 95% confidence interval for mean: 13.5565 to 13.7811</p>
<p>Test statistic: $t(2023) = [(13.3624 - 13.6688) - (-0.353)]/0.0735051 = 0.633797$</p> <p><u>Two-tailed p-value = 0.5263</u> (one-tailed = 0.2631)</p>	

If $\alpha < p$ -value: the null hypothesis H^0 is not rejected;

If $\alpha \geq p$ -value: the null hypothesis H^0 is rejected;

Where $\alpha = 0.05$;

All conducted *t*-test were performed using Gretl [63].

APPENDIX P

Figure 38 *t*-test parameters of INTERDISCS outer measurements obtained with MATLAB®:

Null hypothesis: Difference of means = 0	
<p>DA Samples Inner:</p> <p>n = 15, mean = 11.9283, s.d. = 0.932779</p> <p>standard error of mean = 0.240843</p> <p>95% confidence interval for mean: 11.4118 to 12.4449</p>	<p>LA Samples Inner:</p> <p>n = 15, mean = 10.0752, s.d. = 1.41541</p> <p>standard error of mean = 0.365457</p> <p>95% confidence interval for mean: 9.29135 to 10.859</p>
<p>Test statistic: $t(24) = (11.9283 - 10.0752)/0.43768 = 4.23407$</p> <p>Two-tailed p-value = 0.0002912</p> <p>(one-tailed = 0.0001456)</p>	

If $\alpha < p$ -value: the null hypothesis H^0 is not rejected;

If $\alpha \geq p$ -value: the null hypothesis H^0 is rejected;

Where $\alpha = 0.05$;

All conducted *t*-test were performed using Gretl [63].

APPENDIX Q

Figure 39 *t*-test parameters of INTERDISCS inner measurements obtained with MATLAB®:

Null hypothesis: Difference of means = 0	
DA Samples Inner: n = 15, mean = 12.5906, s.d. = 1.58606 standard error of mean = 0.409518 95% confidence interval for mean: 11.7123 to 13.4689	LA Samples Inner: n = 15, mean = 12.6056, s.d. = 1.50267 standard error of mean = 0.387987 95% confidence interval for mean: 11.7735 to 13.4378
Test statistic: $t(27) = (12.5906 - 12.6056)/0.564127 = -0.0266607$ Two-tailed p-value = 0.9789 (one-tailed = 0.4895)	

If $\alpha < p$ -value: the null hypothesis H^0 is not rejected;

If $\alpha \geq p$ -value: the null hypothesis H^0 is rejected;

Where $\alpha = 0.05$;

All conducted *t*-test were performed using Gretl [63].

APPENDIX R

Multiple linear regression:

$$DA_{OTSU_{INTER}} = \beta_0 + \beta_1 * LA_{OTSU_{INTER}} + \beta_2 * DA_{MANUAL_{INTER}} + \beta_3 * LA_{MANUAL_{INTER}}$$

Model 1: OLS, using observations 1-15

Dependent variable: DA_OTZU_INTER

	coefficient	std. error	t-ratio	p-value	
const	4.98507	2.40457	2.073	0.0624	*
LA_OTZU_INTER	0.226556	0.182435	1.242	0.2401	
DA_Manual_INTER	0.480963	0.308818	1.557	0.1477	
LA_Manual_INTER	0.0887570	0.323465	0.2744	0.7889	

Mean dependent var 11.75312 S.D. dependent var 1.160002

Sum squared resid 9.788408 S.E. of regression 0.943321

R-squared 0.480403 Adjusted R-squared 0.338695

F(3, 11) 3.390088 P-value(F) 0.057570

Log-likelihood -18.08269 Akaike criterion 44.16539

Schwarz criterion 46.99759 Hannan-Quinn 44.13522

Multiple linear regression carried out using Gretl [63].

APPENDIX S

Multiple linear regression:

$$DA_{KMINTER} = \beta_0 + \beta_1 * LA_{KMINTER} + \beta_2 * DA_{MANUALINTER} + \beta_3 * LA_{MANUALINTER}$$

Model 2: OLS, using observations 1-15

Dependent variable: DA_Kmeans_INTER

	coefficient	std. error	t-ratio	p-value
const	2.79619	3.26188	0.8572	0.4096
LA_Kmeans_INTER	0.116027	0.284947	0.4072	0.6917
DA_Manual_INTER	0.423316	0.448113	0.9447	0.3651
LA_Manual_INTER	0.724404	0.458107	1.581	0.1421

Mean dependent var 11.50643 S.D. dependent var 1.529742

Sum squared resid 17.94442 S.E. of regression 1.277228

R-squared 0.452272 Adjusted R-squared 0.302892

F(3, 11) 3.027656 P-value(F) 0.075258

Log-likelihood -22.62829 Akaike criterion 53.25659

Schwarz criterion 56.08879 Hannan-Quinn 53.22642

Mutiple linear regression carrued out using Gretl [63].

APPENDIX T

Multiple linear regression:

$$DA_{OTSU_{INTRA}} = \beta_0 + \beta_1 * LA_{OTSU_{INTRA}} + \beta_2 * DA_{MANUAL_{INTRA}} + \beta_3 * LA_{MANUAL_{INTRA}}$$

Model 3: OLS, using observations 1-15

Dependent variable: DA_OTZU_INTRA

	coefficient	std. error	t-ratio	p-value
const	-4.06046	18.0252	-0.2253	0.8259
LA_OTZU_INTRA	0.450807	0.327583	1.376	0.1961
DA_Manual_INTRA	0.181630	0.795994	0.2282	0.8237
LA_Manual_INTRA	1.01872	1.00499	1.014	0.3325
Mean dependent var	22.00048	S.D. dependent var	3.257070	
Sum squared resid	112.1705	S.E. of regression	3.193324	
R-squared	0.244740	Adjusted R-squared	0.038760	
F(3, 11)	1.188173	P-value(F)	0.358987	
Log-likelihood	-36.37385	Akaike criterion	80.74770	
Schwarz criterion	83.57991	Hannan-Quinn	80.71754	

Multiple linear regression carried out using Gretl [63].

APPENDIX U

Multiple linear regression:

$$DA_{KM_{INTRA}} = \beta_0 + \beta_1 * LA_{KM_{INTRA}} + \beta_2 * DA_{KM_{INTRA}} + \beta_3 * LA_{KM_{INTRA}}$$

Model 4: OLS, using observations 1-15

Dependent variable: DA_Kmeans_INTRA

	coefficient	std. error	t-ratio	p-value	
const	-20.2861	20.1201	-1.008	0.3350	
LA_Kmeans_INTRA	0.912579	0.350501	2.604	0.0245	**
DA_Manual_INTRA	0.691440	0.902787	0.7659	0.4599	
LA_Manual_INTRA	0.822717	1.15974	0.7094	0.4928	
Mean dependent var	20.47019	S.D. dependent var	4.394316		
Sum squared resid	144.0415	S.E. of regression	3.618657		
R-squared	0.467184	Adjusted R-squared	0.321871		
F(3, 11)	3.215012	P-value(F)	0.065427		
Log-likelihood	-38.24946	Akaike criterion	84.49892		
Schwarz criterion	87.33112	Hannan-Quinn	84.46875		

Multiple linear regression carried out using Gretl [63].

CITED LITERATURE

1. Webvision: <http://webvision.med.utah.edu/book/part-ii-anatomy-and-physiology-of-the-retina/the-retinal-pigment-epithelium/> [Online, accessed 12/12/2016].
2. Inoue, K., Kato, S., Inoue, Y., Amano, S. and Oshika, T.: The Corneal Endothelium and Thickness in Type II Diabetes Mellitus. *Japanese Journal of Ophthalmology* Volume 46, Issue 1, January–February 2002, pp. 65 to 69.
3. Struijker Boudier, H., le Noble, J., Messing, M., Huijberts, M., le Noble, F., van Essen, H.: The Microcirculation and Hypertension. *Journal of Hypertension*, Volume 10, 1992, pp. 157 to 158.
4. Paton, D.: The Conjunctival Sign of Sickle-Cell Disease. *Arch Ophthalmol.* 1961, pp. 90 to 94.
5. Oxon, H., Bright, A., Tighe, B.: The Composition and Interfacial Properties of Tears, Tear Substitutes and Tear Models. *Journal of The British Contact Lens Association* Volume 16, Issue 2, 1993, pp. 57 to 66.
6. Scanlon, V., Sander, T.: *Essential of Anatomy and Physiology*. F.A. Davis Company, November 2014, Page 230.
7. Kandel, E., Schwartz, J., Jessel, M., Siegelbaum, S., Hudspeth, A.: *Principle of Neural Science*. McGraw-Hill, Fifth Edition, 2013, pp. 628 to 633.
8. Wikipedia: https://en.wikipedia.org/wiki/Hair_cell/ [Online, accessed 12/14/2016].
9. Hagemana, G., Luthertb, P., Chonga, N.H., Johnsonc, L., Andersonc, D., Mullinsa, R.: An Integrated Hypothesis that Consider Drusen as Biomarkers of Immune-Mediated Processes at the RPE-Bruch's Membrane interface in Aging and in Age-Related Macular Degeneration. *Progress in Retinal and Eye Research* Vol. 20, No. 6, 2001, pp. 707 to 732.
10. Massin, P., et al.: Retinal thickness in healthy and diabetic subjects measured using optical coherence tomography mapping software. *European journal of ophthalmology* 12.2, 2001 pp 102 to 108.
11. Young, R.: The Daily Rhythm of Shedding and Degradation of Rod and Cone Outer Segment Membranes in the Chick Retina. *Invest. Ophthalmology Visual science*, February 1978.

CITED LITERATURE (CONTINUED)

12. Spillmann, L., Werner, J.: Visual Perception, The Neurophysiological Foundations. Academic Press Inc., California, San Diego, 1990, pp. 58 to 77 and 163 to 203.
13. Wyszecki, G., Stiles, W. S.: Color science - Concepts and Methods, Quantitative Data and Formulae. A Wiley-Interscience Publication, Vol. 8, 1982, pp 117 to 129.
14. Lisman, J. E. and Bering, H.: Electrophysiological Measurement of the Number of Rhodopsin Molecules in Single Limulus Photoreceptors. The Journal of general physiology, Volume 70, 1977, pp 621 to 633.
15. Young, R. W.: The daily rhythm of shedding and degradation of rod and cone outer segment membranes in the chick retina. Invest. Ophthalmology Visual science, February 1978.
16. Peters, K., Palade, G., Schneider, B. and David S. Papermaster, D.: Fine Structure of a Periciliary Ridge Complex of Frog Retinal Rod Cells Revealed by Ultrahigh Resolution Scanning Electron Microscopy. The Journal of Cell Biology, Volume 96, January 1983, pp 265 to 276.
17. Fain, G. L., Hardie, R. and Simon B Laughlin, S.B.: Phototransduction and evolution of Photoreceptors. Current Biology 20, R114-R124, 2010.
18. Webvision: <http://webvision.med.utah.edu/book/part-v-phototransduction-in-rods-and-cones/phototransduction-in-rods-and-cones/> [Online, accessed 2/12/2016].
19. Zimmerman, A. L., Yamanaka, G., Eckstein, F., Baylor, D. A., Stryer, L.: Interaction of hydrolysis-resistant analogs of cyclic GMP with the phosphodiesterase and light-sensitive channel of retinal rod outer segments. Proceedings of the National Academy of Sciences 82.24, 1985, pp. 8813 to 8817.
20. Leskov, I., Klenchin, H., Whitlock, G., Bownds, L., Pugh, A.: The Gain of Rod Phototransduction: Reconciliation of Biochemical and Electrophysiological Measurements. Neuron. 27 (3), 2013, pp. 525 to 537.
21. Wandell, B.: Foundation of Vision. Sinauer Associates, 1995, Chapter 2 - Image Formation.
22. MacNeil, M. A. and Masland, R. H.: Extreme diversity among amacrine cells: implications for function. Neuron 20.5, 1998, pp. 971 to 982.

CITED LITERATURE (CONTINUED)

23. Miller, R. F., and Dowling, J. E.: Intracellular responses of the Müller (glial) cells of mudpuppy retina: their relation to b-wave of the electroretinogram. *Journal of Neurophysiology* 33.3, 1970, pp. 323 to 341.
24. Ross, E.B., et al.: Synthesis of retinoic acid from retinol by cultured rabbit Müller cells. *Experimental eye research* 54.4, 1992, pp. 481 to 490.
25. Vijay, S. P. and Lam. D.: Biochemical studies of isolated glial (Muller) cells from the turtle retina. *The Journal of cell biology* 78.3, 1978, pp. 675 to 684.
26. Kandel, E., Schwartz, J., Jessel, M., Siegelbaum, S., Hudspeth, A.: *Principle of Neural Science*. McGraw-Hill, Fifth Edition, 2013, Chapter 25, 27, 28 pp. 557 to 576, pp. 602 to 637.
27. Kolb H.: Facts and Figures Concerning the Human Retina. In: Kolb H, Fernandez E, Nelson R, editors. *Webvision: The Organization of the Retina and Visual System* [Internet]. Updated 2007 Jul 5. Available from: <https://www.ncbi.nlm.nih.gov/books/NBK11556/>.
28. Schroeder, C. E., Foxe, J.: Multisensory contributions to low-level, ‘unisensory’ processing. *Current opinion in neurobiology* 15.4, 2005, pp. 454 to 458.
29. Winn, B., Whitaker, D., Elliot, D., Phillips, N.: Factors affecting light-adapted pupil size in normal human subjects. *Investigative Ophthalmology & Visual Science* 35.3, 1994, pp. 1132 to 1137.
30. Zhao, X., Thapa, D., Wang, B., Lu, Y., Gai, S., and Yao, X.: Stimulus-evoked outer segment changes in rod photoreceptors. *Journal of Biomedical Optics*, 21.6, 2016.
31. Stiles, W. S., and Crawford, B. H.: The luminous efficiency of rays entering the eye pupil at different points. *Proceedings of the Royal Society of London. Series B, Containing Papers of a Biological Character* 112.778, 1933, pp. 428 to 450.
32. Packer, O., Williams, D. R., and Bensinger, D.: Photopigment transmittance imaging of the primate photoreceptor mosaic. *Journal of Neuroscience* 16.7, 1996, pp. 2251 to 2260.
33. Wang, B., Zhang, Q., Lu, R., Zhi, Y., and Yao, X.: Functional optical coherence tomography reveals transient phototropic change of photoreceptor outer segments. *Optics letters*, 2004, pp. 6923 to 6926.
34. Sun, D., Roth, S., and Black, M. J.: Secrets of optical flow estimation and their principles. *Computer Vision and Pattern Recognition (CVPR), 2010 IEEE Conference on. IEEE*, 2010.

CITED LITERATURE (CONTINUED)

35. Lu, R., Levy, A. M., Zhang, Q., Pittler, S. J., and Yao, X.: Dynamic near-infrared imaging reveals transient phototropic change in retinal rod photoreceptors. *Journal of biomedical optics* 18.10, 2013, pp. 106013 to 106013.
36. Lu, Y., Wang, B., Pepperberg, D. R., and Yao, X.: Stimulus-evoked outer segment changes occur before the hyperpolarization of retinal photoreceptors. *Biomedical Optics Express*, 8.1, 2017, pp. 38 to 47.
37. Hofmann, K. P., Uhl, R., Hoffmann, W., and Kreutz, W.: Measurements of fast light-induced light-scattering and-absorption changes in outer segments of vertebrate light sensitive rod cells. *Biophysics of structure and mechanism*, 2.1, 1976, pp. 61 to 77.
38. Heller, J., Ostwald, T. J., and Bok, D.: Effect of illumination on the membrane permeability of rod photoreceptor discs. *Biochemistry*, 9.25, 1970, pp. 4884 to 4889.
39. Asai, H., Chiba, T., Kimura, S., and Takagi, M.: A light-induced conformational change in rod photoreceptor disc membrane. *Experimental eye research*, 21.3, 1975, pp. 259 to 267.
40. Hessel, E., Herrmann, A., Müller, P., Schnetkamp, P. P., and Hofmann, K. P.: The transbilayer distribution of phospholipids in disc membranes is a dynamic equilibrium. *European Journal of Biochemistry*, 267.5, 2000, pp. 1473 to 1483.
41. Barthel, J., and Thust, A.: Quantification of the information limit of transmission electron microscopes. *Physical review letters* 101.20, 2008.
42. Nilsson, S. e.: An electron microscopic classification of the retinal receptors of the leopard frog (*Rana pipiens*). *Journal of ultrastructure research* 10.5-6, 1964, pp. 390 to 416.
43. Asai, H., Chiba, T., Kimura, S., and Takagi, M.: A light-induced conformational change in rod photoreceptor disc membrane. *Experimental eye research*, 21.3, 1975, pp. 259 to 267.
44. Burggren, W., Warburton, S.: *Amphibians as Animal Model for Laboratory Research in Physiology*. ILAR J 2007, pp 260 to 269.
45. Rickman, C.B., LaVail, M.M., Anderson, R.E., Grimm, C., Hollyfield, J., Ash, J.: *Retinal Degenerative Diseases: Mechanism and Experimental Therapy*. *Advances in Experimental Medicine and Biology*, Volume 801, 2014, pp. 194.

CITED LITERATURE (CONTINUED)

46. Yao, X. C., Yamauchi, A., Perry, B. and George, J. S.: Rapid optical coherence tomography and recording functional scattering changes from activated frog retina. *Appl. Opt.* 44.11, 2005, pp. 2019 to 2023.
47. Yao, X. C. and Zhao, Y. B.: Optical dissection of stimulus-evoked retinal activation. *Opt. Express.* 16.17, 2008, pp. 12446 to 12459.
48. Yao, X.C., Zhao, Y. B. and Gorga, C. M.: Optical visualization of stimulus-evoked fast neural activity and spreading waves in amphibian retina. *Proc. SPIE* , 68640M, 2008.
49. Jones, G.J.: Electron microscopy of frog photoreceptor outer segments after fixation with aldehydes. *J. Cell Sci.* 16, 199-219 (1974).
50. Tam, B., Yang, L. L., Boge, T. H., Ross, B., Martens, G., Moritz, O. L.: Preparation of *Xenopus laevis* retinal cryosections for electron microscopy. *Experimental Eye Research* 136, 2015, pp. 86 to 90.
51. Bruabcher, J. L., Vieira, A., Newmark, P. A.: Preparation of the planarian *Schmidtea mediterranea* for high-resolution histology and transmission electron microscopy. *Nature Protocols*, Vol. 9 NO. 3, 2014, pp. 661 to 673.
52. Heller, J., Ostwald, T. L. and Bok, D.: The osmotic behavior of Rod Photoreceptor outer segment discs. *The Journal Of Cell Biology*, Volume 48, 1971, pp. 633 to 649.
53. Lambert, L., Mulvey, T., Mulvey, L., Mulvey, Leslie: Ernst Ruska (1906–1988), designer extraordinaire of the electron microscope: a memoir. *Advances in imaging and electron physics* 95, 1996, pp. 2 to 62.
54. Egerton, R. F.: *Physical principles of electron microscopy*. New York: Springer, 2005, pp. 11 to 17.
55. Burghard, R. C., Droleskey, R.: *Transmission Electron Microscopy*. UNIT 2B.1, *Current protocols in microbiology*, 2006.
56. Muller, S., Aebi, U., Engel, A.: What transmission electron microscopes can visualize now and in the future. *Journal of Structural Biology* 163, 2008, pp. 235 to 243.
57. Williams, D. B., Carter, C. B.: *Transmission Electron Microscopy - A textbook for material science*. Springer Science+ Business Media, LLC, 1996, pp. 67 to 83.

CITED LITERATURE (CONTINUED)

58. Rasband, W.: National Institutes of Health, USA. <http://imagej.nih.gov/ij>, Java 1.6.0_65 (64-bit), 2016.
59. Nickell, S., Park, P. S. H., Baumeister, W., and Palczewski, K.: Three-dimensional architecture of murine rod outer segments determined by cryoelectron tomography. *J Cell Biol*, 177.5, 2007, pp. 917 to 925
60. Nir, I., and Pease, D. C.: Ultrastructural aspects of discs in rod outer segments. *Experimental eye research* 16.3, 1973, pp. 173 to 182.
61. Webb, N. G.: X-ray diffraction from outer segments of visual cells in intact eyes of the frog. *Nature* 235.5332, 1972, pp. 44 to 46.
62. Korenbrot, J. I., Brown, D. T., and Cone, R.: Membrane characteristics and osmotic behavior of isolated rod outer segments. *The Journal of Cell Biology* 56.2, 1973, pp. 389.
63. Cottrell, A. and Lucchetti, R.: Gretl User Manual, 2007, <http://ricardo.ecn.wfu.edu/pub/gretl/manual/>
64. Haas, G. G., DeBaul, L., D'Cruz, O., Shuey, R.: The effect of fixatives and/or air-drying on the plasma and acrosomal membranes of human sperm, Volume 50, Issue 3, 1988, pp. 487 to 492.
65. Young, R. W.: The renewal of photoreceptor cell outer segments, *JCB home*, volume 33 NO. 1, 1967, pp. 61 to 72.
66. Hsu, Y., Chuang, J. Z., Sung, C.: Light regulates the ciliary protein transport and outer segment disc renewal of mammalian photoreceptors. *Developmental cell* 32.6, 2015, pp. 731 to 742.
67. Volland, S., Hughes, L., et al.: Three-dimensional organization of nascent rod outer segment disk membranes. *Proceedings of the National Academy of Sciences* 112.48, 2015, pp. 14870 to 14875.
68. Chan, R. H., Ho, C. W., & Nikolova, M.: Salt-and-pepper noise removal by median-type noise detectors and detail-preserving regularization. *IEEE Transactions on image processing*, 14(10), 2005, pp. 1479 to 1485.
69. Robinson, G. S.: Edge detection by compass gradient masks. *Computer graphics and image processing*, 6(5), 1997, pp. 492 to 501.

CITED LITERATURE (CONTINUED)

70. Mathworks:https://it.mathworks.com/help/images/ref/imbinarize.html?searchHighlight=imbinarize&s_tid=doc_srchtile [Online, accessed 7/12/2017]
71. ComputerScienceSource:
<https://computersciencesource.wordpress.com/2010/09/03/computer-vision-the-integral-image/> [Online, accessed 4/9/2017]